New concept, implementation and analysis of the multicell piezoelectric motor for the control of the car seat position

Roland Ryndzionek

THÈSE

En vue de l'obtention du

DOCTORAT DE L'UNIVERSITÉ DE TOULOUSE

Délivré par :

Institut National Polytechnique de Toulouse (INP Toulouse)

Discipline ou spécialité :

Génie Électrique

Présentée et soutenue par :

M. ROLAND RYNDZIONEK

le mardi 29 septembre 2015

Titre :

CONCEPTION, REALISATION ET CARACTERISATION D'UN MOTEUR PIEZOELECTRIQUE MULTICELLULAIRE, POUR APPLICATIONS AUTOMOBILES

Ecole doctorale :

Génie Electrique, Electronique, Télécommunications (GEET)

Unité de recherche :

Laboratoire Plasma et Conversion d'Energie (LAPLACE)

Directeur(s) de Thèse :

M. JEAN FRANCOIS ROUCHON

M. MIECZYSLAW RONKOWSKI

Rapporteurs :

M. LIONEL PETIT, INSA LYON

M. SLAWOMIR WIAK, TECHNICAL UNIVERSITY OF LODZ

Membre(s) du jury :

M. JANUSZ NIEZNANSKI, POLITECHNIKA GDANSK POLOGNE, Président

M. FRANCOIS PIGACHE, INP TOULOUSE, Membre

M. JEAN FRANCOIS ROUCHON, INP TOULOUSE, Membre

M. MICHAL MICHNA, POLITECHNIKA GDANSK POLOGNE, Membre

M. MIECZYSLAW RONKOWSKI, POLITECHNIKA GDANSK POLOGNE, Membre

PRAGNĘ SERDECZNIE PODZIĘKOWAĆ

Promotorowi Prof. Jean-Francois Rouchon za szczególną opiekę, mobilizację do pracy, inspirujące dyskusje merytoryczne podczas moich studiów oraz staży w INP-ENSEEIHT-LAPLACE w Tuluzie.

Promotorowi dr hab. inż. Mieczysławowi Ronkowskiemu prof. nadzw PG za życzliwość, mobilizację do pracy, za liczne dyskusje oraz pomoc w przygotowaniu niniejszej rozprawy.

Prof. Marii Pietrzak-David za pomoc, porady podpowiedzi, które okazały się nieocenione podczas moich studiów oraz staży w INP-ENSEEIHT-LAPLACE w Tuluzie.

Promotorowi pomocniczemu dr inż. Michałowi Michnie za cenne rady, poświęcony czas przez cały okres moich studiów doktoranckich.

Dominique Harribey za cenną pomoc przy realizacji prototypu wielokomórkowego silnika piezoelektrycznego oraz wsparcie techniczne moich badań w Laboratorium LAPLACE.

Chciałbym szczególnie podziękować moim Rodzicom, za ich wielkie wsparcie podczas moich studiów w Gdańsku i Tuluzie. Mamo, Tato mam nadzieję, że spełniłem Wasze oczekiwania.

Chciałbym podziękować mojej siostrze Izabeli oraz Jakubowi za cierpliwe wsparcie w czasie redagowania pracy.

Chciałbym również podziękować moim kolegom z Katedry Energoelektroniki i Maszyn Elektrycznych: Filipowi, Łukaszowi, Dominikowi, Grzegorzowi oraz wszystkim moim koleżankom i kolegom z Erasmusa w szczególności Carlosowi, Faycelowi, Fernandzie, Elenie, Hemzie, Maćkowi oraz Marcinowi.

ACKNOWLEDGEMENTS

I would like to thank Prof. Jean-Francois Rouchon, my supervisor in France. He did make me feel like his colleague, more than a graduate student, throughout my entire PhD study. He provides a very pleasant research environment in the lab and he really knows how to communicate with his students.

I would like to extend my deepest gratitude to Prof. Mieczysław Ronkowski for he has been more than an academic advisor over the last four years. Prof. Ronkowski has been a great advisor who was always available to discuss and support the technical problems came to my mind.

Prof. Marii Pietrzak-David, she been very helpful since the first day I started study at INP-ENSEEIHT and LAPLACE Laboratory. The friendly office environment and numerous beautiful aspects of ENSEIHT have a lot to do with her presence and energy. She keeps so many things running simultaneously with an amazing performance.

I would like to extend my appreciation to my co-supervisor, PhD Michal Michna, for all help over this four years. He has been available to discuss and advise on non-technical problems of life as well.

I owe thanks to Dominique Harribey for introducing me the lab equipment in LAPLACE. It was in those days when he helped me with conducting the experiments with piezo.

I would like to thank my sister Izabela and Jacob for their patience in editorial work.

I owe special thanks to my parents, for their patience and support during my PhD study.

I truly enjoyed sharing the same office and the lab with several colleagues and friends: Filip, Łukasz, Dominik, Grzegorz.

I met another great colleague during my study in France: Carlos, Faycel, Fernanda, Elen, Hemza, Max, Maciek and Marcin.

Oraz wszystkim tym, których nie wymieniłem, a bez których niniejsza praca by nie powstała.

REMERCIEMENTS

Je voudrais remercier également le Professeur Jean-François Rouchon pour son accueil chaleureux qu'il m'a réservé pendant mes études à l'ENSEEIHT à Toulouse et pendant mon stage dans le laboratoire LAPLACE.

Je tiens à remercier vivement le Professeur Mieczysław Ronkowski pour sa grande bonté et d'avoir accepté de diriger cette recherche, de m'avoir accompagné toujours avec un mot d'encouragement positif et optimiste dans un domaine si difficile et complexe.

J'adresse mes sincères remerciements au Professeur Maria Pietrzak-David pour ses conseils et commentaires, toujours très pertinents pendant mon séjour en France.

Je remercie le Docteur Michal Michna pour son aide précieuse et pour sa grande disponibilité pendant cette recherche au long de ses différentes étapes.

Je tiens particulièrement à remercier mes parents pour leur soutien pendant mes études à Gdansk et à Toulouse. Maman, papa, j'espère que j'ai bien réalisé vos attentes.

Je suis également très reconnaissant envers ma soeur Izabela et Jacob pour leur patience et aide à corriger mon relecture attentive.

Je remercie également mes collègues du département: Philippe, Luc, Dominique, Gregory et tous mes collègues d'Erasmus en particulier Carlos, Faycel, Fernanda, Elena, Hemza, Maciek et Martin.

j'exprime également toute ma gratitude à toutes celles et tous ceux qui, d'une façon ou d'une autre ont contribué à la réalisation de cette thèse.

STRESZCZENIE

Rozprawę zrealizowano jako wspólny doktorat Politechniki Gdańskiej z uczelnią INP – ENSEEIHT-LAPLACE w Tuluzie (Francja). Praca doktorska jest kontynuacją dotychczasowych badań nad przetwornikami piezoelektrycznymi prowadzonymi w Katedrze Energoelektroniki i Maszyn Elektrycznych Politechniki Gdańskiej. Pracę częściowo zrealizowano w ramach staży naukowych w laboratorium LAPLACE w Tuluzie.

Podstawowym celem rozprawy doktorskiej było opracowanie nowej koncepcji, realizacja, badania symulacyjne i eksperymentalne prototypu wielokomórkowego aktuatora piezoelektrycznego (WAP) przeznaczonego do sterowania położeniem fotela w samochodzie osobowym.

Nowatorstwo koncepcji WAP polega zastosowaniu struktury elektromechanicznej złożonej z trzech aktuatorów piezoelektrycznych rezonansowych o modulowanym ruchu obrotowym. Taka struktura WAP umożliwiła połączenie zalet piezoelektrycznego silnika ultrasonicznego z falą biegnącą oraz silnika piezoelektrycznego o ruchu obrotowym modulowanym. Zapewniło to uzyskanie zarówno względnie większych wartości momentu obrotowego jak i prędkości obrotowej WAP. Ponadto, wielokomórkowa struktura WAP zmniejsza liczbę elementów w układzie przeniesienia napędu, umożliwiając bezpośrednie sprzęgnięcie WAP z wałkiem napędowym. Bezpośrednim efektem jest uzyskanie: zintegrowanej struktury układu sterowania położeniem fotela w samochodzie osobowym, zwiększonej wydajności układu, niskiego poziom szumów oraz niskiego kosztu wykonania.

Rozprawa doktorska podzielona jest na siedem rozdziałów. W rozdziale pierwszym przedstawiono tezę i cel rozprawy. W rozdziale drugim zostały omówione materiały piezoelektryczne i najważniejsze topologie przetworników piezoelektrycznych. W kolejnych rozdziałach przedstawiono koncepcję WAP, model analityczny, proces prototypowania oraz budowę modelu wirtualnego i modelu symulacyjnego z zastawaniem metody MES. W rozdziale szóstym opisano proces wykonania prototypu WAP i wyniki badań laboratoryjnych. W ostatnim rozdziale przedstawiono podsumowanie wykonanych badań, osiągniecia rozprawy oraz plan dalszych prac badawczych związanych z optymalizacją i rozwojem WAP.

Rozprawę doktorską zrealizowano w ramach pełnego cyklu badawczego, stosując metody analityczne, symulacyjne i doświadczalne. Wiarygodność wyników badań z zastosowaniem metod analitycznych i metod numerycznych zweryfikowano badaniami doświadczalnymi. Zasadnicze wyniki rozprawy można podsumować następująco: opracowanie nowej koncepcji WAP; sformułowanie modelu analitycznego do wyznaczania parametrów i charakterystyk elektromechanicznych WAP; opracowanie modelu wirtualnego WAP i wykonanie badań symulacyjnych metodą MES; realizacja prototypu WAP z zastosowaniem technologii obróbki CNC i technologii druku 3D; weryfikacja laboratoryjna prototypu WAP.

ABSTRACT

The research works in the frame of the dissertation have been carried out with the cooperation between the University INP - ENSEEIHT - LAPLACE (Laboratory on Plasma and Conversion of Energy), Toulouse, France, and the Gdańsk University of Technology, Faculty of Electrical and Control Engineering, Research Unit Power Electronics and Electrical Machines, Gdańsk, Poland.

The main scope of the dissertation was following: development a novel concept, implementation and analysis of the multicell piezoelectric motor (MPM) for the control of the car seat position.

The new concept of the MPM is based on a combined topology using the working principles of the traveling wave motor/actuator (known as the Shinsei motor), and the electromechanical structure of the rotating-mode motor/actuator. The electromechanical structure of each rotating-mode motor has been considered as an independent one – referred to as a "single cell".

The application of the novel MPM for the control of the car seat position will reduce the number of gears due to its direct coupling with the driving/movement shaft of the seat positioning system. The achieved effects of a such integrated structure will be following: a higher efficiency, a lower noise of performance, a low cost of manufacturing, and in general a lower pollution of the environment.

The dissertation contains seven chapters. In the first chapter the thesis and the objectives of the dissertation have been presented. The second chapter describes the piezoelectric phenomenon, piezoelectric materials, structures of piezoelectric motors (actuators). The third chapter briefly describes the presently applied servo drives for the control of the car seat position. Next, the known structures of the multi piezoelectric motors have been considered in view of their applications for car seat adjustment. Finally, a general introduction to prototyping a novel concept MPM have been presented. The forth chapter contains a description of analytical approach to modeling the basic structures of piezoelectric motors (actuators). First, modeling of the resonance structure using the Mason's equivalent circuit has been explained. Next, the principle and the basic relationships involved in the Langevin's transducer and rotating-mode motor have been considered. Moreover, the rotating-mode motor stator kinematics has been presented, since there is a difference between the excited mode of the rotating-mode motor and the Langevin's transducer. Finally, using the Langevin's transducer equivalent circuit, the analytical model of the MPM has been developed and implemented in the Matlab software. The MPM developed model is based on properly modified known analytical model of the rotating-mode motor. The MPM preliminary dimensions and parameters have been determined using the developed analytical model. In the fifth chapter the preliminary dimensions and parameters of the prototype MPM have been verified using its virtual (geometrical) model and developed FEM model. Using the FEM model of the prototype MPM the resonance frequencies and stress values have been determined. In the sixth chapter the manufacturing process, assembling and experimental verification of the prototype MPM has been described. The final chapter describes the dissertation conclusions: research results and the dissertation achievements, and the future research works.

RESUME

L'étude présentée est le fruit d'une collaboration entre le groupe de recherche de l'Electrodynamique du INP-ENSEEIHT (Toulouse), LAPLACE Laboratoire de Recherche et l'École Polytechnique de Gdańsk, le Département Génie Electrique et Automatique. L'objectif de cet projet est la conception d'un moteur piézoélectrique multicellulaire composé de plusieurs stators de moteurs à rotation de mode (3 au minimum) permettant de garantir des fréquences de résonance élevées ainsi qu'une répartition des efforts de frottement plus favorables. Le dimensionnement du moteur s'appuiera sur un cahier des charges du domaine de l'automobile, en visant une structure la plus simple possible à mettre en œuvre.

Outre un travail important concernant la conception, il faudra procéder à sa caractérisation après la réalisation du prototype. La dernière étape concernera la définition des stratégies d'alimentation et de commande d'une telle structure qui posera inévitablement le problème de l'autoadaptativité des cellules résonantes à une même fréquence de résonance.

Le moteur multicellular (MPM) proposé sera une combinaison du moteur à onde progressive annulaire (Shinsei) et moteur à rotation de mode. Il combine les avantages des deux moteurs par une combinaison de trois cellules élémentaires de moteurs à rotation de mode. La combinaison de ces deux concepts, accroît le nombre de surface de contact.

Les dimensions préliminaires et les paramètres de la MPM prototype ont été vérifiés en utilisant son modèle développé analytique (géométrique) et méthodes numériques (MÉF). Le modèle analytique de la MPM a été développé sur la base de circuit équivalent de la Langevin actuateur. La model analytique a été fait dans Matlab. Les principaux paramètres calculés sont: fréquence de résonance 26.2 kHz, couple bloque 0.4 Nm et la vitesse 40 tr/mn. En utilisant le modèle MÉF les fréquences de résonance et les valeurs du stress de la MPM prototype ont été déterminés. . Des simulations ont été effectuées pour sélectionner la fréquence de résonance et la forme pour concevoir le contre mass. Les fréquences de résonances résultantes sont 25.6 kHz et simulations du stress moins de 9 N/mm^2. Comparaison des résultats fréquence de résonance calcule à modèle analytique (26.2 kHz) et le modèle FEM (25.6 kHz) du une prototype MPM, il convient de noter, que de modèle analytique est fortement modèle précis.

Enfin, la réalisation des pièces par imprimante 3D a été décidée (contre-mass et carter) et les matériaux: aluminium et nylatron. Les autres parties ont été réalisés sur une machine à commande numérique à l'aide de l'acier.

Les mesures de la MPM prototype ont été effectuées. L'étape suivante a consisté à tester le moteur et vérifier la fréquence de résonance, et la mesure de déplacement, résonances fréquences résultantes sont 22 kHz et déplacement 1.1 μm sur rotor/stator point du contact. Finalement, les paramètres mécaniques ont été mesurés. Les meilleurs paramètres mécaniques ont été obtenus sur dSpace support de laboratoire: vitesse - 46-48 tr/mn, et le couple bloqué – 0.4 Nm. Les résultats sont satisfaisants et donnent un bon point de départ pour les futurs travaux.

CONTENTS

1 GENERAL INTRODUCTIONS

The modern applications of mechatronic/electromechanical motion systems feature increasing integration of motor (actuator), and sensor functions within a coupling mechanism. This tendency is especially advanced in the field of motors (actuators) characterized by centimetric or decimetric dimensions. It opens an area to design a new generation of electromechanical motion devices which are capable to take up the challenge of the tendency to the more open electrical technology (MOET). In different fields of technology such as: automotive, e.g., engine controlling systems, driving comfort; bio-medical engineering, e.g., driven prostheses, robotized micro-surgery; smart houses and building; avionics and aeronautics, e.g., actuators for flight control, actuators for energy sources system management. [43], [44], [69], [70]. Achieved recently progress in the field of materials engineering, whether passive materials (composite magnetic materials) or smart (intelligent materials)/electroactive (piezoelectric, electrostrictive ceramics, magnetostrictive alloys, shape memory alloys) supports a very promising field of innovations with a very high level of functional integration of mechatronic/electromechanical motion systems [45], [53], [73].

The piezoelectric motors (actuators) are relatively new in comparison to the motors using electromagnetic structures. The results, obtained in the field of piezoelectric motors, have pointed out that these motors have potentially high possibilities in the forthcoming special and advanced applications. The piezoelectric motors (actuators) feature interesting properties in terms of torque per mass ratio. In general, their torque is 10 – 100 times higher than the electromagnetic motors (actuators) of the same size or same weight.

Applications of the piezoelectric motor (actuator) reduces the number of gears due to coupling it directly to the power train shaft. As a result a better efficiency of the electromechanical motion system is gained . In turn, for positioning application, where a high blocking torque is required, particularly the multi-piezoelectric motors (actuators) seems to be the most suitable.

In this dissertation new concept of a multi piezoelectric motor dedicated to adjust the position of car seats has been considered.

1.1 OBJECTIVES OF THIS DISSERTATION

The research work described in this dissertation has been conducted as part of the European Union sponsored programme ERASMUS [**91**], and project called The Center for Advanced Studies - the development of interdisciplinary doctoral studies at the Gdansk University of Technology in the key areas of the Europe 2020 Strategy, referred to as Advanced PhD* [**92**].

The research works has been carried out with the cooperation between the INP - ENSEEIHT - LAPLACE (Laboratory on Plasma and Conversion of Energy), in Toulouse, France, and the Gdańsk University of Technology, Faculty of Electrical and Control Engineering, Research Unit Power Electronics and Electrical Machines, Gdańsk, Poland [**90**].

*The project is co-financed by the European Union within the European Social Fund – Human Capital Operational Programme (HC OP).

The Laboratory LAPLACE is an interuniversity research unit and is involved in advanced research programs in the following fields: technological plasmas and their applications, transport phenomena, dielectric materials (particularly polymers) and their integration into systems, design of electrical systems, optimization of control systems and converters [**89**]. One of the Laboratory LAPLACE's research group – GREM3 – is a leading research unit in the world in the field of piezoelectricity and shape-memory alloys technology.

The first part of the 12 months studying and research programme in the frame of ERASMUS started in September 2011 at the INP-ENSEEIHT-LAPLACE. This programme in the frame of "Transformation de l'Energie et Mécatronique avancée" covered issues of power electronics, automation and mechatronics systems, and has been completed with the Master International research project and diploma. The first part of the carried out research covered the "Rotating-mode motor – simulations, manufacturing and measurements", and also the "Hybrid piezoelectric motor". In turn, the second part: six months Master International research project has been called "Moteur piézoélectrique multicellulaire".

The second part of the 10 months research programme in the frame of the Advanced PhD started in October 2013 and has been divided into 7 months research work carried out at the Research Unit Power Electronics and Electrical Machines, and 3 months internship at the Laboratory LAPLACE. The subject of the research work conducted at the Laboratory LAPLACE was "Multicell piezoelectric motor" and has covered measurements and analysis of the performance characteristics of the prototype multicell piezoelectric motor.

It should be underlined that the research works in the field of piezoelectric technology have not been carried out on a wide scale in Poland, so far. The research works conducted in the frame of this disseration are one of the pioneer research works in Poland, that focuses on application of piezoelectric phenomenon to design and manufacture piezoelectric motors (actuators).

The thesis of this dissertation is following:

> *Multicell piezoelectric motor based on the concept of a combined topology using the working principles of the traveling wave motor, and the electromechanical structure of the rotating-mode motor is characterized by a relatively high values of the rotating speed and blocking torque, respectively.*

To describe in systematic way the development of modeling, design, measurement, and manufacturing (implementation) technology for new concept multicell piezoelectric motor the dissertation has been structured as follows.

The chapter 2 describes the piezoelectric phenomenon, piezoelectric materials, structures of piezoelectric motors (actuators).

The chapter 3 briefly describes the presently applied servo drives for the control of the car seat position. Next, the known structures of the multi piezoelectric motors have been considered in view of their applications for car seat adjustment. Finally, a general introduction to prototyping

a novel concept multi piezoelectric motor, referred to as "multicell piezoelectric motor" (MPM), have been presented.

The chapter 4 contains a description of analytical approach to modeling the basic structures of piezoelectric motors (actuators). First, modeling of the resonance structure using the Mason's equivalent circuit has been explained. Next, the principle and the basic relationships involved in the Langevin's transducer and rotating-mode motor have been described. Moreover, the rotating-mode motor stator kinematics has been presented, since there is a difference between the excited mode of the rotating-mode motor and the Langevin's transducer. Finally, using the Langevin's transducer equivalent circuit, the analytical model of the MPM has been developed and implemented in the Matlab software. The MPM developed model is based on properly modified known analytical model of the rotating-mode motor. The MPM preliminary dimensions and parameters have been determined using the developed analytical model.

In chapter 5 the preliminary dimensions and parameters of the prototype MPM have been verified using its virtual (geometrical) model and developed FEM model. Using the FEM model of the prototype MPM the resonance frequencies and stress values have been determined.

In chapter 6 manufacturing process, assembling and experimental verification of the prototype MPM has been described.

Finally, the last chapter describes the final conclusions: research results and the dissertation achievements, and future research works.

To this dissertation five appendixes are attached.

2 PIEZOELECTRIC PHENOMENA, MATERIALS AND STRUCTURES

In the first part of this chapter the piezoelectric phenomenon has been explained and the piezoelectric materials have been described as well. In the second part the main topologies of the piezoelectric motors have been presented.

Piezoelectricity is widely used in industrial sectors such as the production and detection of sound, generation of high voltages, electronic frequency generation, microbalances, driving an ultrasonic nozzle and ultrafine focusing of optical assemblies. It is also the basis of a number of scientific instrumental techniques using atomic resolution e.g. the scanning probe microscopies such as a scanning tunneling microscope (STM), atomic force microscopy (AFM), microthermal analysis (MTA), near-field scanning optical microscopy (NSOM/SNOM) etc. It can be found useful in everyday life activities, such as acting as an ignition source for lighters.

2.1 PIEZOELECTRIC PHENOMENA

Some materials combine electromagnetic and mechanical properties that interact with each other even within these materials [**39**]. Thus, they have an intrinsic electromagneto-elastic coupling properties that can be used to build up electromechanical transducers, i.e., motors and actuators [**65**].

Historically, the phenomenon of magnetostriction (1847) was discovered before piezoelectricity (1881) by James Joule [**27**]. He discovered that a ferromagnetic material changed its length with the application of magnetism. The development of the new materials (especially rare earth element) has resulted in discovered the new phenomenon.

The first research work on piezoelectricity has been done by Carl Linnaeus and Franz Aepinus in the mid-18th century [**2**], [**33**]. They studied the pyroelectric effect, by which material generates an electric potential in response to a temperature change. Based on this knowledge, both René Just Haüy and Antoine César Becquerel posited a connection between mechanical stress and electric charge. However both experiments were found unconvincing [**76**].

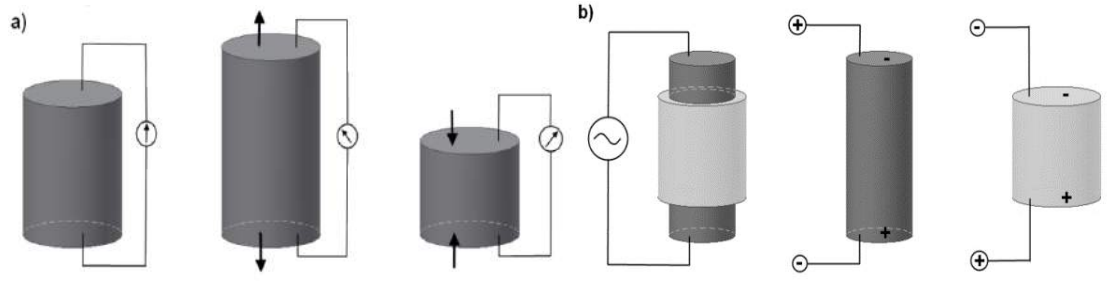

*Fig. 2.1 An illustration of piezoelectric effect a) direct b) inverse [**59**]*

The first phenomenon is called the direct piezoelectric effect. The name "piezoelectricity" was given by Wilhelm Gottlieb Hankel [**28**]. When mechanical force or pressure is applied to piezoelectric material, the electric charge or voltage is induced on the surface (Fig. 2.1a).

Conversely, if some charge or voltage is imposed on a piezoelectric material, the material reacts by generating some mechanical force and strain. This phenomenon is called the converse piezoelectric effect (Fig. 2.1b). Pierre and Jacques Curie show in 1881, the direct piezoelectric effect. A year later, Pierre and Jacques Curie, basing on the work of Lippmann, demonstrated the existence of an inverse effect [**4**], [**12**]- [**13**], [**34**].

The first commercial application of the inverse piezoelectric effect was the sonar system during the First World War [**73**]. In 1917, Paul Langevin used a piezoelectric material (quartz) to detect the presence of submarines. The sonar consisted of a transducer, made of thin quartz crystals glued between two steel plates, and a hydrophone to detect the returned echo-signal. By emitting a high-frequency pulse signal from the transducer, and measuring the value of time it takes to hear a signal from the sound waves bouncing off an object, one can calculate the distance to that object. Materials used then, (quartz, tourmaline, Rochelle salt, etc.) revealed weak piezoelectric features. The need to produce materials with improved performance has led to the invention of ceramic polycrystalline [**6**].

In 40's, during World War II, in the United States, USSR, and Japan discovered a new class of synthetic materials. It was called ferroelectrics. Piezoelectric properties raise when exposing it to an electric field polarization due to the many times higher piezoelectric constants than natural materials. This helps to intense research and develop a barium titanate and later a lead zirconate titanate materials with specific properties for particular application. Barium titanate and plumbum zirconate titanate, have been named with the acronym PZT. Nowadays, the piezoelectric phenomenon is used in several areas such as sensors, actuators, positioning, detection of seismic zones, igniters, microphones, etc.. The PZT ceramics are most commonly used for piezoelectric motors [**3**].

*Tab. 2.1 Major applications of piezoelectricity [**76**]*

Communications and control	Industrial	Health and consumer	Newer applications
• Cellular radio • Television • Automotive radar	• Sensors • Actuators • Pumps • Motors	• Transducers • Sensors • Actuator	• Smart Structures • High Displacement Transducers • Mixed-effect Device
o Signal processing o Frequency control and timing o Correlators o Convolovers o Filters o Delay lines o Oscilators	o Ultrasonic cleaning sonar o Nondestructive evaluation (NDE), o Liquid level sensors o Vibration damping o High temperature sensors o Material properties determination o Chemical/biological sensors	o Noninvasive medical o diagnostics Hyperthermia Lithotripsy o Subcutaneous medication o Wristwatches o Camera focusing /steadying / ranging o Computer timing / printing / modem o Ignition of gases ("spark pump")	o Microelectromechanical (MEMS) devices o Microoptomechnaical (MOMS) device o Biomimetic devices o Composite and functionally graded devices o Rainbow devices o Acousto-photonic-electronic devices

2.2 PIEZOELECTRIC MATERIALS

As was written in previous chapter, the first mineral which established the piezoelectric effect was quartz. Quartz (Fig. 2.2) is the second most abundant mineral in the Earth's continental crust, after feldspar. The technological progress allowed to increase the material's properties. The technology of cuts (SC - Stress Compensated developed in 1974) improved the sensitiveness to mechanical stresses and increased temperature transient effects. Working frequencies ranged from below 1 kHz to above 10 GHz [**76**].

Two types of quartz crystals exist: left-handed and right-handed. This two types differ in the optical rotation but they are identical in other physical properties. If the cut angle is correct, both left and right-handed crystals can be used for oscillators. In manufacture, the right-handed quartz is commonly used. Quartz exists in several phases. At 573 °C at 1 atmosphere (and at higher temperatures and higher pressures) the α-quartz undergoes quartz inversion, transforms reversibly to β-quartz. The reverse process however is not entirely homogeneous and crystal twinning occurs. Special attention is recommended during manufacture and processing to avoid the phase transformation. Other phases, e.g. the higher-temperature phases of tridymite and cristobalite, are not significant for oscillators. All quartz oscillator crystals are the α-quartz type [**15**], [**21**].

a) b)

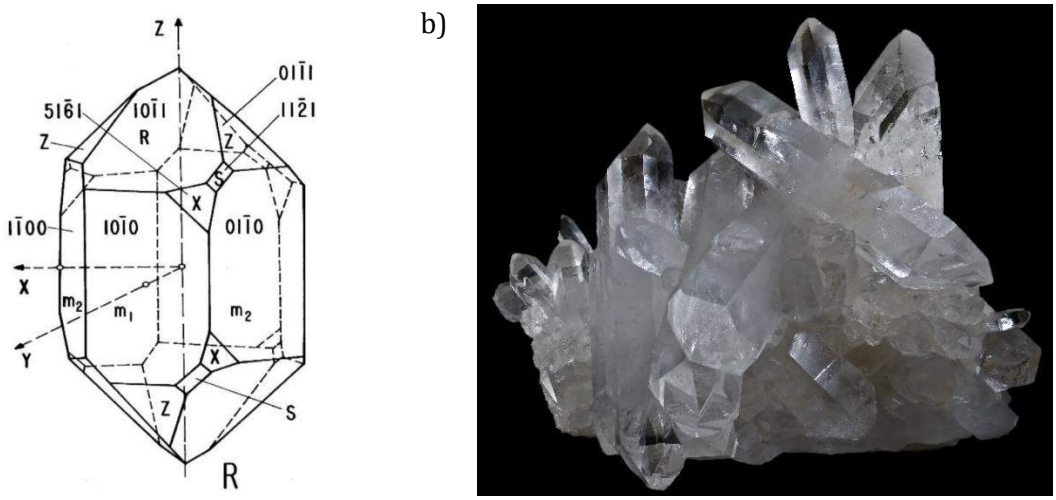

*Fig. 2.2 a) Right-hand quartz, showing natural facets b) Cluster of natural quartz crystals [**76**]*

The application where quartz was used are: resonators, filters, delay lines, transducers, sensors, signal processors, and actuators.

Nowadays, the piezoelectric ceramics are produced mainly from zirconate titanate (PZT). Ceramic materials have several advantages over single crystals, especially the ease of manufacturing in a variety of shapes and sizes. In contrast, single crystals must be cut along certain crystallographic directions, what limits the possible geometric shapes. A piezoelectric ceramic material consists of small grains (crystallites), in which the polar direction of the unit cells are aligned. Before polarization, these grains and the areas are oriented randomly, so that the overall polarization of the material is zero. Therfore, the piezoelectric ceramics do not exhibit piezoelectric properties. The application of a sufficiently high field (called polarization process), will collocate electric potential of the crystal grains similarly to the direction of the

field. When the remnant polarization is used, then the material exhibits a piezoelectric effect (Fig. 2.3 and Fig. 2.4). The piezo polymers polyvinylidene fluoride (PVDF or PVF2) are a special class of fluoropolymer that have a high level of piezoelectric activity. They are used to produce piezoelectric thin films (less than 30 microns), which can be laminated on the structural material [**4**], [**76**].

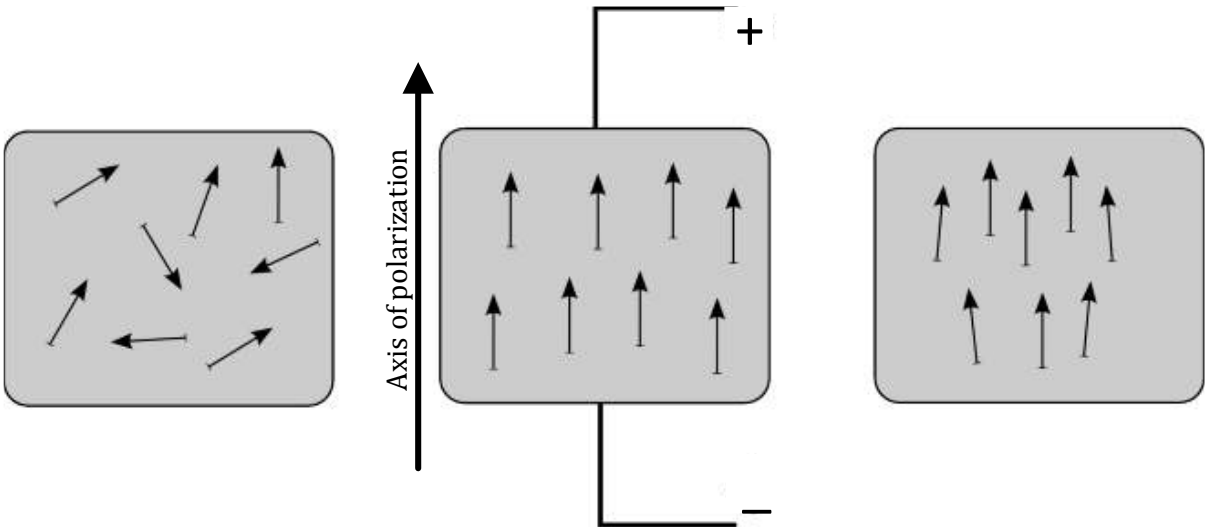

Fig. 2.3 Electric dipoles in the piezoelectric materials before, during and after polarization.

2.2.1 TEMPERATURE LIMITS

Important issue that should be considered is a Curie temperature. It is a point which corresponds to the temperature where the material loses his piezoelectric qualities due to the excessive agitation of the molecules. This point is very relevant because it severely limits the operating temperature of piezoelectric ceramics. In general, piezoelectric ceramics are properly working in the half of the Curie temperature [**8**].

The following describes the Curie Temperature for a few selected materials:

SiO_2 ≈ 573°C,

$LiNbO_3$ ≈ 1210 °C,

$BaTiO_3$ ≈ 130°C,

PVDF ≈ 180°C,

PZT ≈ 350°C.

The parameter relevant for the piezoelectricity is also temperature sensitiveness and more particularly the relative permittivity, which varies in an order of magnitude of $5 \cdot 10^{-3}$ per one degree for PZT [**26**], [**78**].

2.2.2 VOLTAGE LIMITS

The voltage limit of the piezoelectric ceramic depends on the level of electrical field applied. If imposed electrical field is too high, ceramic is depolarized, losing the piezoelectric properties.

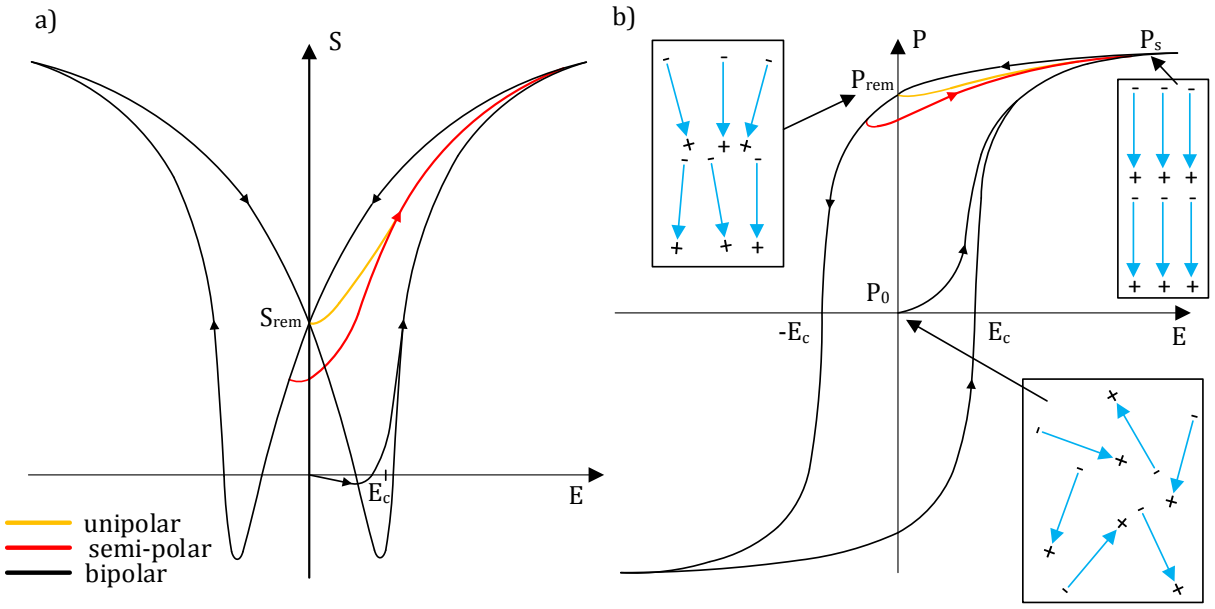

Fig. 2.4 a) Electromechanical behavior of the longitudinal strain S b) dielectric behavior of the polarization P

Before the first polarization, the electrostatic dipoles are deployed randomly in the material so the polarization of the internal field of ceramics (point P_0) is zero. During the polarization process, the material passes successively from zero to maximum polarization (point P_s). After the polarization the point is set on the phase of remnant polarization (point P_{rem}), which has been shown in Fig. 2.4.

2.2.3 PRESSURE LIMITS

There are two types of pressure limits. The first one, is the depolarization where the internal electric field in the ceramic is greater than the depolarization field which causes a depolarization of the ceramic. The second limit, is the limit where mechanical pressure or high excessive force causes a deterioration of the ceramics. The pressure limit is more important than the yield strength (generally by a factor of 10), which explains that the piezoelectric ceramics generally work under preloading [**5**].

2.3 PIEZOELECTRIC CONSTITUTIVE EQUATIONS

The nature of the piezoelectric effect is closely related to the occurrence of electric dipole moments in solids. The piezoelectric phenomenon is manifested by the conversion of electrical energy into mechanical energy and vice versa [**72**]. When an electric field (E) and a field of mechanical stress (T) are applied to the piezoelectric materials, two things happen:

- mechanical deformation S which can present itself as a translation or rotation respectively along the axes x, y and z.
- a variation of the electric displacement D around the remnant polarization P_{rem}.

Piezoelectricity is the combined effect of the electrical behavior of the material and Hooke's Law [**25**]:

$$D_n = \varepsilon_{nm} E_m$$
$$S_j = s_{ij}^E T_j \tag{2.1}$$

At the beginning of the most important factors will be presented:

- S_{ij} is the strain tensor (m)
- T_{ij} is the stress tensor (N/m^2)
- E_i is the electric field vector (V/m)
- D_i is the electric displacement field vector (C/m^2)
- ε_{ij} is the permittivity tensor (F/m)
- β_{ij} (ε^{-1}) is the impermittivity components tensor (m/F)
- c_{ijkl} is the elastic stiffness constant tensor (N/m^2)
- s_{ijkl} (c^{-1}) is the elastic compliance constant tensor (m^2/N)

The s and c are obtained in the absence of electric field (E = 0) or charge (D = 0). Although, the ε and β obtained in the absence of mechanical strain (S = 0) or stress (T = 0).

Constitutive equations of piezoelectric materials for one medium dimension could be written as the tensorial representation of the strain–charge displacement form:

$$S_{ij} = s_{ijkl}^E T_{kl} + d_{kij} E_k$$
$$D_i = d_{ikl} T_{kl} + \varepsilon_{ik}^T E_k \tag{2.2}$$

In general the piezoelectric materials have 21 independent elastic constants, 18 independent piezoelectric constants and 6 independent dielectric constants [**25**]:

- e_{ijk} is the piezoelectric constant for stress-charge (N/m^2)
- d_{ijk} is the piezoelectric constant for strain-charge (m/V or C/N)
- g_{ijk} is the piezoelectric constant for strain-voltage (Vm/N or m^2/C)
- h_{ijk} is the piezoelectric constant for stress-voltage (V/m N/C)

Other forms of the constitutive equations are:

stress-charge:

$$T_{ij} = c_{ijkl}^E S_{kl} - e_{kij} E_k$$
$$D_i = e_{ikl} S_{kl} + \varepsilon_{ij}^S E_k \tag{2.3}$$

strain-voltage:

$$S_{ij} = s_{ijkl}^D T_{kl} + g_{kij} D_k$$
$$E_i = -g_{ikl} T_{kl} + \beta_{ik}^T D_k \tag{2.4}$$

stress-voltage:

$$T_{ij} = c_{ijkl}^{D}\, S_{kl} - h_{kij}\, D_k$$
$$E_i = -h_{ikl}\, S_{kl} + \beta_{ik}^{S}\, D_k \tag{2.5}$$

Indexes *i, j* = 1, 2, 3, …, 6 and *k*, *l* = 1, 2, 3 are different directions within the material coordinate system shown in Fig. 2.5.

And matrix form:

$$\begin{bmatrix} S \\ D \end{bmatrix} = \begin{bmatrix} s^E & d^t \\ d & \varepsilon^T \end{bmatrix} \begin{bmatrix} E \\ T \end{bmatrix} \tag{2.6}$$

Furthermore, [d] is the matrix for the direct piezoelectric effect and [d^t] is the matrix for the converse piezoelectric effect. First elements after the equations refer to the mechanical properties of an elastic body and to electric properties of a dielectric medium. Artificial piezoelectric materials obtain remnant polarization in the process of poling [**6**], [**72**].

2.4 COUPLING FACTOR/COEFFICIENT AND DIFFERENT MODES

The ability of a transducer to convert the energy is characterized by the coupling factor *k* [**74**]. It characterizes the quality of the electro-mechanical conversion in the piezoelectric material and therefore the ability of the oscillator to convert electrical energy into mechanical energy. Considering the density of mechanical energy W_M, electrical energy W_E and electromechanical energy W_{EM}, *k* is defined as:

$$k = \sqrt{\frac{W_{EM}^2}{W_E \cdot W_M}} \tag{2.7}$$

In the case of an energy conversion involving only the piezoelectric material, the coupling coefficient can be expressed in terms of electromechanical material parameters and by mode of deformation considered by:

$$k_{ij} = \sqrt{\frac{d_{ij}^2}{\varepsilon_{ii}^T\, s_{jj}^E}} \tag{2.8}$$

Artificial piezoelectric materials acquire a remnant polarization through the process of polarization. The direction of polarization is the direction of electric field. This direction is marked by convention, the Z-axis orthogonal system *x, y, z* (Fig. 2.5). The indexes 1, 2 and 3 are linked to these axes, respectively. Indices 4, 5, and 6 are used to describe the shear identified in the directions 1, 2 and 3. Modes couplings can then be defined theoretically by constants with two indices. The first index *i* in coupling factor corresponds to the direction of the applied electric field, and second *j* is the axis where deformation take place [**30**], [**40**].

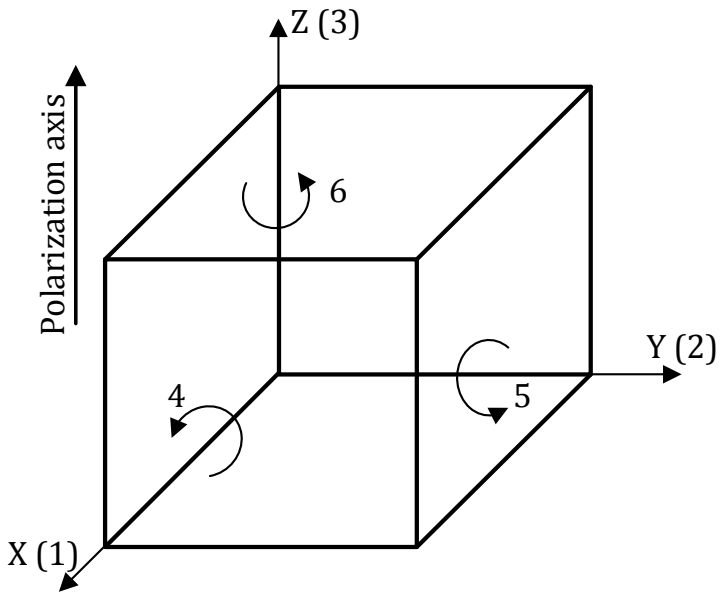

*Fig. 2.5 Modes of the piezoelectric material [**62**]*

As was stated the piezoelectric ceramics are characterized by electromechanical coupling coefficient *k*. The direction of deformation can be done in several directions that can be classified in three main ways (Tab 2.1):

1. the longitudinal mode (mode 33), results in a change in length along the axis 3, when an electric field is applied along the same axis by means of electrodes placed on the sides perpendicular to this axis,
2. the transverse mode (mode 31 or 32), leads as well to a change in length along the axis 1 when an electric field is applied along the axis 3,
3. shear mode (mode 15), leads to a shear deformation around the axis 2 when an electric field is applied along the axis 1.

The movement depends on the geometry and the relative orientation of the crystal axes and the position of the electrodes. Electrical field has an elongation in that direction and contraction in the perpendicular direction. The reverse field causes contraction in the direction of the field and an elongation in the perpendicular direction. The d_{33} mode provides three times stronger displacement than the d_{31} mode [**72**].

Tab. 2.1 Different modes of coupling in piezoelectric materials

Longitudinal mode	
$S_3 = s_{33}^E T_3 + d_{33} E_3$ $D_3 = d_{33} T_3 + \varepsilon_{33}^T E_3$ $k_{33} = \sqrt{\frac{d_{33}^2}{\varepsilon_{33}^T \cdot s_{33}^E}}$	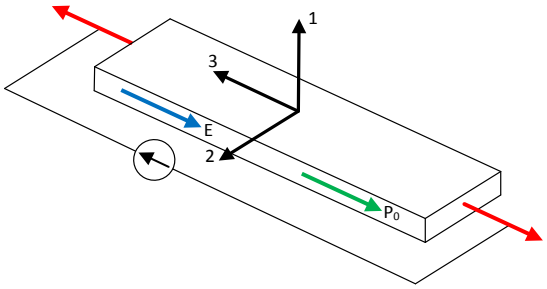
Transverse mode	
$S_1 = s_{11}^E T_1 + d_{31} E_3$ $D_3 = d_{31} T_1 + \varepsilon_{33}^T E_3$ $k_{31} = \sqrt{\frac{d_{31}^2}{\varepsilon_{33}^T \cdot s_{11}^E}}$	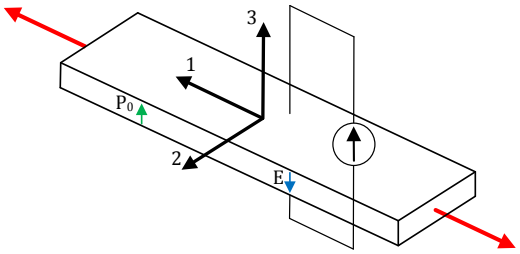
Shear mode	
$S_5 = s_{44}^E T_5 + d_{15} E_1$ $D_1 = d_{15} T_5 + \varepsilon_{11}^T E_1$ $k_{15} = \sqrt{\frac{d_{15}^2}{\varepsilon_{11}^T \cdot s_{44}^E}}$	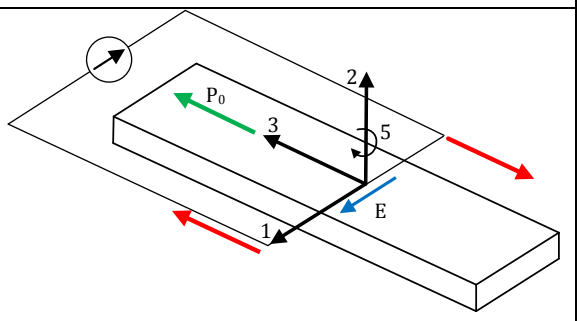

On the Tab. 2.1 the properties of some piezoelectric material samples have been presented. Following the values from the table, the coupling factor k_{33} is the most relevant in terms of coupling and should be preferred whenever possible.

*Tab. 2.1 PTZ material properties samples [**79**], [**80**]*

Model	**Type**	**Coupling factors**			**Curie Temperature [°C]**	**Piezo charge coefficients [10^{-12} C/N]**	**Dielectric constants (1 kHz)**
		k_{15}	**k_{33}**	**k_{31}**		**d_{33}**	**ε_{33}**
PZT-4D	Soft PZT	0.62	0.71	0.33	310	360	1280
PZT-8	Hard PZT	0.57	0.68	0.34	320	280	1000
P189	Traditional Hard PZT	0.51	0.65	0.32	320	240	1150
P762	Traditional Hard PZT	0.58	0.68	0.35	300	300	1300
P188	Traditional Soft PZT	0.62	0.75	0.37	340	425	1850
Pz27	Traditional Soft PZT	0.59	0.70	0.33	350	425	1800
Pz37	Low-Acoustic Impedance Family	0.35	0.60	0.15	370	350	1150
Pz46	High Temp PZT	0.03	0.09	0.02	650	18	120

2.5 RESONANCE MOTORS

Modern piezoelectric motors/actuators are generally built using either quasi-static or resonance operating topologies. There are several types of those piezoelectric motors – traveling wave motor, rotation mode motor, quasistatic motor - but they all have a similar principle of operation. When they work in a step by step mode those structures rarely generate rated torque greater than tens of Nm. However, they exhibit interesting properties in terms of torque per mass ratio and relatively small dimensions compared to electromagnetic motors. The detailed comparison of those structures will be discussed in the following paragraphs [**7**].

In Fig. 2.6 it is shown the classification of motor/actuators technologies according to the force vs. velocity characteristics. Electroactive motors/actuators which have the highest energy density are based on the piezoelectric ceramics or magnetostrictive ceramics [**45**].

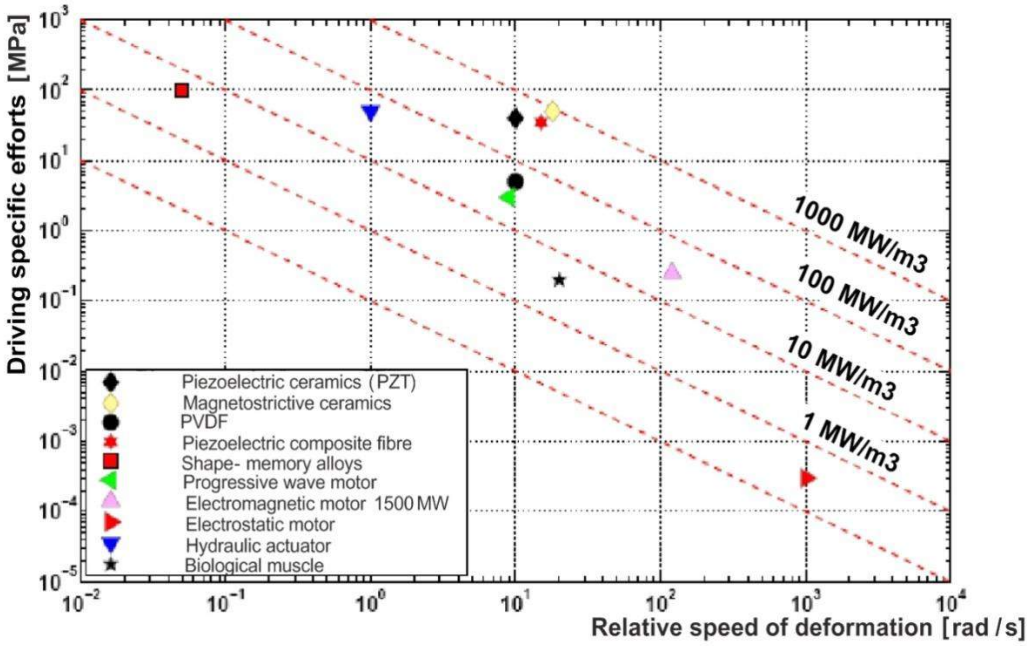

*Fig. 2.6 Comparison of the various electromechanical effects in terms of specific energy [**45**], [**53**]*

Piezoelectric motors are based on the conversion of mechanical high-frequency oscillations (tens of kHz) in a continuous movement and are interesting for applications where the functional integration, and reduced mass are required. Piezoelectric materials can be used as oscillators (quartz crystal), and in the case of piezoelectric motors, usually PZT ceramics are implemented [**44**], [**67**]. An ultrasonic motor is a transducer where a mechanical vibration in the ultrasonic wave range is used as its driving source.

The advantages of piezoelectric motors are following: high torque, high resolution, excellent control, a small time constant, compactness, high efficiency, quiet operation, and no electromagnetic field. In Fig. 2.7 the principle operation of an traveling wave motor (flexural traveling wave ring-type motor) is shown as an example. Using a resonance mode of the mechanical structure enables the transformation of micro displacements and movement to large amplitudes.

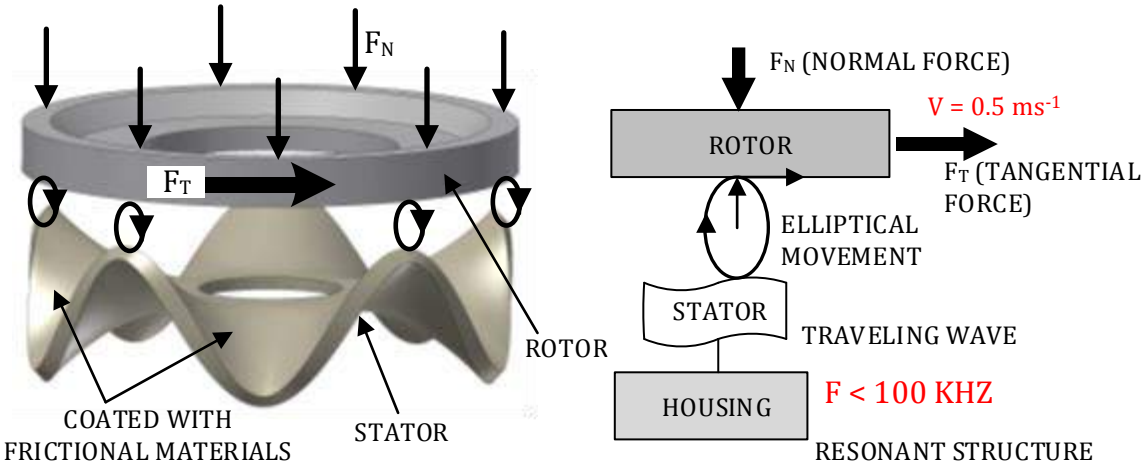

*Fig. 2.7 Operation principle of the traveling wave type motor [**42**]*

Generally the piezoelectric motors/actuators are composed of four parts: stator, rotor, piezoelectric ceramics and power supply. The stator consists of piezoelectric material associated with a mechanical structure. Piezoelectric material structures are properly supplied by a two-phase source of voltage and therefore deformed at a frequency corresponding to the mechanical resonance frequency of the structure to which they are associated by adhesive bonding or preload. Thus, the initial deformation of ceramics is amplified by the effects of the resonance of the mechanical structure. Stator's final deformation is sinusoidal and is gradually becoming the two-phase supply areas of ceramics. The rotor is a mechanical part, which is held in contact with the stator by a constraints (screw).

The point trajectory of contact between the stator and the rotor is described by an ellipse. This ellipse can be modeled by a wave of the form:

$$u = A\cos(n\theta + \omega t) \tag{2.9}$$

Where ω is the vibration frequency, θ is phase angle and A is vibration amplitude.

A traveling wave may result from the sum of two standing waves [**41**]:

$$u = u_1 + u_2 = V\sin(\omega t)\cdot\sin(n\theta) + V\cos(\omega t)\cdot\cos(n\theta) \tag{2.10}$$

The elliptical motion is decomposed into two components:

- normal, which controls the frictional force by compensating the axial force applied by a spring F_N on the moving part,
- tangential, which induces the driving force expressed by Coulomb's law $F_T = \mu F_N$.

2.5.1 ULTRASONIC MOTORS

In office equipment such as printers and disk drives, market research indicates the potential application of motors with a volume of 1 cm^3 [**35**], [**74**]. Ultrasonic motors have better properties compare to classical electrical motors – torque/mass ratio and high resolution. The principle of operation of the motor is based on the wave generation on the stator by a piezoelectric ceramic ring (usually it is lead zirconium-titanate-compound – PZT) glued to the back of the drive ring. The operation depends on friction at the interface between the moving rotor and stator. To extended lifetime of the motor, a design of the specific and precision construction of the stator is necessary [**3**], [**23**].

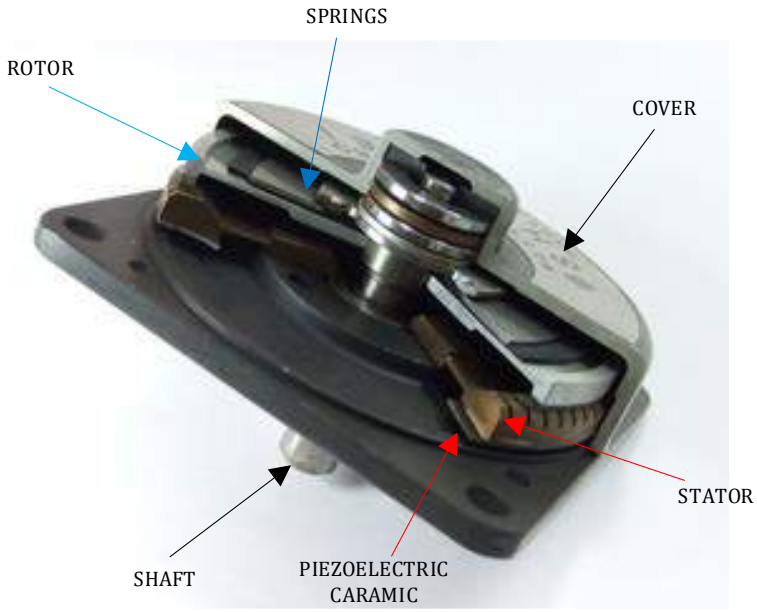

*Fig. 2.8 Exploded view of a ultrasonic motor **[81]***

The stator has ring type construction with teeth on it. Teeth are arranged in a ring at the radial position and are intended to form a moment arm to amplify the amplitude of displacements, so increasing the speed. To generate a traveling wave within the stator two orthogonal modes are activated simultaneously. The rotor is driven by friction. This type of motor uses specific kinematics at the level of interface between the rotor and stator. Produced forces are a priori weaker. The points at the rotor/stator contact surface are oscillating in an elliptic way. Generally, the stator is made of beryllium-copper and the rotor from duralumin (Fig. 2.8) [**32**], [**64**].

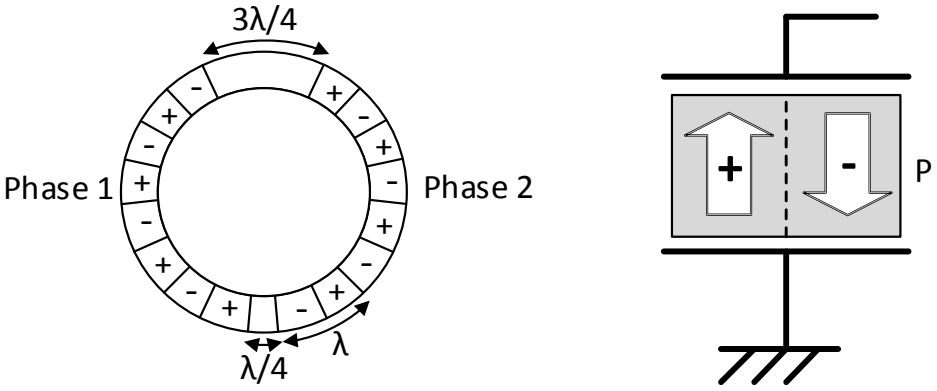

*Fig. 2.9 Sectorization of a piezoelectric ring in ultrasonic motor **[42]***

There are two sets of electrodes, each having eight sectors of width $\lambda/2$. The second set is shifted $\lambda/4$. These modes are induced by a stator that is constructed with the drive piezoelectric actuators in the form of two sections of poling pattern that are bonded to the stator. Geometrical examination of this pattern shows that driving the two sections using $sin(\omega t)$ and $cos(\omega t)$ supplying signals, respectively, will produce a traveling wave with a frequency of $\omega/2p$. Also, by

changing the sign on one of the drive signals, the traveling wave would reverse its direction (Fig. 2.9) [**22**].

The advantages of travelling wave motors are following: silent operation due to excitation in a field of inaudible frequencies (>20 kHz), relatively low speed (requiring no gear) and short response times (a few ms) at startup and braking provide excellent dynamic control position or speed. Another advantage is torque/mass high ratio (>10 Nm/kg). In this kind of stator structure appears a technological problem, because the bond between the ceramic and the metal is provided by a glue joint [**11**], [**46**].

Canon was one of the pioneers of the ultrasonic motor (motor annular wave - USM) [**82]**. The motor is used to controlling the auto focus - AF (Fig. 2.10). Camera's autofocus lenses are driven by these small piezoelectric motors. The stator of this motor is composed of a metal ring which is bonded on a ceramic PZT exciting a bending mode of row 9. The rotor is driven by friction at nine sliding contact points (nine traveling wave are generating). The ring-type USM is actually very simple in operation and interesting in terms of integration within the autofocus. By applying a AC signals with a resonance frequency about 40 kHz to the structure, vibrations are created, causing the rotor is rotate continuously. Depending on the model, Canon uses three types of ultrasonic motor: ring type, micro USM I and II with a gear unit.

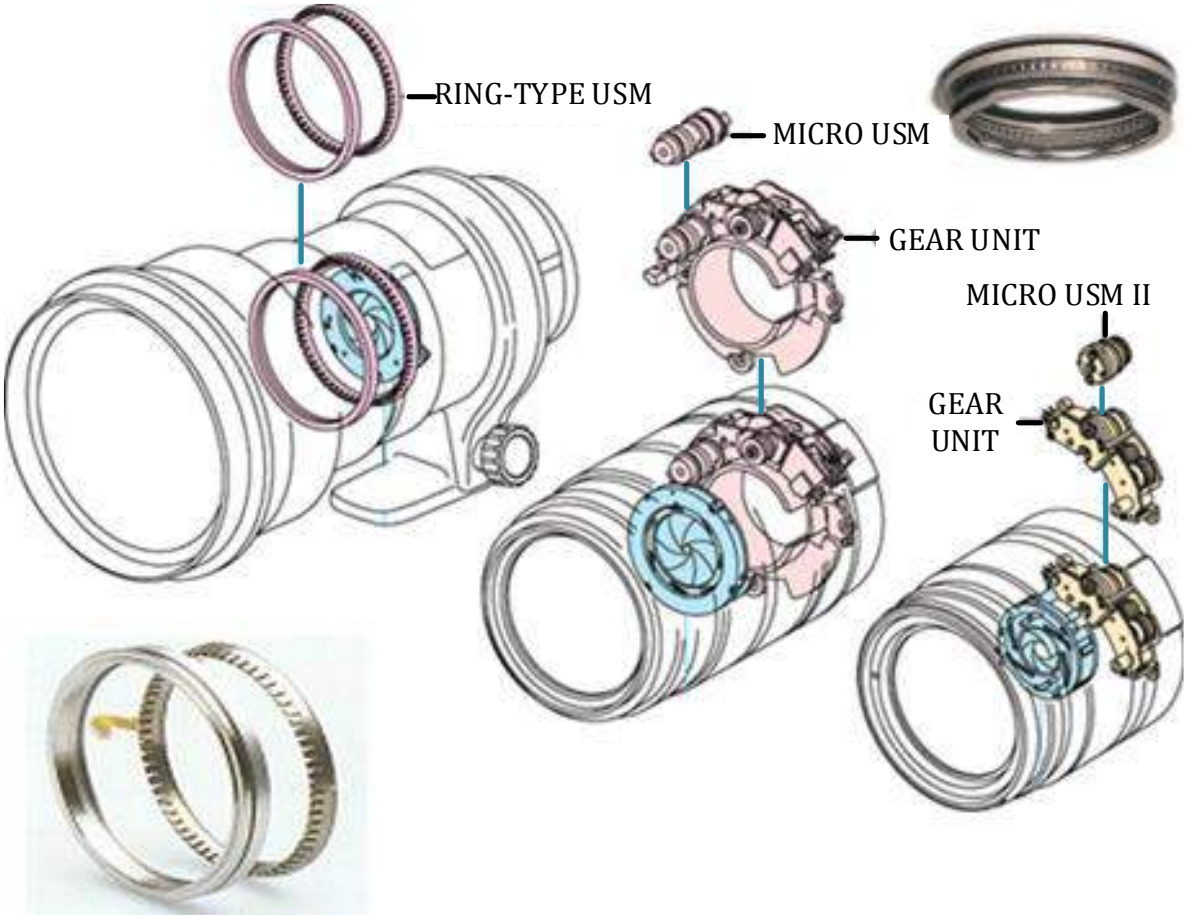

*Fig. 2.10 The three types of USM motor used in Canon cameras [**82]***

2.5.2 ROTATING-MODE MOTOR

The rotating-mode motor (Fig. 2.11) consists of the same parts as a Langevin type transducer, which is basically composed of one or more pairs of piezoceramic rings sandwiched between two metal counter-masses (stator). In addition, the rotating-mode motor has one or two rotor [**42**].

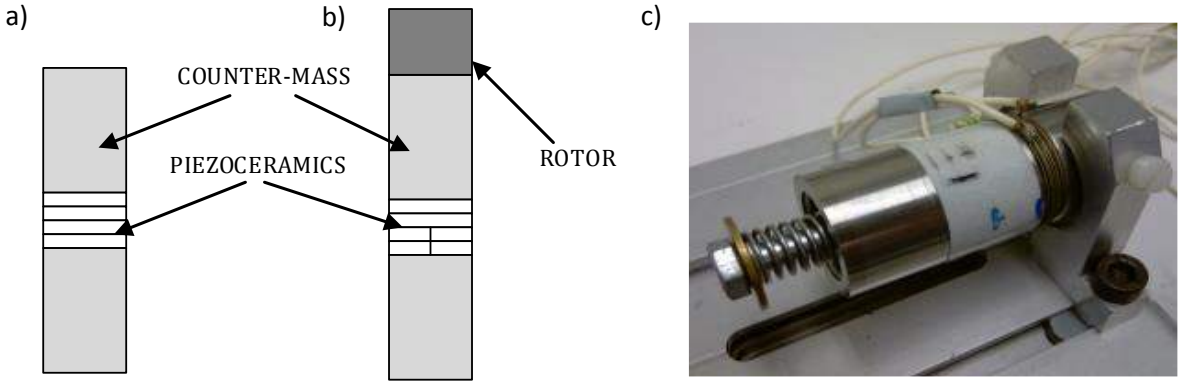

Fig. 2.11 The structures of the: a) Langevin's transducer b) rotating-mode motor c) rotating-mode motor prototype (LAPLACE Laboratory)

The difference is in the excited mode: in rotation-mode motor the mode of flexion exists, whereas Langevin type transducer - longitudinal vibration modes. The stator of a rotating-mode motor uses two modes of bending (Fig. 2.12). The ceramics are discs with opposing polarization on each half. The whole structure is prestressed by a screw.

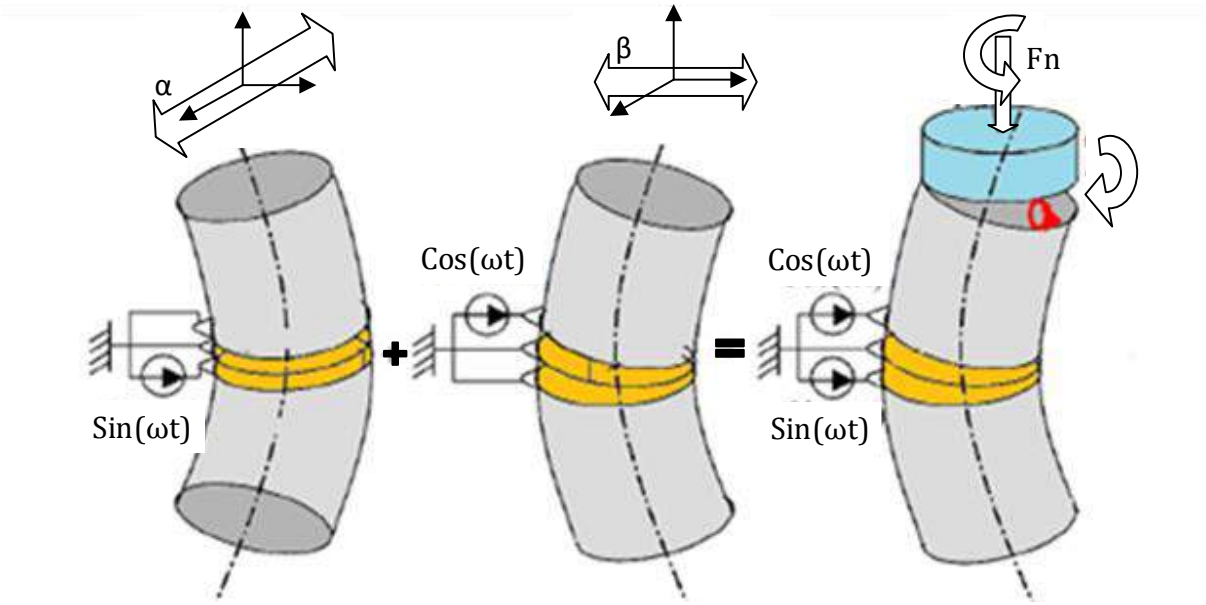

*Fig. 2.12 Operation principle of a rotating-mode motor [**42**]*

The two sinusoidal high frequency phase shifted voltage sources are used to supply the ceramics structures. The ceramics are oriented at each other by 90° (Fig. 2.13). Following this conditions, the traveling wave is generating. The traveling wave is amplified by the counter-mass. Generated

traveling wave is in contact with the rotor on the stator in any time. The rotor (like in ultrasonic motor) is driven by friction [**66**].

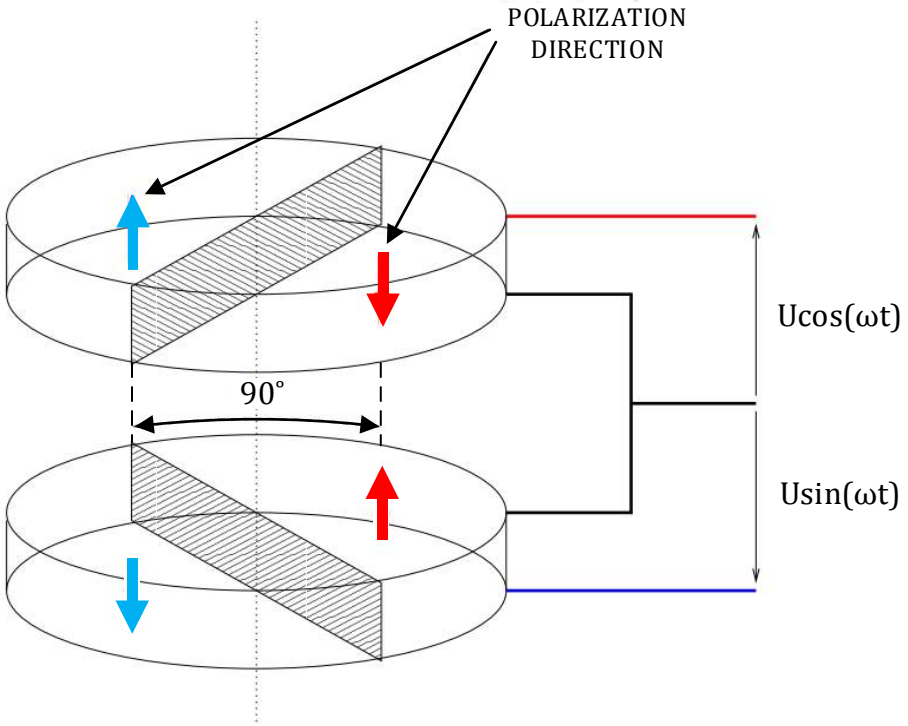

*Fig. 2.13 Piezoceramics arrangement in rotating-mode motor [**10**]*

The main advantages are the high torque to mass ratio (10 N/kg), a blocking torque, small number of parts (simple structure) and low weight .

A good example of this motor type is the piezoelectric rotating mode motor with high torque density developed in LAPLACE Laboratory in Toulouse. The project was carried out with cooperation between Airbus and LAPLACE in Toulouse. The goal was to create a new concept of piezoelectric rotation mode actuator with high torque density and that is dedicated in aeronautical application areas. The project name was "Future Flight Control" [**70**] – [**72**].

For the above case the rotating-mode motor structure is suitable to use because it has simple design and possibility to adjust the preload to piezoceramics to maximize their potential. Other advantage is rotor/stator contact on the entire surface. To increase the properties of the actuator the second rotor has been used due to symmetrical structure. In addition the uses the double rotor it is possible to obtain better force control. The counter-mass (stator) has been made from aluminum alloy AU4G type, to reduce the weight of the actuator. Moreover, this material allows to reduce the mechanical losses comparing to steel. The rotors were made of steel, because the material of high density was necessary. The rotor should have sufficient inertia to ensure the proper functioning of the electromechanical power conversion process. The hard ceramics of the type PC8 have been used because they do not generate much losses. The virtual prototype is presented in Fig. 2.14, and real model parts are shown in Fig. 2.15.

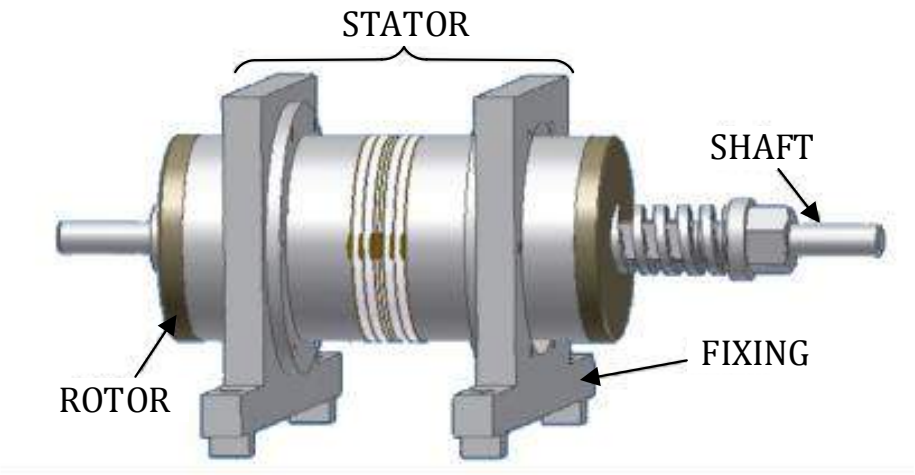

*Fig. 2.14 The virtual prototype of the piezoelectric rotating-mode actuator with high torque density [**72**]*

*Fig. 2.15 The actuator parts: a) rotor, b) stator [**72**]*

The obtained performance characteristics have shown a very interesting technological solution, i.e., the torque density was approximately 8 Nm/kg. The obtained parameters of the prototype for the supply voltage 780 V (rms) was following: velocity 52 rpm, blocking torque 4.2 Nm. The mechanical power of the actuator was around 6 W.

In addition, to supply the above motor, a dedicated frequency converter of 400 Hz and 200/115 V/V was designed (Fig. 2.16). The system has been built and tested in the laboratory with the static converter for the effective application of two voltages 600 V phase-shifted by 90° at a frequency of approximately 20 kHz [**71**].

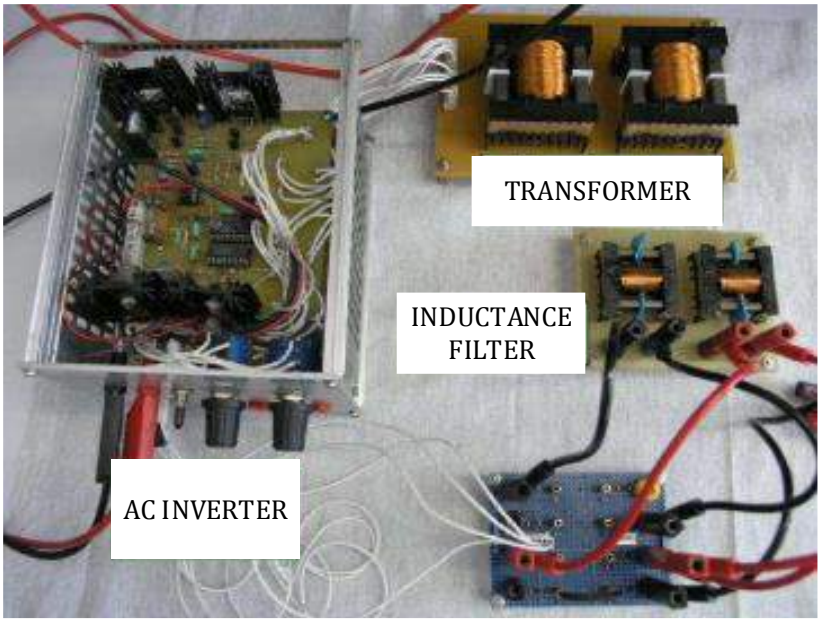

*Fig. 2.16 Power supply of the rotating-mode motor with high torque density [**71**]*

2.6 OTHER PIEZOELECTRIC MOTOR/ACTUATOR STRUCTURES

2.6.1 QUASI STATIC ACTUATORS

The principle operation of the quasi static actuators is based on the deformation of ceramics (Fig. 2.17), such as multilayer ceramics, of the order of a few microns, which are supplied with the low frequencies (below few hundreds of Hz). The multiplication of these micro displacements results in movements of larger amplitudes. This type of motors is used primarily for their nano displacement, precision and substantial generated forces. Moreover, the used kinematics is a solid and low speed ($\approx 3 \div 10$ mm.s^{-1}). Thus, the contact imposes the coefficient of a static friction. This kind of motor usually consists of three parts: clips, gripers and piezoceramics changing distance between two previous parts [**18**], [**63**], [**69**].

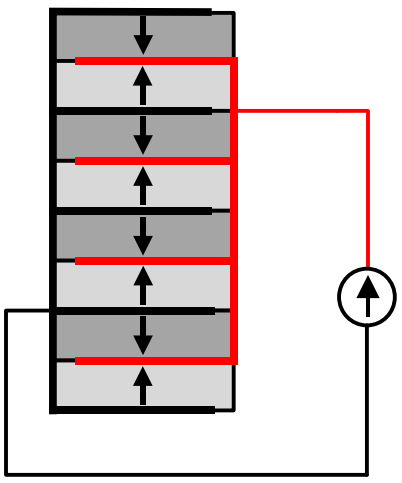

*Fig. 2.17 Multilayer ceramic [**42**]*

The operating cycle is divided into several steps (Fig. 2.18):

1. the two grippers are gripping the guide,
2. the first gripper is released while another continues gripping the guide,
3. the actuator is extending to move the free gripper, the second gripper is fixed still,
4. then actuator reach the maximum the first gripper is going to fix,
5. the second actuator is released,
6. the actuator is shortening to move the second gripper,
7. when actuator reach the minimum the second gripper is going to fix.

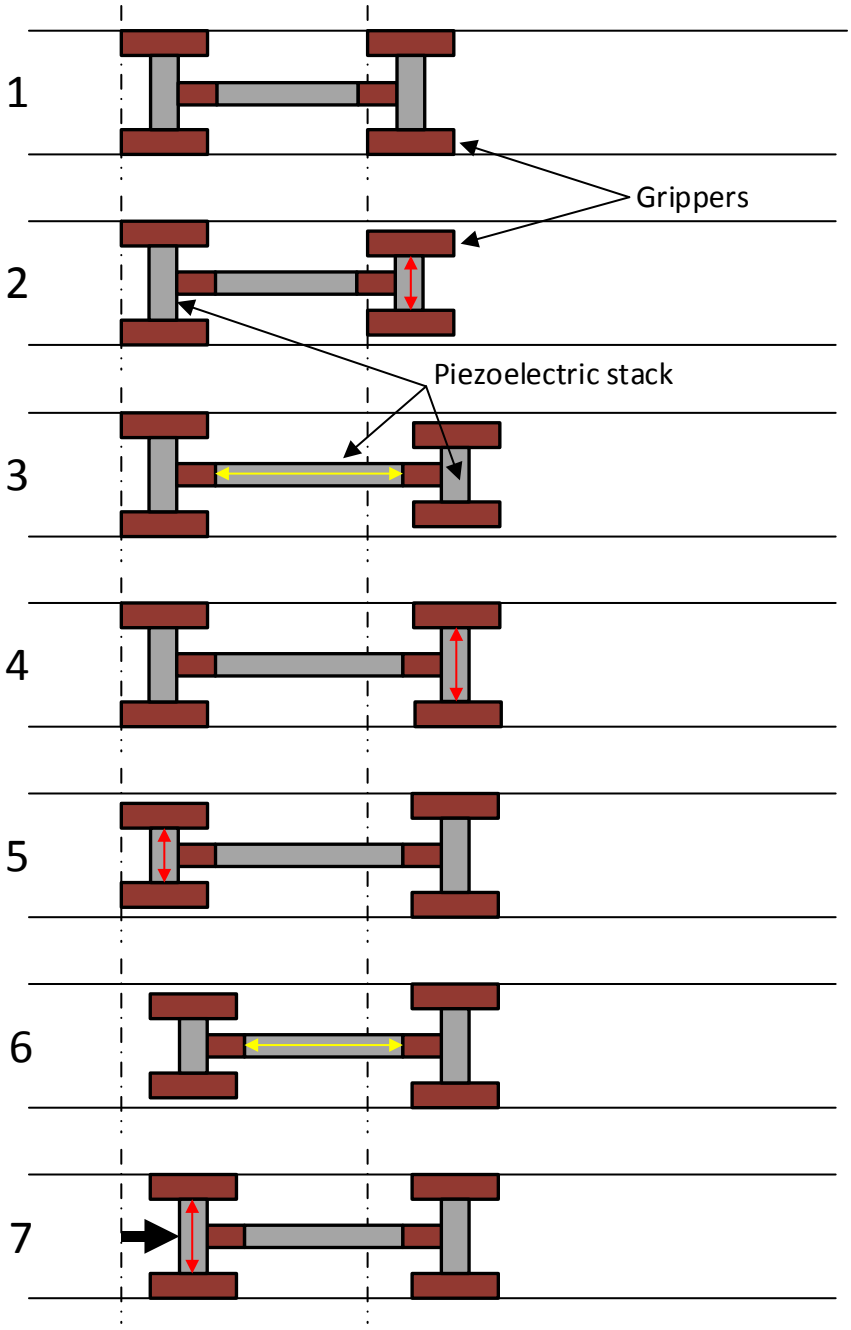

*Fig. 2.18 Operation principle of a quasi-static motor [**10**], [**69**]*

Quasi-static structures (Fig. 2.19) have some advantages: like high step resolutions which is useful for micropositioning applications, and high torque/mass density. However, they have limited power and low speed.

For the dedicated applications the quasi-static structures have been chosen to implement modification of the operating principle to overcome recurring problems of conventional structures (sensitivity to wear, poor accommodation surfaces). The electroactive lubrication between rotor and stator is also added (using the resonance piezoactuators), in order to disengage rotor and stator in the return phase.

A combination of these two topologies, i.e., using hybrid topology, can result in further advantages of piezoelectric motors. The considered hybrid piezoelectric motor is characterized by much more compact dimensions and lower weight. It exhibits higher torque per volume ratio as well as good blocking ability when is not powered. It operates at a low speeds and do not require any gear reduction system which leads to further gains in weight and volume. Finally, it can work in higher temperatures compared to the variable reluctance motor. On the other hand, while using the piezoelectric elements there is a risk of depolarization as well as a shorter life span.

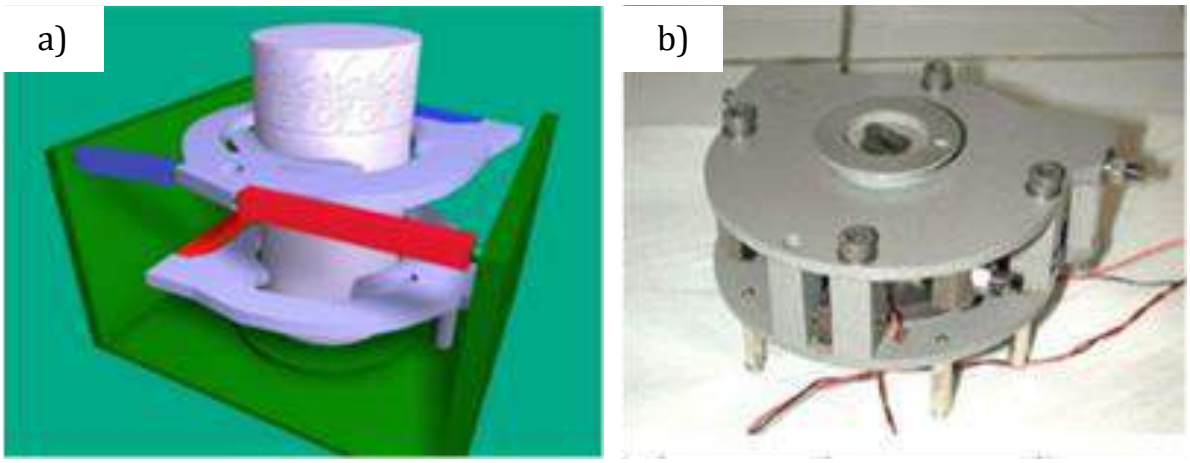

*Fig. 2.19 Quasi-static operating piezoelectric actuator: a) conception, b) prototype [**53**]*

2.6.2 ELECTROACTIVE LUBRICATION PRINCIPLE

The main idea using the electroactive lubrication is to control the friction forces between the rotor and stator [**54**]. By the vibrations (μm amplitude, a few kHz frequency) injected at the dry contact between two pieces, subjected to a certain relative speed, the frictional forces resulting from the movement between the two solid bodies are decreased. To increase motor efficiency, it is necessary to reduce the friction losses as low as possible. While keeping power consumption as low as possible it is possible to obtain a relatively high speed and vibration parameters (amplitude and frequency) [**54**].

The principle of electroactive lubrication is based on the control of the friction forces. To obtain this goal the injection of vibrations into the contact surface between rotor and stator is used. The friction control process can be divided in two main stages (Fig. 2.20):

- Contact surfaces are separated if the proper vibration magnitude is injected. For this state (indicated by interval t_1) there is no friction (friction force - $F_{fr} = 0$)
- Upon contact of the surfaces, the two bodies have to be in the state of partial slip. While there is a full slip, the entire contact surface slides (the state is indicated by interval t_2 and speed V_2). For a partial slip and the proper distribution of the pressure the central part of the body is fixed (part of the contact is indicated by a red line in Fig. 2.20: interval t_2 and speed V_1), while the peripheries of the body are sliding (part of the contact indicated by a green line in Fig. 2.20). Thus, for the partial slip the friction is involved in a smaller area than for the full slip. As a result, the friction forces are reduced when the slip is partial.

To ensure the control of the friction forces, the ball is subjected to a static normal force F_{No} and the normal force F_{vib} (due to injected vibration). Depending on the dynamically produced value of the normal force, the separation of the surfaces will be effective or not.

Respecting those constrains, explained above it is possible to specify the requirements for control of the vibration and friction in the considered hybrid piezoelectric motor.

According to the Fig. 2.21, there are two fundamental parameters of vibration excitation: amplitude and frequency. In order to determine the most efficient contact for electroactive lubrication, it is crucial to investigate the importance of those parameters. For the minimum amplitude, there is the separation of contact surfaces. However, friction forces increase for the cylinder/plane contact while they decrease for the studs/plane contact. In general, lower amplitude of vibrations leads to a smaller separation of the surfaces, which increases duration of the contact, and as a result the electroactive lubrication is less effective.

For a high excitation frequency, the apparent friction coefficient tends to decrease until a low value. For studs/plane contact, the friction forces decrease more quickly for a frequency range less important. The augmentation of the frequency of the vibrations leads to a shorter contact time and results in a more effective electroactive lubrication.

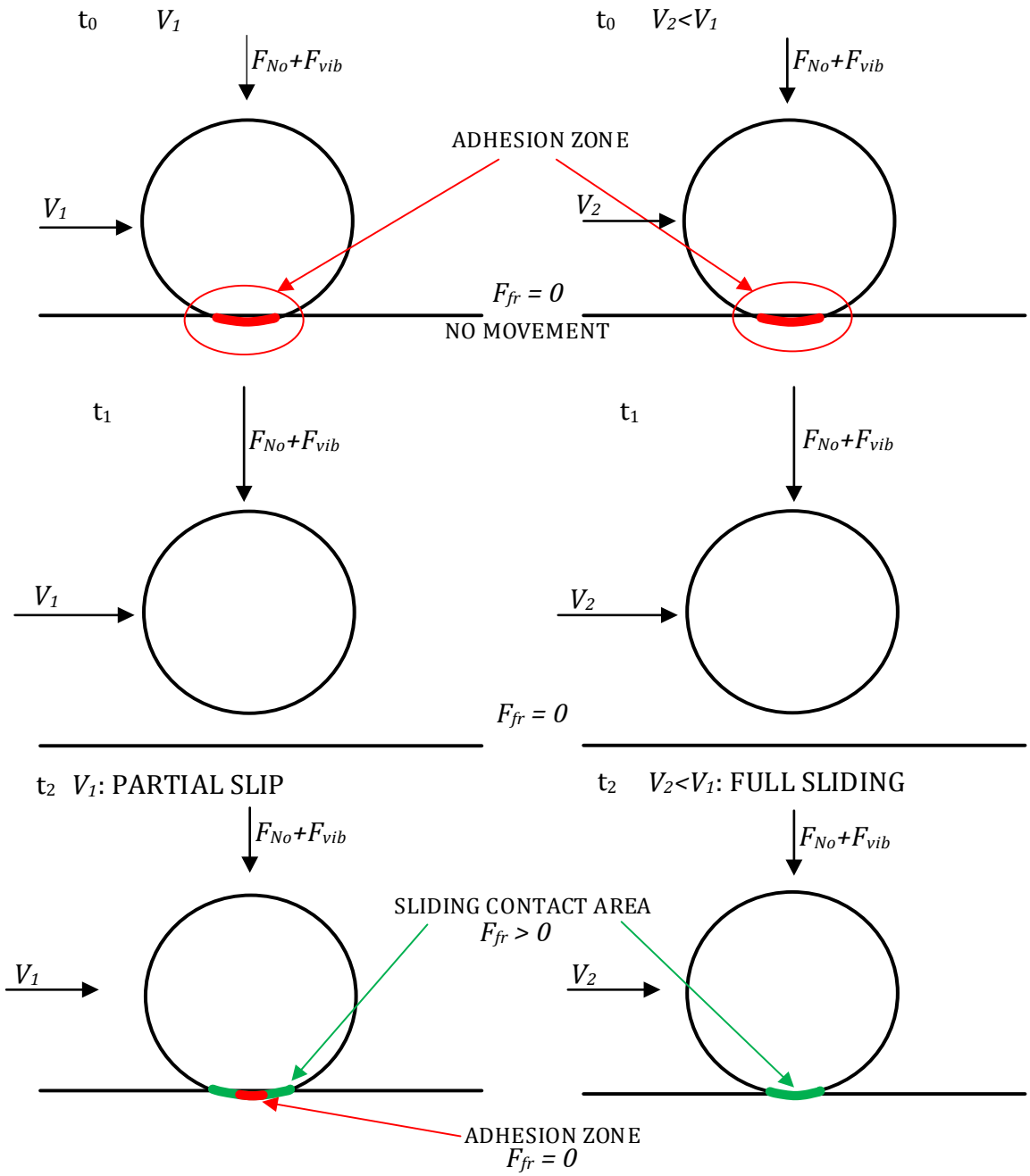

*Fig. 2.20 . Illustration of the electroactive lubrication principle applied for hybrid piezoelectric motor: V_1, V_2 – velocities of the moving body, t_0 – full adhesion interval; t_1 – separation interval; t_2 – partial or full slip interval; F_{No} – static normal force; F_{vib} –normal force due to vibration; F_{fr} – friction force [**10**]*

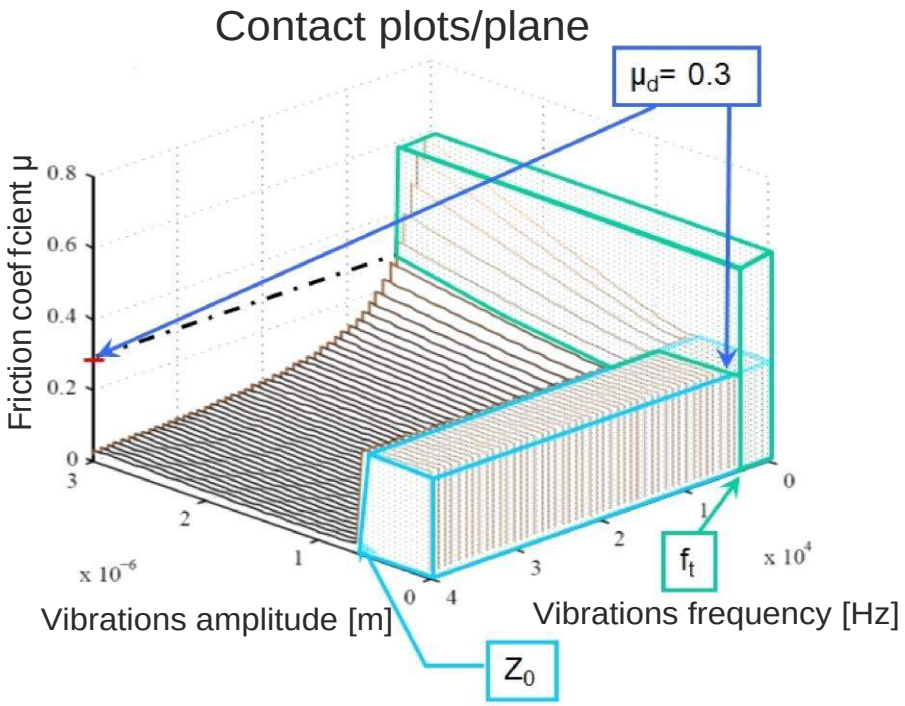

*Fig. 2.21 Evolution of the friction coefficient as a function of the amplitude and frequency of vibrations for the discretized contact; Z_0 – minimal amplitude of vibrations; f_t – minimal frequency of vibrations; μ_d – selected dynamic friction coefficient [**53**]*

The above considerations have shown that studs/plane contact (discretization of the contact surfaces) combined with the proper control of the amplitude and vibration frequencies allows to obtain the best conditions for the electroactive lubrication [**54**].

2.6.3 HYBRID PIEZOELECTRIC MOTOR BASED ON ELECTROACTIVE LUBRICATION PRINCIPLE

The detailed results of the measurements of the hybrid piezoelectric motor have been presented in papers [**60**] and [**61**]. Thus, only the most important issues will be described below.

The considered hybrid piezoelectric motor was developed in LAPLACE Laboratory. The specific applications of this motor set up the following parameters: high torque/mass ratio, small overall dimensions and light weight. Moreover, the high blocking torque, when the motor is not powered, is also required.

The hybrid piezoelectric motor (Fig. 2.23) has a basic structure composed of grippers containing resonance actuators and the exciters equipped with the multilayer ceramics.

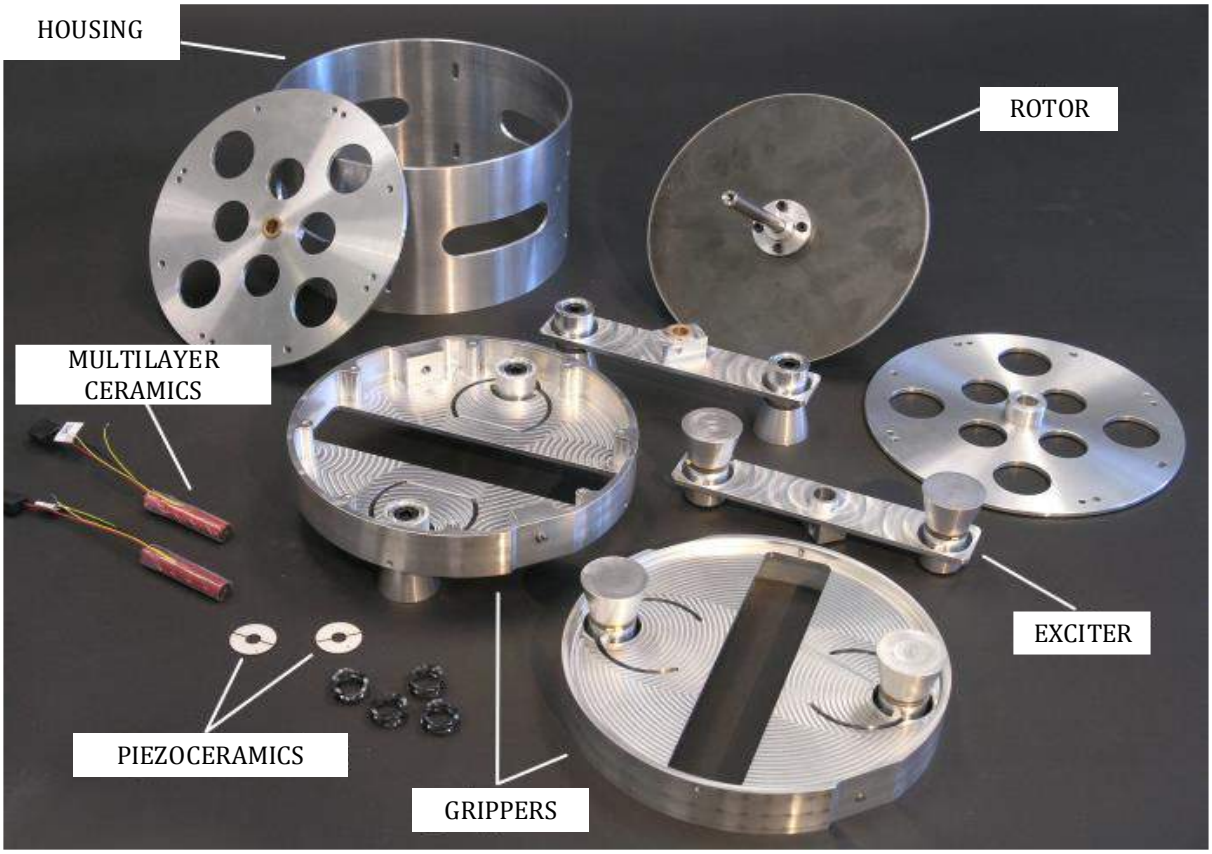

Fig. 2.22. Disassembled prototype hybrid piezoelectric motor

The hybrid piezoelectric motor (Fig. 2.23) has a basic structure composed of grippers containing resonance actuators and the exciters equipped with the multilayer ceramics.

The hybrid nature of the motor is due to using two different types of piezoelectric actuators in order to generate a rotational movement [**55**]. The driving force is generated by the exciters using the quasi-static actuators. They produce small deformations due to the operation of the high voltage multilayer ceramics. The basic step is then multiplied and drives the rotor. The purpose of the grippers is to lock and unlock the motor rotor at a specific time intervals, and also to provide the electroactive lubrication. Due to using the resonance actuators, working in the bending mode, the vibrations are injected at the level of the rotor/stator interface. This leads to lowering the parasitic friction of the motor moving structures. It also supports the hybrid motor behavior to be independent of the evolution of ambient temperature, and enables proper control of the motor performance. The half of the hybrid motor consists of one exciter (using two multi-layer ceramics) and two sets of grippers. The completed motor structure consists of those two halves and a rotor that is sandwiched between them (Fig. 2.23).

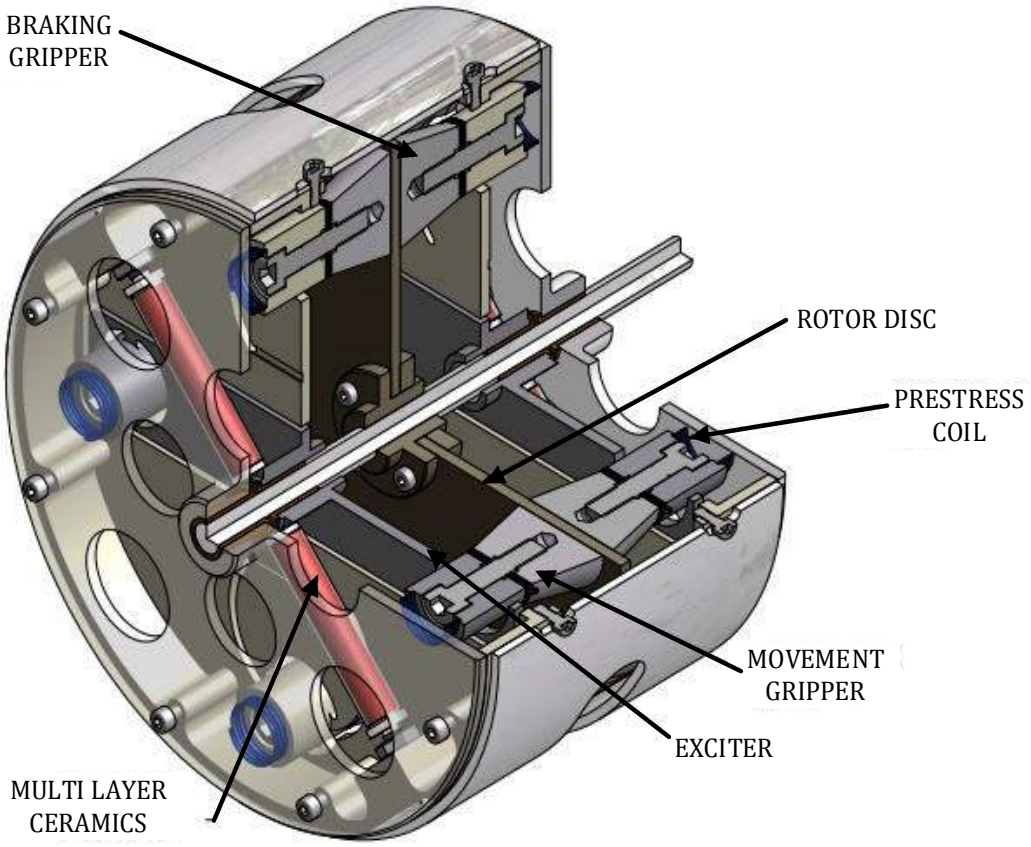

*Fig. 2.23 Virtual structure (cut away view) of the prototype hybrid piezoelectric motor **[55]***

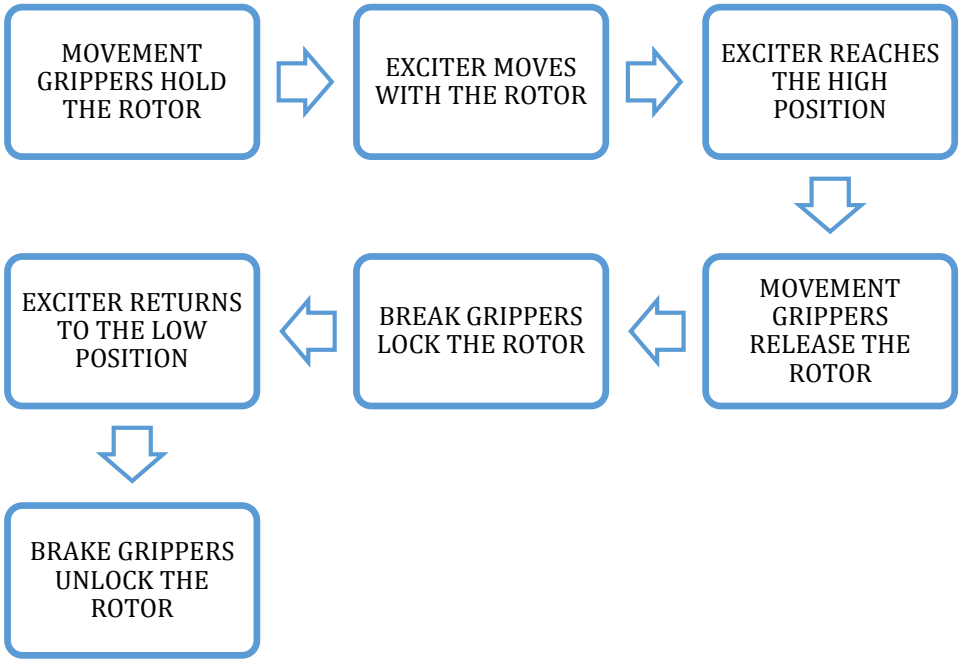

Fig. 2.24 Block diagram of the hybrid piezoelectric motor working cycle

One working cycle (Fig. 2.24) has the following operations:

- movement grippers hold the rotor when the exciter pieces move with the rotor;
- exciter pieces reach the high position level that the movement grippers can release the rotor;
- brake grippers lock the rotor and the exciter pieces return to the low position level;
- brake grippers unlock the rotor.

The assembling and tuning of the prototype hybrid piezoelectric motor have been done in the following steps:

- preparation of the ceramics;
- assembling of the resonant actuators;
- frequency matching.

The motor assembling process has the following steps: arranging piezoceramics to a specific direction of polarization to maintain the bending deformations (Fig. 2.25); bolting the stack of PZT to the metal cylinders and adjusting the prestress force in order to set the proper working frequency. As a result, the mechanical resonance of the grippers was set to 17.6 kHz and 18.6 kHz, respectively for the exciters.

Fig. 2.25 Hybrid piezoelectric motor - orientation of the ceramics and the electrode

The key aspect of the motor working principle was the proper synchronization between the actuators groups. In order to ensure the working cycle (Fig. 2.24), both braking and movement grippers should have the same resonant frequency (Fig. 2.26). The tuning process is focused on matching all the actuators to the same resonant frequency, as it is necessary for the motor to work properly. The best option is to set up all eight actuators at the same level of frequency. However, it has turned out, that due to mechanical imperfections of the surface and a low available accuracy of the frequency tuning, it was extremely difficult to set up them properly.

As it was described above, the characteristics of each motor part were set up by adjusting the prestress force acting on the actuators. The best accuracy was achieved within the range of 50-100 Hz.

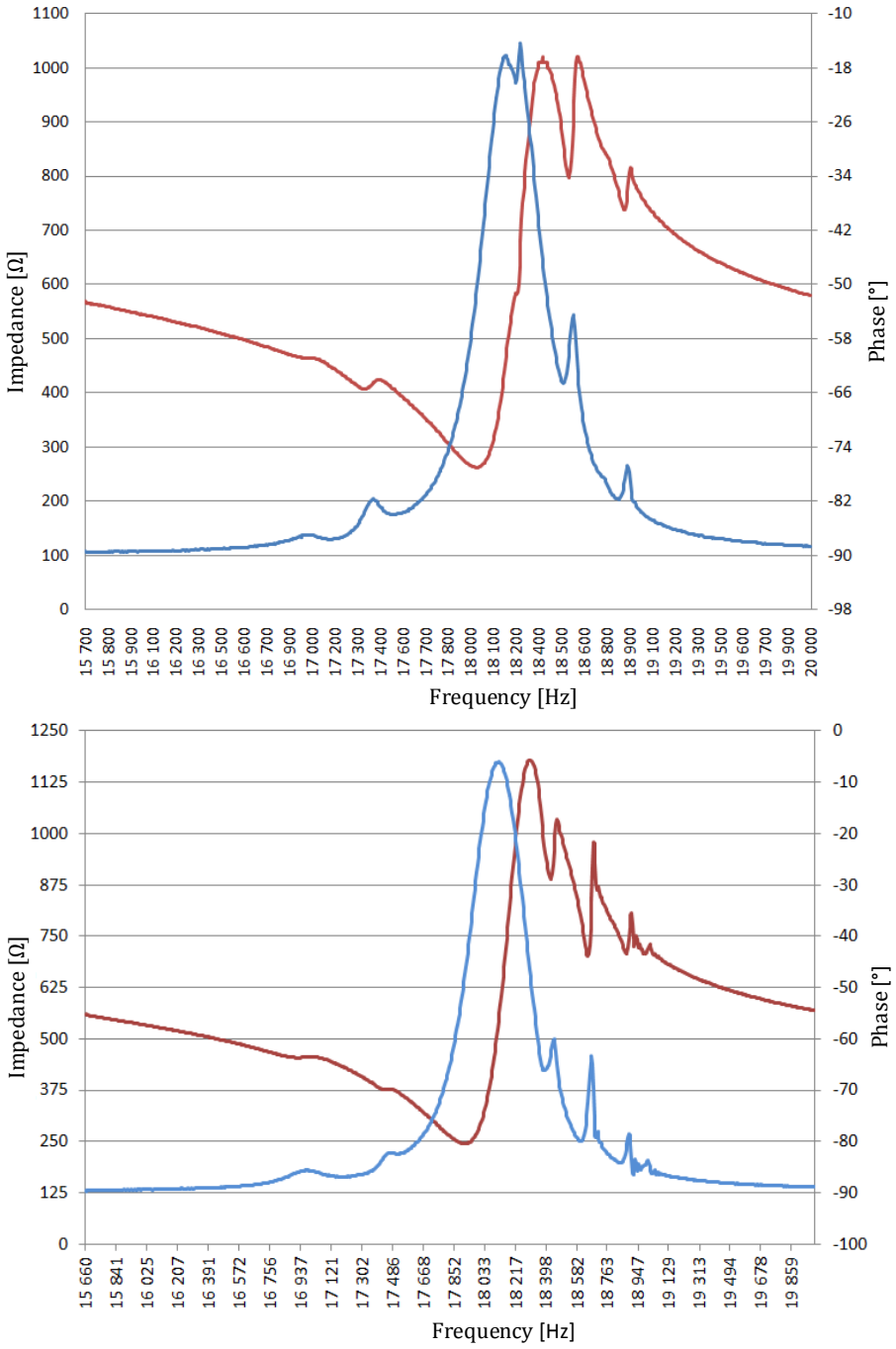

Fig. 2.26 Phase and impedance characteristics of one pair of the movement grippers (on both sides of the rotor)

The assembling process of the completed prototype motor structure has included the positioning of exciters and grippers in relation to the rotor disc as well as to the housing. It was the crucial part of the whole process as the structure needed a very high level of precision to provide the best contact conditions for the electroactive lubrication principle. The motor characteristics were mainly tuned by minor changes at the position of the multilayer piezoceramics: their angle with respect to each other and the force that they acted on the

exciters. To get the success, the key problem was to place the multilayer ceramics by an optimal way. Depending on their position, different values of displacement were obtained.

For testing the prototype hybrid piezoelectric motor a high frequency power supply system has been elaborated. The type DS1005 controller, a power converter, and type DS2004 high-speed A/D board were used. It has four inverters which can work in synchronization or independently and are supplied by a DC voltage source application of Matlab and dSPACE have enabled the control of the power supplied of the prototype piezoelectric hybrid motor. By this way, the synchronization of the multilayer ceramic's supply with the duty cycle of the piezoceramic grippers was possible. The main control program has four function blocks that are used to control the power switching process for each channel of the converter. According to the tested motor working cycle (Fig. 2.24), when exciters are working, the breaking grippers should not be fed by voltage, and vice versa. Additionally, the control of four frequencies of the movement and braking grippers was essential to maintain them in a resonance mode and to ensure the proper work of the motor. The motor supplying voltage waveforms are shown on the Fig. 2.27. It represents the synchronization of the power supply between the multilayer ceramics and the grippers based on resonance actuators. For this mode of supply, the amplitude of supplying voltage for the piezoceramic grippers was about 200V at the frequency of 17.6 kHz and 18.6 kHz and the excitation frequency of multilayer ceramics was about 90 Hz (Fig. 2.27).

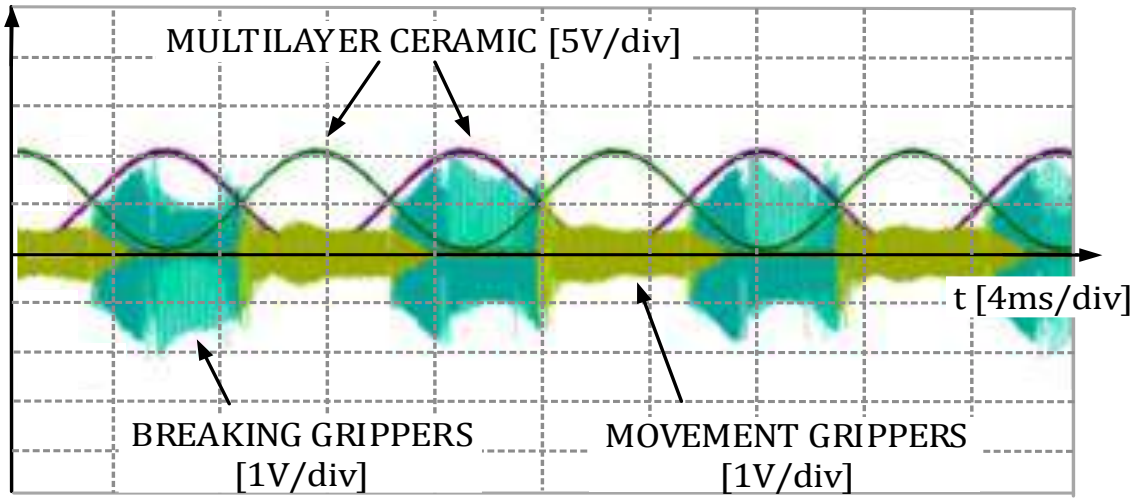

Fig. 2.27 Measured supply voltage waveforms of the multilayer ceramic and both grippers of the tested prototype hybrid piezoelectric motor for two modes of performance: braking/blocking, and rotation/movement at no-load

The tested prototype hybrid motor, having two sets of grippers, has generated the starting torque of 3.5 Nm, when rotor was braked/blocked (Fig. 2.28). By increasing the number of the grippers in the tested motor, it is possible to increase the developed torque.

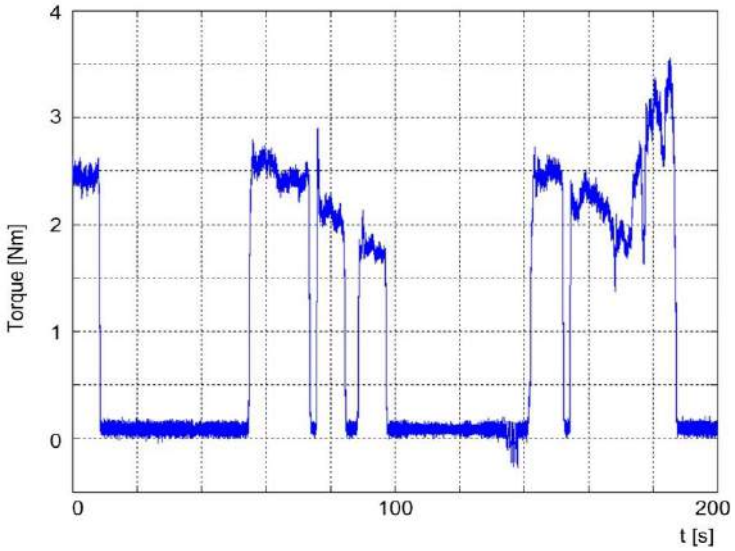

Fig. 2.28 Measured waveforms of starting torque for the tested prototype hybrid piezoelectric motor at the braking/blocking state

2.6.4 NON-CONTACT PIEZOELECTRIC ROTATING MOTORS

There is also a group of non-contact (friction less) piezoelectric rotary motor [**29**]. These motors are characterized by high speed (up 4000 rpm), low weight and long lifetime. In [**75**] a bidirectional non-contact rotary motor using a piezoelectric torsional vibrator and giant electrorheological (GER) has been presented. The driving force of this motor can be actively controlled by varying the electric field strength to the GER fluid. This motor generates 1.04 mNm torque when the electric field of 2 kV/mm with 30% duty cycle is applied to the GER fluid, offering torque at least one order of magnitude larger than those of other types of noncontact piezoelectric motors.

2.7 CONCLUSIONS

Using piezoelectric phenomenon and presently produced piezoelectric materials, various device topologies have been developed for electromechanical energy conversion [**73**], [**69**]. It seems that the most interesting electromechanical topologies are those used to build the ultrasonic traveling wave motor/actuator (Shinsei's motor) and the rotating-mode motor/actuator. Moreover, presently these motors/actuators are widely applied in practice (industry, home appliance, transport, avionics, etc.). The Shinsei's motor due to the generated several traveling waves (dependent upon the used piezoelectric ring) is characterized by a relatively high speed and a small density torque. In turn, the rotating-mode motor, since it generates only single traveling wave, is characterized by a relatively low speed, large density torque, and large blocking torque.

In the next chapter a novel concept of piezoelectric motor has been considered. The concept of this piezoelectric motor is based on using a combined topology of the traveling wave motor/actuator and the rotating-mode motor/actuator. Using this concept it is possible to obtain better drive characteristics that particularly are required for positioning the car/plane seats (chairs).

3 A NOVEL CONCEPT PIEZOELECTRIC MOTOR. INTRODUCTION

In this chapter a novel conception of a piezoelectric motor has been considered. It has been assumed that the new motor is dedicated to adjust the position of car seats (chairs). Presently applied servo drives for car seat adjustment have been briefly described. Next, the known structures of the multi piezoelectric motors have been considered in view of their applications for car seat adjustment. Finally, an introduction to prototyping the novel piezoelectric motor have been presented.

3.1 CAR SEAT POSITIONING SYSTEM

To improve the driver comfort and physical appearance of the car seat, the automotive companies add lots of features. One of these is a front seat with electromechanical positioning system with the following functions: slide, tilt, height, seat, lumbar, and shoulder. Depending upon the number of the seat positioning functions, the electromechanical system has two or more electric motors, e.g. first motor is responsible for raising and lowering of the seat, the second motor is responsible for the movement in forward and backward direction (Fig. 3.1). The use of gears or belts is necessary to obtain an appropriate torque and speed values to position the seat. Moreover, in case of additional options the number of electric motors and the weight of the system will be substantially increased.

Application of the multicell piezoelectric motor will reduce the number of gears due to installing it directly on the movement shaft. It results in better efficiency of the electromechanical structure. The other advantage is that the multicell piezoelectric motor has few times less weight, comparing with electric machine.

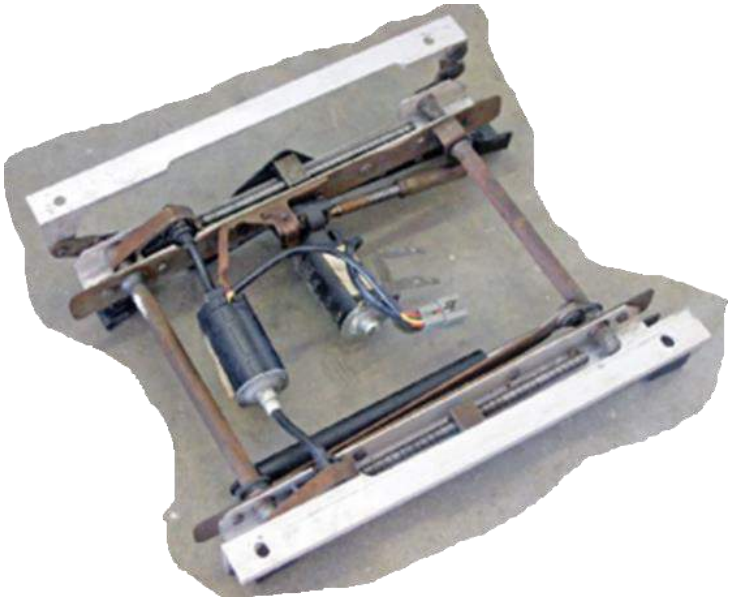

Fig. 3.1 An example of presently applied servo drives for car seat adjustment ***[83]***

3.2 KNOWN STRUCTURES OF MULTI-PIEZOELECTRIC MOTORS

3.2.1 US PATENT OF A MULTI-PIEZOELECTRIC MOTOR

The first structure which should be considered is patented solution of multi piezoelectric motor [**68**]. This piezoelectric motor (Fig. 3.2) has a cylindrical outer motor casing formed by a separable two part housing that encloses and supports three piezoelectric actuators and a group of rotatable components. The rotatable components include: a rotating output shaft that protrudes from the housing (for coupling a load thereto), three drive rollers that engage the output and are evenly spaced thereabout, and an idler ring assembly that secures the drive rollers together with output shaft when the motor is assembled.

The housing has a six piezoelectric stacks (piezoceramics and counter-mass) mounted in a fixed position to interior surfaces of the housing. Each stack is cylindrical with one flat end, having a truncated cone shaped crown roller mounted thereon. The stacks are positioned such that the longitudinal axes of the stacks coincide and the moveable and of each stack ends thereof face each other. A crown roller having a truncated cone shape has its base section fixed to the movable and of each stack so that tapered bearing surfaces on the crown roller rollers can contact the rotating components of the motor when a voltage is applied to the stack. Ball bearing are positioned between the apexes of the truncated cone shaped crown rollers when the motor is assembled. The three piezoelectric actuators are spaced at 120 degree intervals about the center line of the motor. The external bearing surfaces of the drive rollers contact the bearing surfaces of the output shaft so that the rotation of the drive rollers is transferred to the output shaft. The three piezoelectric actuators support and position the rotatable components within the assembled housing during motor operation. The internal surfaces of the drive rollers are positioned over the crown rollers of the actuators so that when the actuators are energized and the crown rollers move in circular or nutating motion, the crown rollers with great force and impart rotation thereto. An idler ring assembly retains the drive rollers in position about the output shaft.

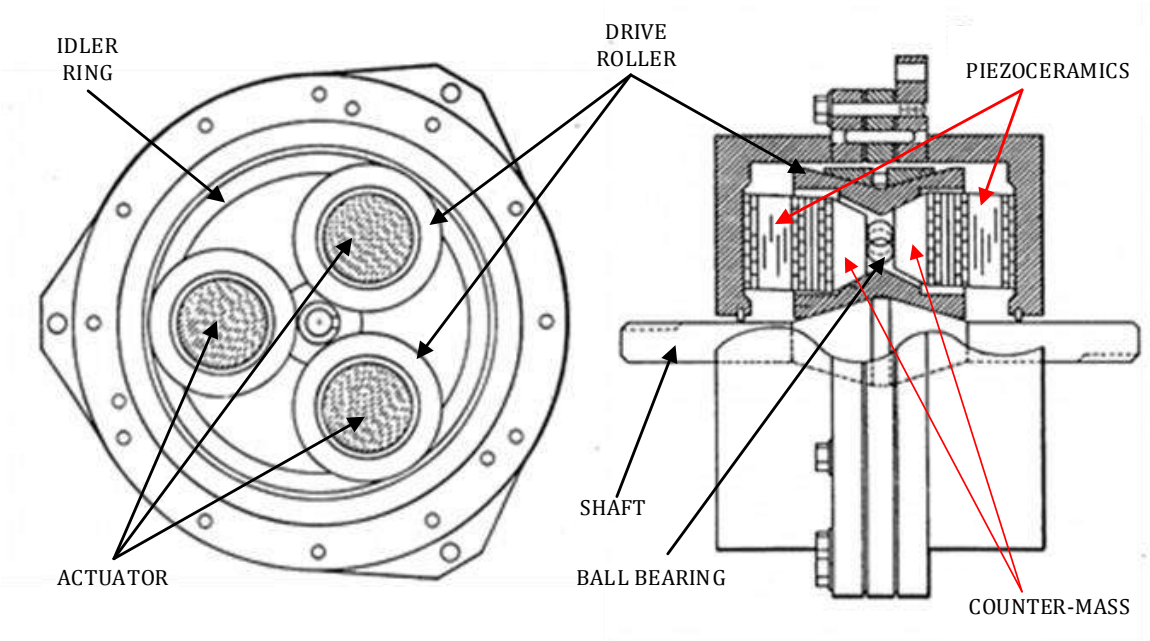

Fig. 3.2 Top view and cross section of assembled multi-piezoelectric motor [**68**]

The actuator shown in Fig. 3.2 have to be supplied by two voltage sources – one voltage has to be 90˚ out of phase with the other.

3.2.2 MULTI-PIEZOELECTRIC MOTOR USING LONGITUDINAL ACTUATORS

The multi-piezoelectric motor using longitudinal actuators has been developed at the laboratory LGEF-INSA in Lyon. The two variants of this prototype motors have been described in [**47**]- [**49**].

The first prototype (Fig. 3.3) had 12 piezoelectric rods covered with a silver electrode, around 10 μm thick, on their flat surfaces and one elastic ring for each half of the structure. The piezoelectric material is a lead-zirconate-titanate PZT ceramic which has a high coupling factor. The motor has symmetrical structure. That enables the use of two rotors coupled on the same motor axis in order to increase the output torque. The PZT rods (diameter 6.35 mm, length 15 mm) are prestressed between two elastic annular plates clamped by a bolt. A frictional layer (polymer) with a high coefficient of friction, bounded on the rotor improves the mechanical contact at the rotor-stator interface [**47**], [**50**].

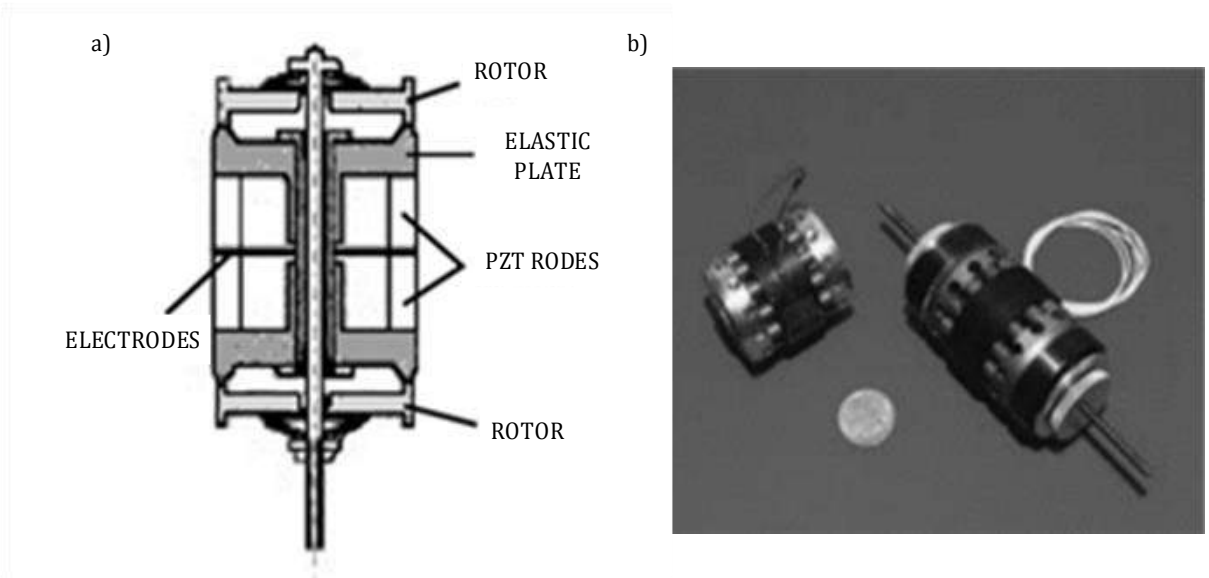

Fig. 3.3 Structure of the multi-piezoelectric motor using longitudinal actuators: (a) cut-off view, (b) motor prototypes [**47**]

The second structure of the motor (MLTWILA) (Fig. 3.4) consist of four multilayer ceramics and actuators (Langevin's type). The total length of the longitudinal actuator is 30 mm and diameter of the stator is 20 mm. The hard PZT ceramics of the longitudinal actuators are integrated (bulk). The structure is preestress by a screws [**49**], [**48**].

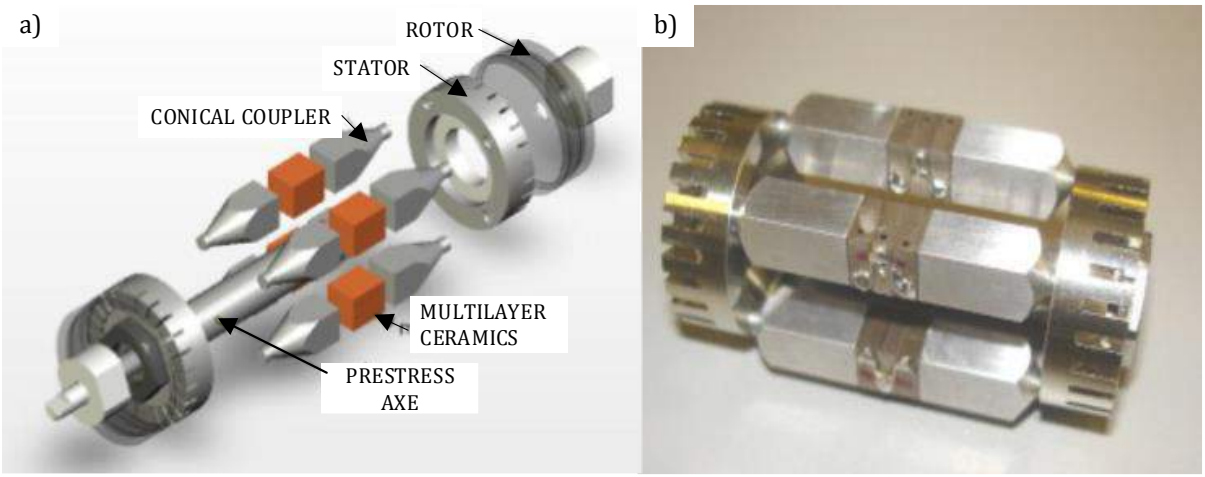

*Fig. 3.4 Complete structure of the multi-piezoelectric MLTWILA: a) exploded view b) assembled prototype [**48**]*

The both motor structures use the propagation of a flexional traveling wave inside a ring-shaped stator. The flexional vibrations of the stator are generated by longitudinal vibrations of the combined piezoelectric actuators that are perpendicularly disposed to the stator and distributed along the circumference.

The measurements results of the first structure are following: maximum torque 0.8 Nm, a no-load rotation speed 120 rpm, and a mechanical output power 4W. The maximal efficiency around is 25%. The second structure has maximum torque 0.095 Nm, a no-load rotation speed 300 rpm and a mechanical output power of 1.5W. Moreover, the efficiency has been improved by reaching 20%.

3.3 A NEW CONCEPT TOPOLOGY OF THE MULTI-PIEZOELECTRIC MOTOR

The concept of the novel piezoelectric motor, referred to as "multicell piezoelectric motor" (MPM), is based on using a combined topology of the traveling wave motor/actuator (known as the Shinsei motor) and the rotating-mode motor/actuator. Each rotating-mode motor topology should be considered as an independent structure – referred as a "single cell". This topology combines the advantages of the both motors (Shinsei motor and rotating-mode motor). Mixing properly the performance of the three rotating-mode actuators three traveling waves are generated.

Using the above mentioned concept it is possible to obtain a better drive characteristics. However, the traveling wave motor does not have a symmetrical structure, but connection between its stator/rotor has many contact points, what makes the motor construction more stable. The rotating-mode motor has a simpler structure for industrial implementation, but its contact conditions are less stable (a single point contacts). Also, the rotating-mode motor has a symmetrical structure. That it makes possible to use two rotors. The combination of these two concepts results in a larger surface contact, and therefore, increases the friction surface.

Finally concluding, the MPM has the following features:

- greater acting force on the rotor, higher speed, and torque,
- higher resonant frequency of the motor cells, which ensures quiet operation even for a large motor,
- prestressed structure which enables its use in a hostile environment,
- symmetrical construction, that allows to use the two rotors. The shaft is driven from two sources, what improves the properties of the motor,
- high holding torque without energy consumption.

The main disadvantage of the considered topology of the MPM is the size of the motor structure. Comparing it to the Shinsei motor, which has compact dimensions, the using mixing structure of the three motors/actuators will cause the increased size of the active motor part.

3.4 PROTOTYPING THE MULTICELL PIEZOELECTRIC MOTOR (MPM). GENERAL REMARKS AND ASSUMPTIONS

In the prototyping process of the MPM some important aspects should be taken into account, for example: active parts - piezoelectric ceramics, counter-mass and rotor material.

The prototype MPM has been determined by the dimensions of the piezoelectric ceramics that have been available at the LAPLACE Laboratory. The available ceramics had the following dimensions:

- external diameter - 12.5 mm,
- internal diameter - 5 mm,
- thickness - 1 mm.

Having determined dimensions of the piezoelectric ceramics, the main goal of this thesis was to design the prototype MPM featuring a maximum possible rotation speed.

The another issue to be considered in designing process of the MPM is the value of the resonance frequency. The MPM should work at the ultrasonic range, i.e., the minimum working frequency should be higher than 20 kHz. While prototyping it should be noticed that measured resonance frequency on the assembled prototype MPM, and the numerically calculated frequency on the virtual model of the MPM can have different values. The expected difference value should be not more than 1 - 2 kHz. Therefore, the simulations should be carried out with relatively high accuracy.

To find the initial (approximate) dimensions of the single actuator (cell), i.e., the length of the counter-mass, the following simple expression:

$$\omega = \frac{2\pi}{L_n}\,(2n-1)\sqrt{\frac{c}{\rho}} \tag{3.1}$$

where:

- $f = \frac{\omega}{2\pi}$ – resonance frequency,
- L_n – the length of the counter-mass,
- n – the wave number,
- c – the elastic modulus,
- ρ – the density of the material.

Assuming an adequate value of the resonance frequency and rearranging eq. (3.1), respectively, the length of the counter-mass can be determined.

To design and study the electromechanical structure of the MPM the Multiphisics Autodesk and Autodesk Inventor with stress module have been used. Autodesk Inventor has been used to define the general shape structure of the single actuator of the MPM and the behavior of the stator topology, while supplying it by voltage source with frequency interval 15 - 50 kHz. In turn, the Autodesk Multiphysics has been used to analyze the piezoelectric phenomena taking place in the studied piezoelectric ceramics.

The whole approach (procedure) to prototyping the novel MPM is described in details in the next chapters.

4 ANALYTICAL MODELLING OF THE PROTOTYPE MPM

In this chapter the analytical modeling of the basic structures of piezoelectric motors have been presented. At first, the modeling of the resonance structure using the Mason's equivalent circuit has been presented. Next, the principles and basic relationships for the Langevin's transducer and rotating-mode motor have been described. Moreover, the stator kinematics of the rotating-mode motor has been presented because there is a difference between the excited mode of the rotating-mode motor and the Langevin's transducer. Finally, using the carried out considerations, the design and analysis results of the novel MPM have been presented.

4.1 MODELING OF THE RESONANCE STRUCTURES. GENERAL REMARKS

Referring to consideration in the previous chapter, the structure of the novel MPM is based on three rotating-mode piezoelectric motors. Since the rotating-mode motor is based on Langevin's transducer, a brief description and analysis of the resonance structures using analytical modeling approach have been presented as shown in Fig. 4.1.

The presented description are referred to analytical approach that has been described in literature [**6**], [**7**], [**18**], [**36**], [**41**], [**77**].

Fig. 4.1 The stages of analytical modeling of the resonance structures

Energy conversions in piezoelectric motor can be divided into two forms:

- elctro-mechnical conversion at the ceramic - provides an elastic deformations in mechanical structure;
- mechano-mechanic conversion between rotor/stator interface - small deformations amplitudes are transformed to the large ones.

The rotating-mode motor principle has been presented in subchapter 2.5.2. Generally, its topology is based on the Langevin's transducer structure. Their structures consist of the piezoelectric ceramics, two metal counter-masses and screw. The screw enables to get more simple structure, because it does not has to be bond. The contact pressure/force between the parts can be controlled by an easy way.

The structures of the Langevin's transducer and the rotating-mode motor work at resonance frequency bandwidth to obtain the maximum displacements at the two ends of the counter-mass. The piezoelectric ceramics in the Langevin's transducer are arranged in a specific direction of polarization to maintain the bending deformations or longitudinal mode. The stack is supplied by single voltage signal. The rotating-mode motor uses two bending modes which are generating traveling wave (Fig. 4.2).

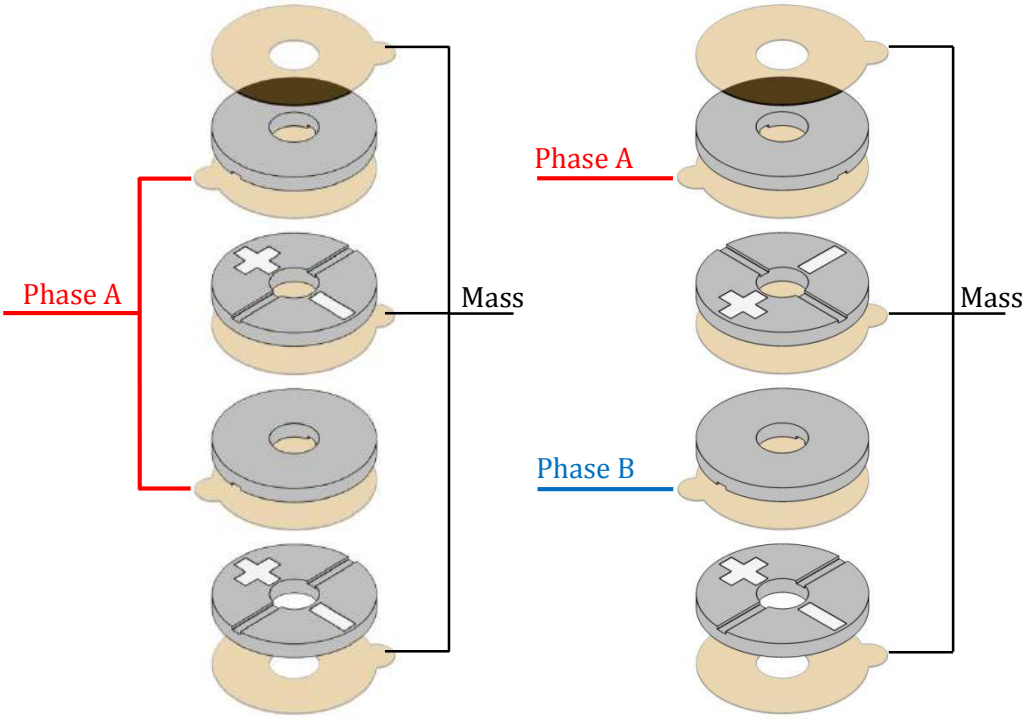

*Fig. 4.2 Orientation of the piezoceramics a) Langevin's transducer, b) rotating-mode motor [**43**]*

4.2 EQUIVALENT CIRCUITS

In Fig. 4.3 an elementary piezoceramic resonance system is presented. It has the following parts: piezoceramic denoted by *C*, counter-mass denoted by *M*, screw spring denoted by *K*, voltage source denoted by *V*, and charge (load) denoted by *F*. Since in the vibration structure the mass of the piezoelectric ceramic is negligible, its kinetic energy can be assumed as negligible [**19**].

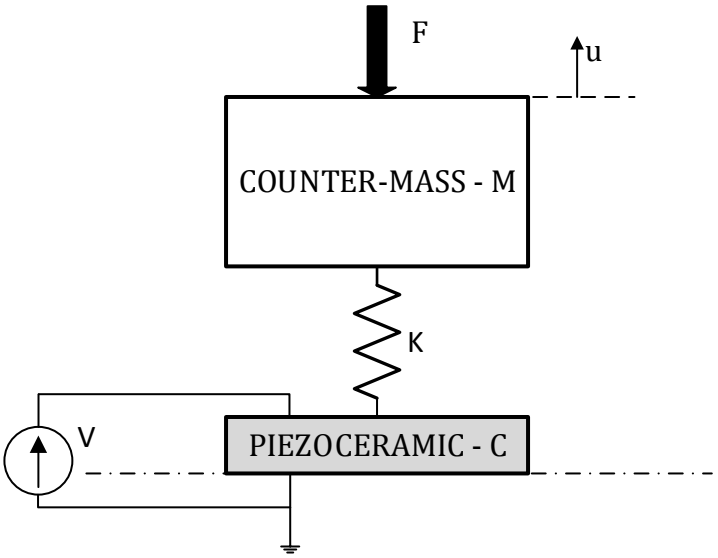

Fig. 4.3 A diagram of an elementary piezoceramic resonance system (transducer)

An electromechanical analog, shown in Fig. 4.4, can be used to model the mechanical part of the considered piezoceramic system (Fig. 4.3).

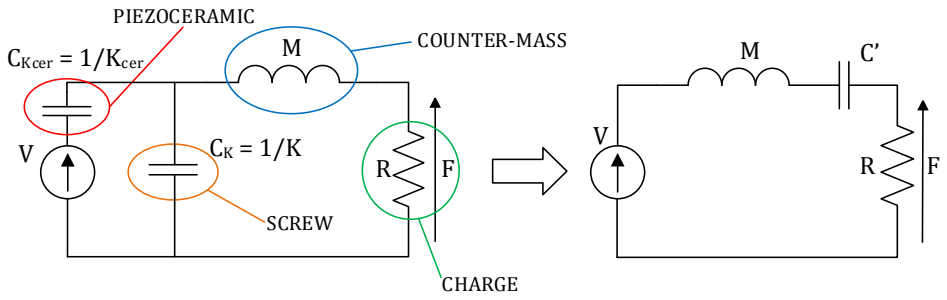

Fig. 4.4 Equivalent circuit of the mechanical part of the system shown in Fig. 4.5

The circuit in the Fig. 4.4 can be transformed to a resonance *RLC* circuit diagram supplied by a voltage source *V*. The capacity and the dieffort factor are expressed as:

$$C' = \frac{C_{Kcer}}{C_K} = C_K + C_{Kcer} \tag{4.1}$$

The completed representation of the transducer (Fig.4.3) in terms of the electrical variables is presented in Fig. 4.6. An electromechanical transformer (with ratio *N*) and the blocking capacity C_0 of the piezoelectric ceramic have been added. The electromechanical transformer is used to combine the electrical and mechanical variables (Tab. 4.1).

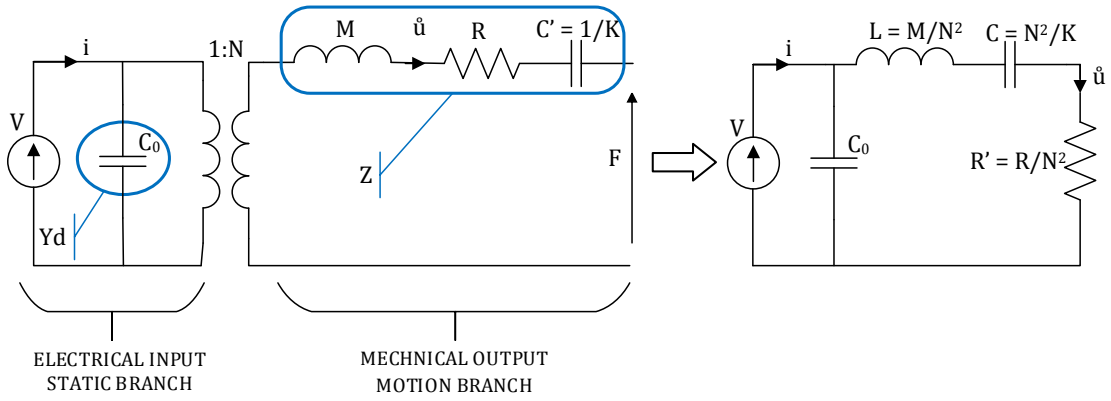

Fig. 4.6 Electromechanical equivalent circuit of the piezoelectric resonance system shown in Fig.4.3: L - equivalent inductance, C - equivalent capacitance, R' - equivalent resistance

The electromechanical equivalent circuit shown in Fig. 4.6 is referred to as the *Mason's equivalent circuit*.

Tab. 4.1 Electromechanical analogies

Mechanical variables	**Electrical variables**
Force (N)	Voltage (V)
Velocity (m/s)	Current (A)
Displacements (m)	Electrical charge (C)
Damping (Ns/m)	Resistance (R)
Mass (kg)	Inductance (H)
Flexibility (m/N)	Capacity (F)

The resonance frequency of the motion branch, which corresponds to the mechanical resonance frequency of the transducer can be expressed as:

$$\omega_0 = \frac{1}{\sqrt{LC}} \tag{4.2}$$

Considering the circuit in Fig. 4.6 and Tab. 4.1 with electromechanical analogies it is possible to write the mechanical equitation in complex notation:

$$\begin{aligned} F &= Z\dot{u} - NV \\ i &= Y_d V + N\dot{u} \end{aligned} \tag{4.3}$$

To obtain the capacity *C* it is necessary to solve some equations. Following the mechanical theory and Hook's Law, where *F = - Kx* and considering the variable *i* equation (4.3), the capacity is:

$$C = \frac{N^2}{K} \tag{4.4}$$

where:

$$F = -K\frac{q}{N}$$

integrating $\dot{q} = N\dot{x}$ you get $q = Nx$

If $u = 0, F = -NV$

And finally:

$$NV = K\frac{q}{N} \quad \Longrightarrow \quad \frac{q}{V} = C = \frac{N^2}{K} \tag{4.5}$$

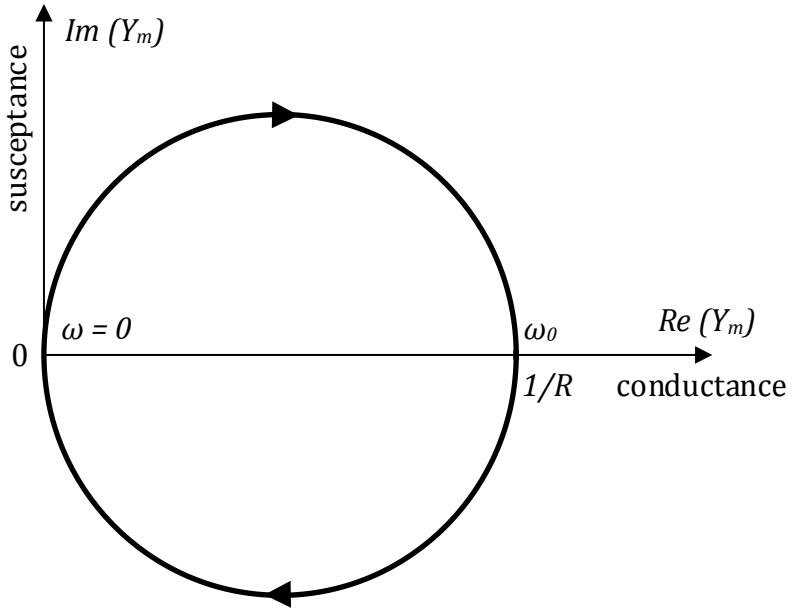

Fig. 4.7 Admittance of the motional branch in terms of the Nyquist graph

The admittance of the motional branch *RLC* in terms of the Nyquist graph (Fig. 4.7) is a circle of radius *½ R* with center point in *(½ R, 0).*

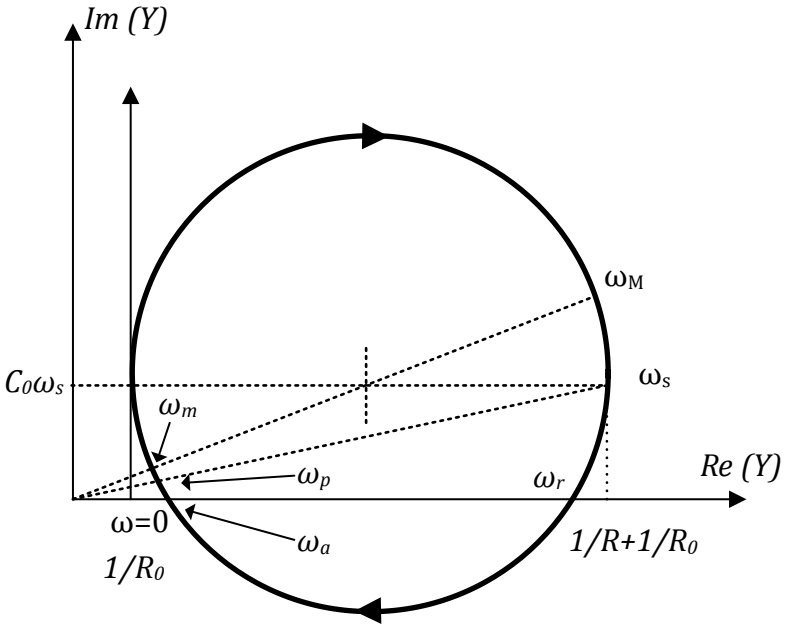

Fig. 4.8 Admittance of the equivalent circuit in terms the Nyquist graph

Adding the static branch C_0R_0 it allows to obtain the Nyquist graph presented in Fig. 4.8 which represents the complete equivalent circuit (Fig. 4.6). Parameter R_0 represents dielectric losses in piezoelectric ceramic. In practice, for piezoelectric motors or actuator, R_0 can be assumed negligible.

The admittance for electric circuit in Fig. 4.6 could be written as:

$$Y = j\omega C_0 + \frac{1}{R + j\omega L + \frac{1}{j\omega C}} \tag{4.6}$$

The admittance Y after transformation:

$$Y = j\omega C_0 + \frac{1 + \frac{C}{C_0} - \omega^2 LC + j\omega RC}{1 - \omega^2 LC + j\omega RC} \tag{4.7}$$

The coefficient of quality Q is high (Q>>10) for the motion branch so the parallel and series resonant frequencies are following:

$$\text{series resonance: } \omega_s = \frac{1}{\sqrt{LC}}$$
$$\text{parallel resonance: } \omega_p = \frac{1}{\sqrt{L\frac{CC_0}{C_0+C}}} \tag{4.8}$$

The other variables determined for the circuit in Fig. 4.8 are:

Maximum admittance: $\omega_M = Max(\|Y\|)$
Minimum admittance: $\omega_m = Min(\|Y\|)$
Resonance: ω_r
Antiresonance: ω_a

Finally, the paramaters *L* and *C* are:

$$C = C_0 \left[\left(\frac{\omega_r}{\omega_s} \right)^2 - 1 \right] \tag{4.9}$$

$$L = \frac{1}{C_0(\omega_r^2 - \omega_u^2)} \tag{4.10}$$

The coupling coefficient was briefly described in chapter 2.4, but it is possible to calculate it by another way. When the mechanical structure is combined with piezoceramics, the coupling coefficient could be calculated from the equivalent circuit (Fig. 4.6). For this case, the k coefficient is the ratio of the energy stored in capacitor *C,* and the total capacity of the resonance structure is *(C + C₀)*

$$k = \sqrt{\frac{C}{C_0 + C}} \tag{4.11}$$

Based on previous calculations the coefficient *k* can be written as:

$$k = \sqrt{1 - \left(\frac{\omega_s}{\omega_r} \right)^2} \tag{4.12}$$

4.3 WAVE PROPAGATION IN LANGEVIN'S TRANSDUCER

In this chapter some characteristic parameters are consider: elastic and kinetic energy which are distributed along the transducer during vibrations [**1**], [**77**].

At the beginning the longitudinal wave in an elastic medium will be described. The Young module should be explained as well. It is defined as the ratio of the stress (force per unit area) along an axis over the strain (ratio of deformation over initial length) along that axis in the range of stress in which Hooke's law holds.

$$\frac{dl}{l} = \frac{1}{E}\,\sigma \tag{4.13}$$

$$F = \sum E \frac{dl}{l} \tag{4.14}$$

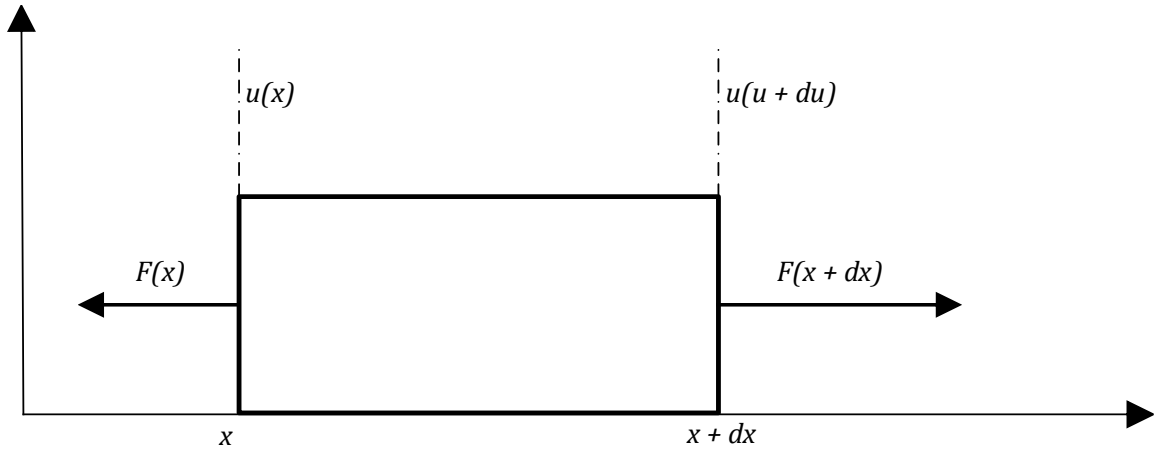

Fig. 4.9 The basic cross-section of the moving beam

This study will be limited to one-dimensional beam with one free ending. A longitudinal wave is a wave where the deformations occurs in the direction of wave propagation. The equation can be obtain by isolating a basic cross-section of a beam.

The dynamic's fundamental principle is applied between *x* and *x+dx*

$$\sum \overrightarrow{F_{ext}} = ma \tag{4.15}$$

where *F* is the net force applied, *m* is the mass of the body, and *a* is the body's acceleration. Thus, the net force applied to a body produces a proportional acceleration. In other words, if a body is accelerating, then there is a force on it.

This equation is:

$$-F(x) + F(x + dx) = m\frac{\partial^2 u}{\partial t^2} \tag{4.16}$$

For $m = \rho dx\varepsilon$ the equation (4.16) is:

$$\frac{dF}{dx}dx = \rho dx \sum \frac{\partial^2 u}{\partial t^2} \qquad \frac{dF}{dx} = \rho \sum \frac{\partial^2 u}{\partial t^2} \tag{4.17}$$

Based on equation *(*4.14) you can determine:

$$E\sum \frac{\partial^2 u}{\partial x^2} = \rho \sum \frac{\partial^2 u}{\partial t} \tag{4.18}$$

$$\frac{\partial^2 u}{\partial x^2} = \frac{\rho}{E}\frac{\partial^2 u}{\partial t} \tag{4.19}$$

Finally:

$$\frac{\partial^2 u}{\partial x^2} = \frac{1}{c^2}\frac{\partial^2 u}{\partial t} \tag{4.20}$$

where:

$$c^2 = \frac{E}{\rho'} \tag{4.21}$$

Assuming that the equation is sinusoidal function of time, the following complex function can be applied:

$$u = Ue^{j\omega t} \tag{4.22}$$

Then the differential equation becomes:

$$U = \alpha e^{-jkt} + \beta e^{jkt} \tag{4.23}$$

where:

$$k^2 = \omega^2 \frac{\rho}{c} \tag{4.24}$$

4.3.1 NON-PIEZOELECTRIC BAR

Another case that should be considered is the non-piezoelectric finite length bar. The waveform here is not unidirectional and reflection of the component could happen. Using the boundary conditions, such as velocity at the ends of the bar *x = 0* and *x = L_n*, and the coefficients *α* and *β*, you will obtain:

$$\begin{aligned} \dot{U_0} &= \dot{U_0}(0) = j\omega(\alpha + \beta) \\ \dot{U_{Ln}} &= \dot{U_0}(L_n) = j\omega(\alpha e^{-jkL} + \beta e^{+jkL}) \end{aligned} \tag{4.25}$$

where, the coefficients:

$$\begin{aligned} \alpha &= \frac{\dot{U_0} e^{jkL} + \dot{U_{L_n}}}{2\omega \sin(nL_n)} \\ \beta &= \frac{\dot{U_0} e^{-jkL} - \dot{U_{L_n}}}{2\omega \sin(nL_n)} \end{aligned} \tag{4.26}$$

Substituting these coefficients in the expression for the internal stress $T = \frac{c\theta u}{\theta x}$ (where c is a material elastic constant), you will obtain:

$$F(x,t) = \Sigma E \frac{je^{j\omega t}}{c\, sin(nL)} \left(\dot{U_0}\, cos\left(n(x - L_n)\right) - \dot{U_{L_n}} cos(nx)\right) \tag{4.27}$$

$$\begin{cases} F_0 = \Sigma E \dfrac{jn}{\omega\, sin(nL_n)} \left(\dot{U_0}\, cos(kL_n) - \dot{U_{Ln}}\right) \\ F_{L_n} = \Sigma E \dfrac{jn}{\omega\, sin(nL_n)} \left(\dot{U_0} - \dot{U_l} cos(nL_n)\right) \end{cases} \tag{4.28}$$

$$\begin{cases} F_0 = F(0) = -jZ_c \left(\dfrac{\dot{U_0}}{tan(kL_n)} - \dfrac{\dot{U_L}}{sin(nL_n)}\right) \\ F_{L_n} = F(L_n) = -jZ_c \left(\dfrac{\dot{U_0}}{sin(nL_n)} - \dfrac{\dot{U_{Ln}}}{tan(nL_n)}\right) \end{cases} \tag{4.29}$$

The Mason model of the non-piezoelectric bar is based on the expression of a common displacement $\dot{U_0} - \dot{U_L}$, so using the *L/2* length is required:

$$\begin{cases} F_0 = Z_c\left(\dfrac{\dot{U}_0 - \dot{U_{L_n}}}{jsin(nL_n)} + j\dot{U}_0 tan(\dfrac{nL_n}{2})\right) \\ F_{L_n} = Z_c\left(\dfrac{\dot{U}_0 - \dot{U_{L_n}}}{jsin(nL_n)} - j\dot{U}_{L_n} tan(\dfrac{nL_n}{2})\right) \end{cases} \tag{4.30}$$

The final equations are shown in Fig. 4.10, and represents the Mason circuit diagram of the non-piezoelectric bar.

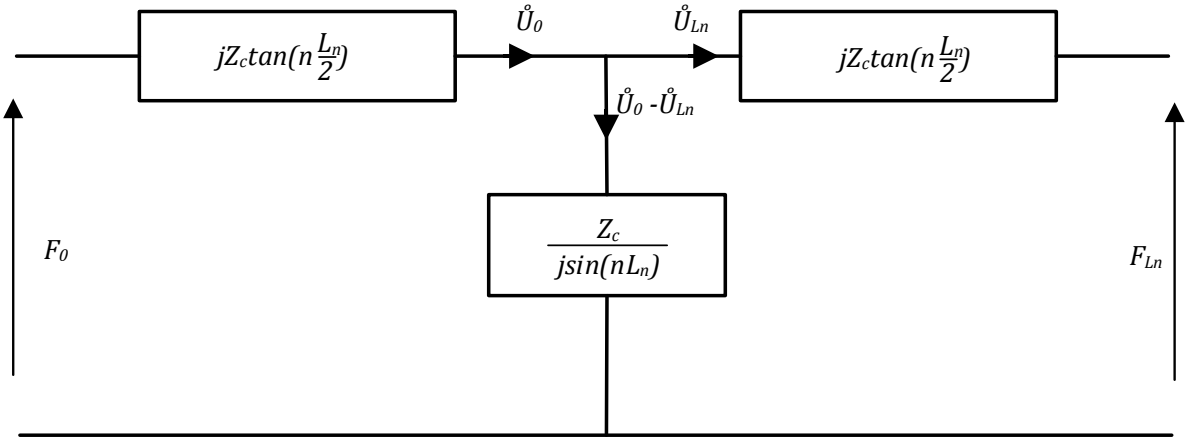

Fig. 4.10 Equivalent circuit of the non-piezoelectric bar: Z_c, L_n and n denote impedance of the elastic bar, wave number, and length of the bar, respectively

The resonance frequency calculations are possible as well. The boundary condition should be specified. For the bar the conditions they are:

- at $x = 0$, a fixed ending, no displacements, so $\dot{U}_0 = 0$,
- at $x = L_n$, a movable ending, no constraints, so $F_{L_n} = 0$.

The corresponding equivalent circuit is obtained by short-circuiting the branch that is corresponding to the section $x=L_n$, and opening the circuit at $x = 0$. For this configuration, the resonance state corresponds to a non-zero vibration velocity which is $\dot{U}_0 \neq 0$, the impedance has zero value, and the conditions are:

$$\frac{Z_c}{jsin(nL_n)} + jZ_c \tan\left(n\frac{L_n}{2}\right) = 0 \tag{4.31}$$

The resonance frequency can be obtained using:

$$\omega = \frac{\pi}{2L_n}(2n-1)\sqrt{\frac{c}{\rho}} \tag{4.32}$$

The described equivalent circuit can be represented by the transfer matrix which represents the deformation velocity and stress ratio:

$$\begin{aligned} F_{L_n} &= F_0 cos(nL_n) - jZ_c\dot{U}_0\, sin(nL_n) \\ \dot{U}_L &= -j\frac{F_0}{Z_c} sin(nL_n) + \dot{U}_0\, cos(nL_n) \end{aligned} \tag{4.33}$$

In matrix form:

$$\begin{pmatrix} F_{L_n} \\ \dot{U}_{L_n} \end{pmatrix} = T \begin{pmatrix} F_0 \\ \dot{U}_0 \end{pmatrix} \tag{4.34}$$

$$\begin{pmatrix} F_{L_n} \\ \dot{U}_{L_n} \end{pmatrix} = \begin{pmatrix} cos(nL_n) & -jZ_c sin(nL_n) \\ -\dfrac{jsin(nL_n)}{Z_c} & cos(nL_n) \end{pmatrix} \begin{pmatrix} F_0 \\ \dot{U}_0 \end{pmatrix} \tag{4.35}$$

This matrix allows modeling the mechanical stack in an easy way, and to determine the resonance frequency of the longitudinal mode. This formula is very simple to express in structure of a Langevin's transducer d_{33} where all elements are connected in series. The resulting matrix is only the result of a simple matrix product.

4.3.2 PIEZOELECTRIC BAR

The equivalent circuit in Fig. 4.10 will be supplemented by piezoelectric ceramics, i.e., represented by a piezoelectric transformer. For this case the piezoelectric equations equations are used that describe the linear nature of piezoelectricity. Dependent on the used input parameters the constitutive equations can be written in different forms. The variations have been described by equations presented in chapter 2: (2.2), (2.3), (2.4), (2.5).

The piezoelectric coefficients are described by the following relationships:

$$\begin{gathered} s^D = s^E - d^t\, \beta^S\, d \\ g = \beta^T d \\ \beta = \frac{1}{\varepsilon} \\ h = \beta^S c\, d \end{gathered} \tag{4.36}$$

The mechanical strain in the piezoceramic material is expressed by S that is added to dielectric displacement D (subchapter 2.3).

These piezoelectric coefficients are used to determine the longitudinal mode of coupling. For this type of deformation, the electric field E and stress deformation T are collinear and could interact (but E on the ceramics surface may not be constant, can be changing). On the other hand, for ceramic without the electrical charges the *divD* is 0, therefore D is constant on the entire length of the ceramic.

Taking into account stress deformation T and using transform you have:

$$T = c^D \cdot S - h \cdot D \longrightarrow T + hD = c^D S \tag{4.37}$$

where:

$$\begin{gathered} c^D = c^E + \frac{e^2}{\varepsilon^S} \\ h = \frac{e}{\varepsilon^S} \end{gathered} \tag{4.38}$$

h - constant between deformation *S* and electric charge *E [V/m or N/C]*

The integration of these local equations (4.30) and (4.37) provides the following expressions relating the mechanical parameters:

at *x = 0* :

$$F_0 + hDA = Z_c\left(\frac{\dot{U}_0 - \dot{U_{L_n}}}{jsin(nL_n)} + j\dot{U}_0 tan(\frac{nL_n}{2})\right) \tag{4.39}$$

at $x = L_n$:

$$F_{L_n} + hDA = Z_c\left(\frac{\dot{U}_0 - \dot{U_{L_n}}}{jsin(nL_n)} + j\dot{U}_{Ln} tan(\frac{nL_n}{2})\right) \tag{4.40}$$

The electrical current flowing through the section *A* is given by:

$$I = j\omega DA \tag{4.41}$$

The voltage *V* across the electrodes (or other metallic material) is the integral of the electrical charge *E* along the length of the ceramic:

$$V = \int_0^L Edx \tag{4.42}$$

Thus (using equation (2.3) $D_i = e_{ikl}\, S_{kl} + \varepsilon_{ij}^S E_k$) you will have:

$$V = \frac{DL_n}{\varepsilon^T} - h\left(U_{L_n} - U_0\right) \tag{4.43}$$

$$V = \frac{L_n}{j\omega\varepsilon^S A} I - \frac{h}{j\omega}\left(\dot{U_{L_n}} - \dot{U}_0\right) \tag{4.44}$$

By substituting equations for blocking capacity (4.45) and after rearranging, you will have:

$$C_0 = \frac{\varepsilon^T A}{L_n} \tag{4.45}$$

$$I = j\omega C_0 V + hC_0\left(\dot{U_{L_n}} - \dot{U}_0\right) \tag{4.46}$$

To determine the variable *F*, eqs. (4.41) and (4.46) should be used:

$$F = hDA$$
$$F = \frac{hI}{j\omega} \tag{4.47}$$

$$F = hC_0 V + \frac{h^2 C_0\left(\dot{U_{Ln}} - \dot{U}_0\right)}{j\omega} \tag{4.48}$$

where the voltage *V* after the rearranging is:

$$V = \frac{F}{hC_0} - \frac{h\left(\dot{U_{L_n}} - \dot{U}_0\right)}{j\omega} \tag{4.49}$$

These equations represent the electric part of the Mason's model. This model can be represented by an equivalent circuit shown in Fig. 4.11 with added electromechanical transformer of ratio hC_0.

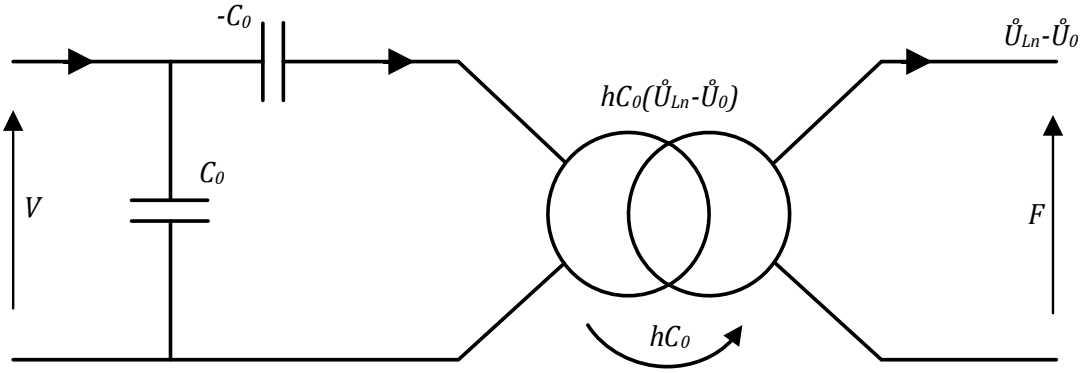

Fig. 4.11 The electrical part of the Mason's model with added electromechanical transformer of ratio hC_0

The piezoceramic can be represented by an overall diagram shown in Fig. 4.12.

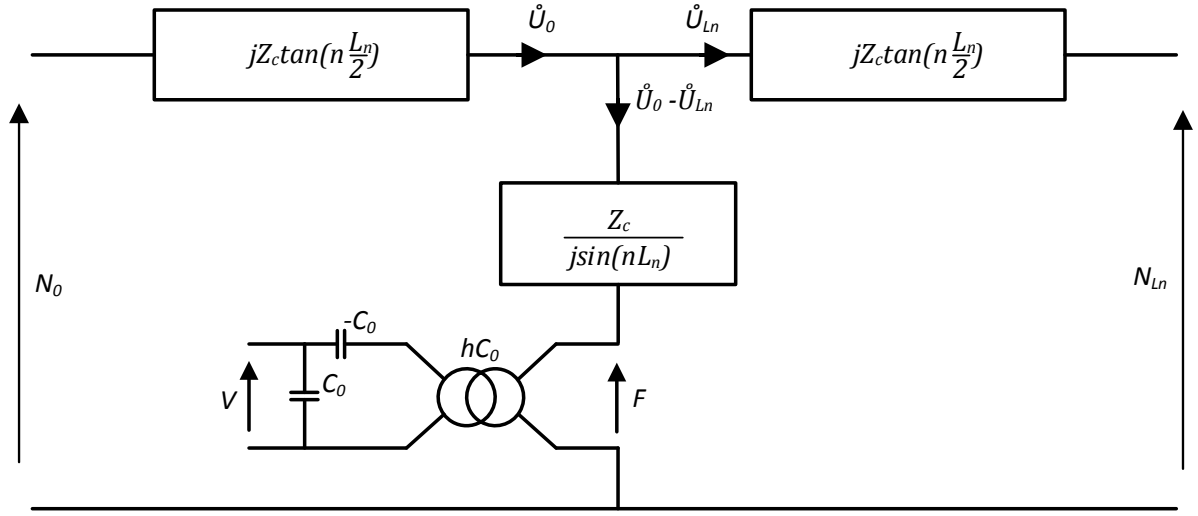

Fig. 4.12 The overall Mason's model - the electrical equivalent circuit of the piezoelectric bar

The Mason's model is helpful for describing the electromechanical coupling effects in the electrical part of the overall Mason's model. This model is interweaving the electric circuit in a more classical mechanical model.

4.3.3 LANGEVIN'S TRANSDUCER

A brief model description of the Langevin's transducer is considered as an introduction to modeling the rotating-mode motor.

The Langevin's transducer has simple structure:

- two counter-masses made of aluminum,
- piezoelectric ceramic, one or more.

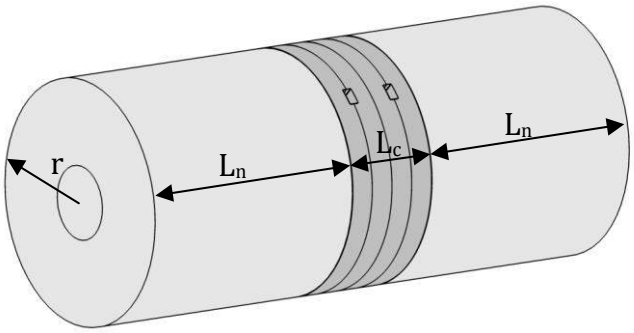

Fig. 4.13 Langevin's transducer structure and geometry

Each element of the Langevin's transducer (Fig. 4.13) may be represented by an overall equivalent circuit diagram (Fig. 4.14). The ends of the transducer are out of charge (load) thus there are no constrains - it is represented by a short circuit on the diagram.

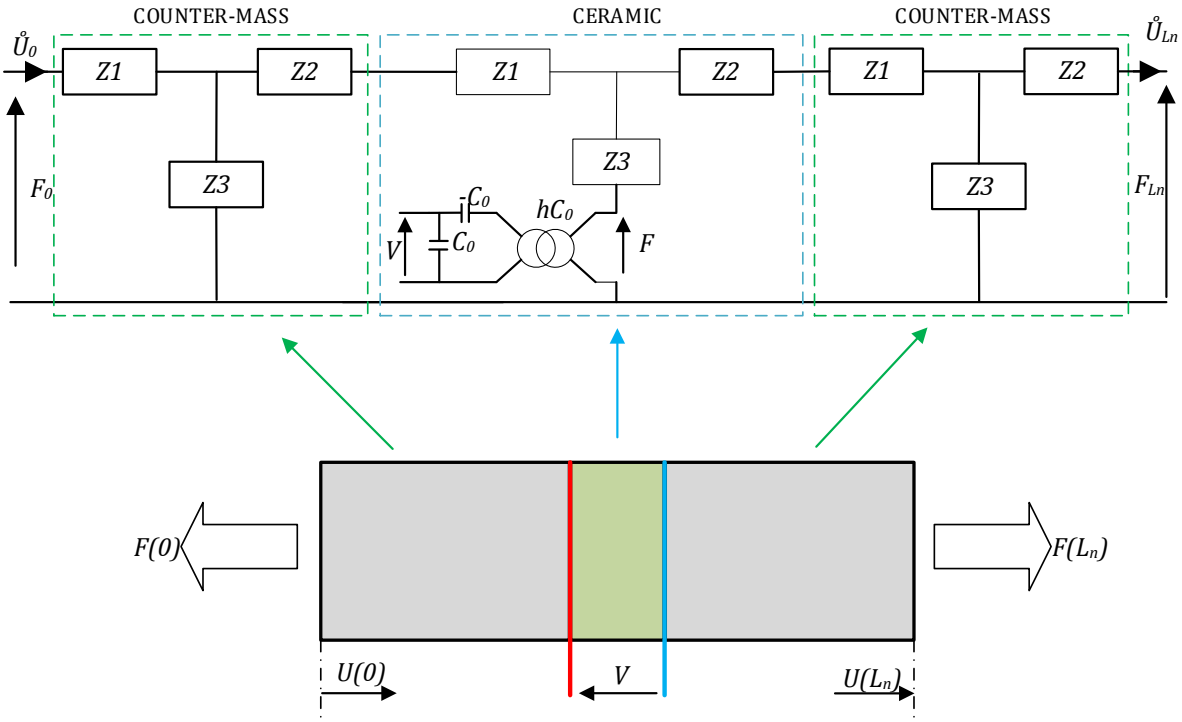

Fig. 4.14 The overall diagram of the Langevin's transducer

In Fig. 4.15 the working principle of the Langevin's transducer has been shown. The ceramics are working in bending mode, i.e., you can see how one side is expanding and shrinking due to the alternating supply voltage *V*.

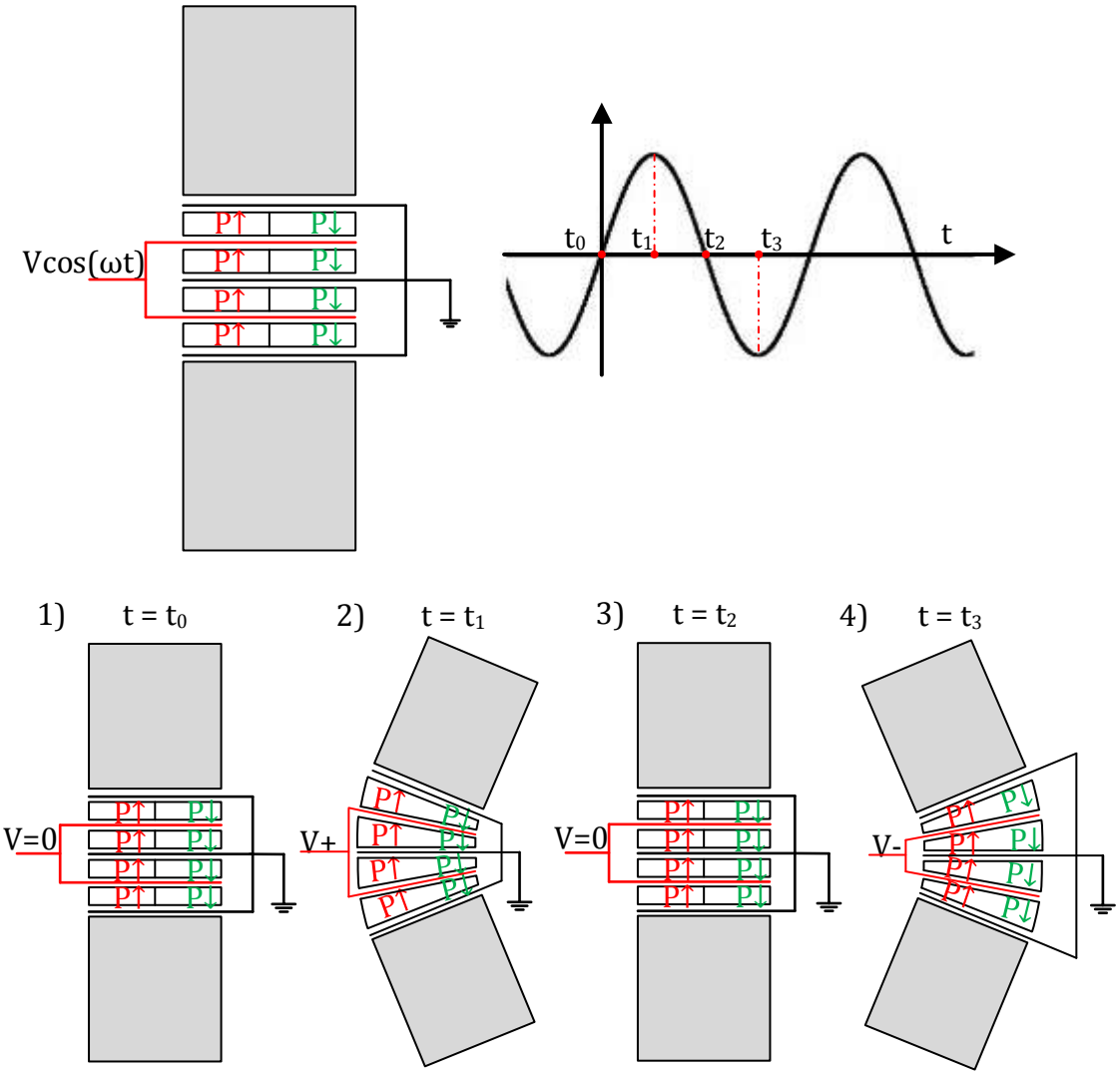

Fig. 4.15 The Langevin's transducer working principle

The considered Langevin's transducer has been studied using the FEM simulations - ANSYS software. The simulation results are only presented for one case of the transducer. To develop its FEM model the following steps have been done:

- in the preprocessor module – definition of the elements, material, geometry and the mesh;
- in the solution module – type of analysis choice, definition of the symmetries, developing the voltage source, definition of the frequency range;
- in the postprocessor module – current calculations which are corresponding to the admittance, reading of the electrical charges.

For the ceramics PC5H the static FEM simulation has been carried out. In the Fig. 4.16 you can see the stress and displacements analysis results. The movement in the *Z* axis can be amplified by using some extra ceramics PC5H. There is also a relatively small displacement/movement in the *Y* axis.

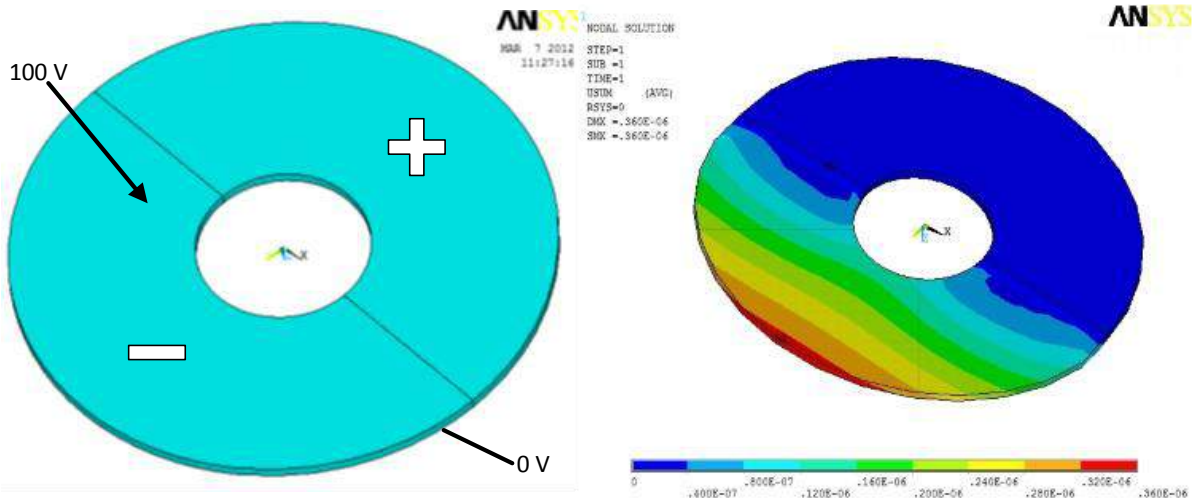

Fig. 4.16 The piezoceramic PC5H - static FEM simulation

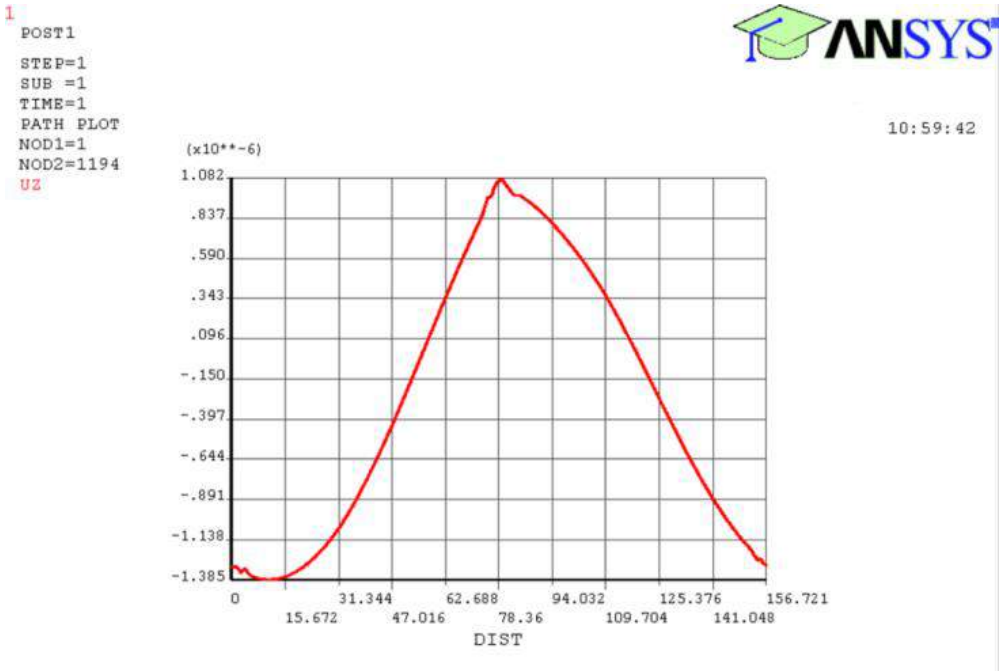

Fig. 4.17 Deformation plots of the piezoceramic PC5H - static FEM simulation

In Fig. 4.17 the deformation have been shown and the amplitude is 2.38 nm. The maximum value corresponds to the centre of the ceramic that is positively polarized, and the minimum corresponds to the centre of the ceramic that is negatively polarized.

The dynamic FEM simulations have been carried out for the counter-mass. The frequency range has been set from 20 kHz to 50 kHz. The resonance frequency value was found by searching the deformations. For this special case study, three resonance modes has been found, at: 28.94 kHz, 28.97 kHz and 40.5 kHz. The result are shown in Fig. 4.18 and Fig. 4.19. You can notice two bending modes and one longitudinal mode.

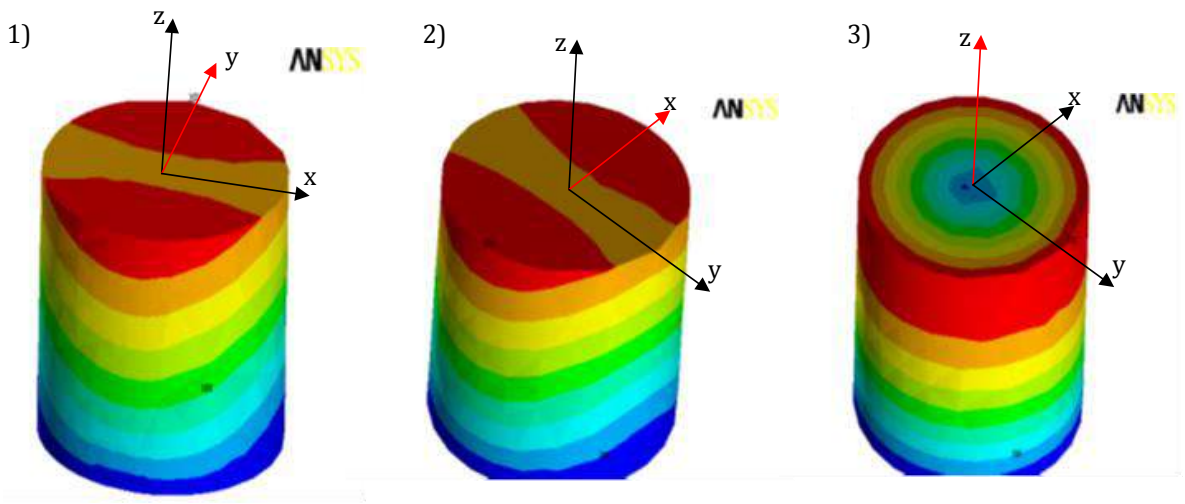

Fig. 4.18 The counter-mass dynamic for the three resonance modes - FEM simulations

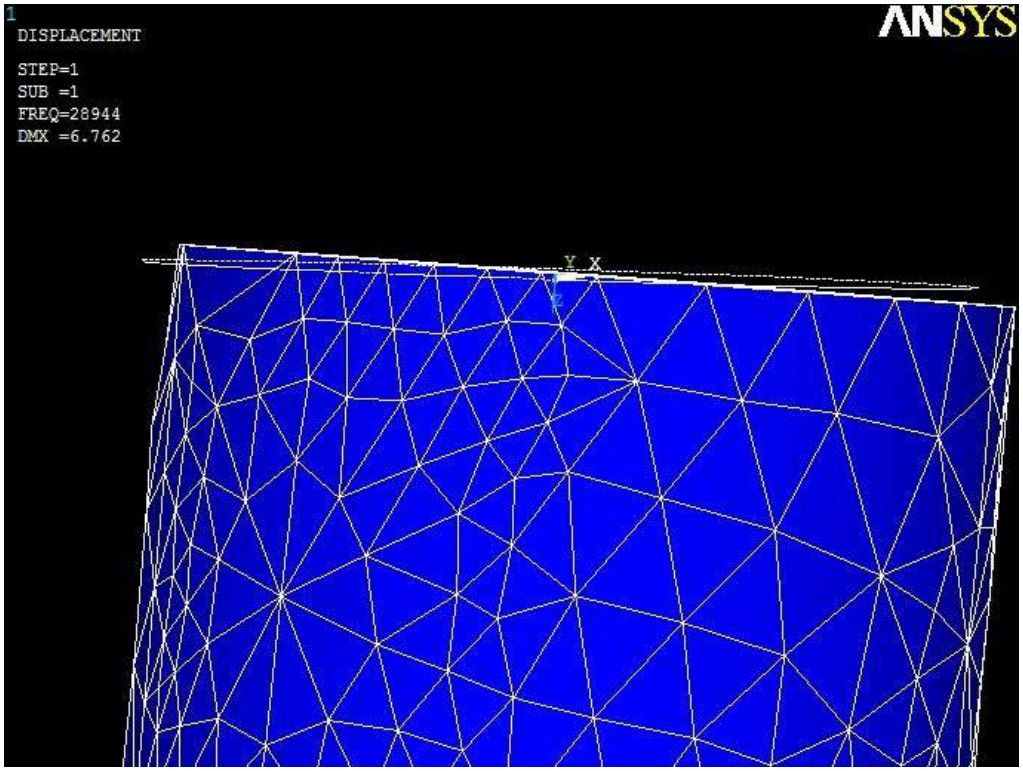

Fig. 4.19 Deformation of the counter-mass at 28.9 kHz frequency - FEM simulation

4.4 ROTATING-MODE MOTOR

4.4.1 EQUIVALENT CIRCUIT FOR METAL-CYLINDER

The analysis of the metal bar flexural vibrations can be used to evaluate the stator dynamic behavior of the rotating-mode motor. For this study the motor model should takes into account the shear deformation and rotational inertia effects, making it suitable for describing the behavior of the short beams, sandwich composite beams or the beams stressed to high-frequency excitation, when the wavelength approaches the thickness of the beam.

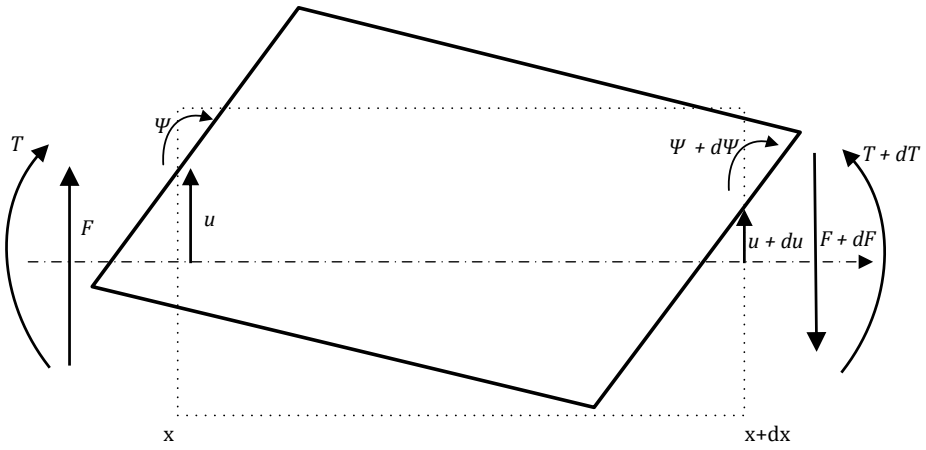

Fig. 4.20 The basic cross-section of the beam at bending mode

The basic motion equation is:

$$EI\frac{\partial^4 u}{\partial z^4}+\rho\frac{\partial^2 u}{\partial t^2}-\ \rho I\left(1+\frac{E}{aG}\right)\frac{\partial^4 u}{\partial z^2\partial t^2}+\frac{\rho^2 I}{aG}\frac{\partial^4 u}{\partial t^4}=0 \tag{4.50}$$

and its solution is:

$$u(x)=Asin(k_1x)+Bcos(k_1x)+Csinh(k_2x)+Dcosh(k_2x) \tag{4.51}$$

It is possible to isolate the two quantities, like moment of inertia I, and a cross sections A (from Fig. 4.20):

$$\begin{aligned}\rho A\frac{\partial^2 u}{\partial t^2}&=\ -\frac{\partial F}{\partial x}\\ \rho I\frac{\partial^2 \psi}{\partial t^2}&=\ \frac{\partial T}{\partial x}-F\end{aligned} \tag{4.52}$$

The additional variables are: u – displacements, T – torque, F – share force, and Ψ – rotational angle.

Using the expression (4.51) it is possible to write next equations for:

torque

$$T(x)=\alpha_M\big(Asin(k_1x)+Bcos(k_1x)\big)+\beta_M(Csinh(k_2x)+Dcosh(k_2x)) \tag{4.53}$$

rotational angle:

$$\Psi(x)=\alpha_\Psi\big(Acos(k_1x)-Bsin(k_1x)\big)+\beta_\Psi(Cch(k_2x)+Dsh(k_2x)) \tag{4.54}$$

and share force:

$$F(x)=\alpha_T\big(Acos(k_1x)-Bsin(k_1x)\big)+\beta_T(Cch(k_2x)+Dsh(k_2x)) \tag{4.55}$$

4.4.2 STATOR KINEMATICS

Based on the literature [**6**], [**36**], [**41**] the traveling wave principle of rotating-mode motor has been explained.

Referring to previous paragraph, to obtain a traveling wave the two electrical supply sources with 90° phase shifted are required, and also the piezoelectric ceramics (phases of the motor) have also to be placed in space orthogonally at each other. Each phase generate the vibrations, which are perpendicular at each other in space (Fig. 4.21). To simplify the analysis it can be assumed that stator has circular form.

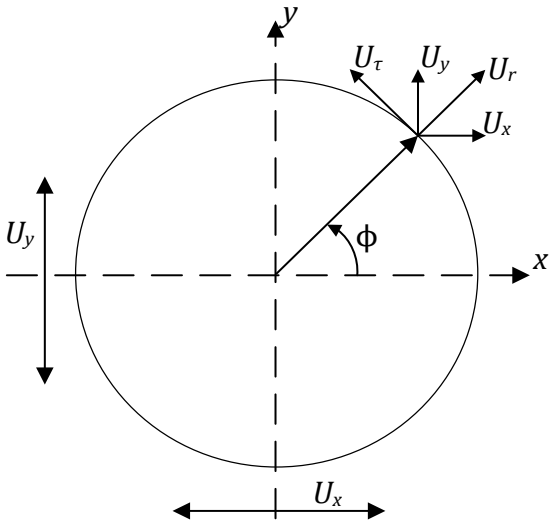

Fig. 4.21. Stator (counter-mass) deflections of the considered Langevin's transducer

The basics bending modes U_x and U_y in two axes are following:

$$\begin{aligned} U_x &= U_0 \cos(\omega t) \\ U_y &= U_0 \sin(\omega t) \end{aligned} \tag{4.56}$$

The superposition of two standing waves can generate traveling wave components. So, it is necessary to consider the deflections in circumferential and radial directions due to circular form of the stator - the values U_τ and U_r are:

$$\begin{aligned} U_\tau &= U_x \cos\varphi + U_y \sin\varphi \\ U_r &= U_y \cos\varphi - U_x \sin\varphi \end{aligned} \tag{4.57}$$

And after transformation, using the (4.56) and trigonometric identities you will have:

$$\begin{aligned} U_\tau &= U_0 \cos\,(\omega t - \varphi) \\ U_r &= U_0 \sin\,(\omega t - \varphi) \end{aligned} \tag{4.58}$$

The longitudinal displacements have also to be considered (Fig. 4.22). These displacements are generating due to the deflections (4.56), where r is a radius of the cross section.

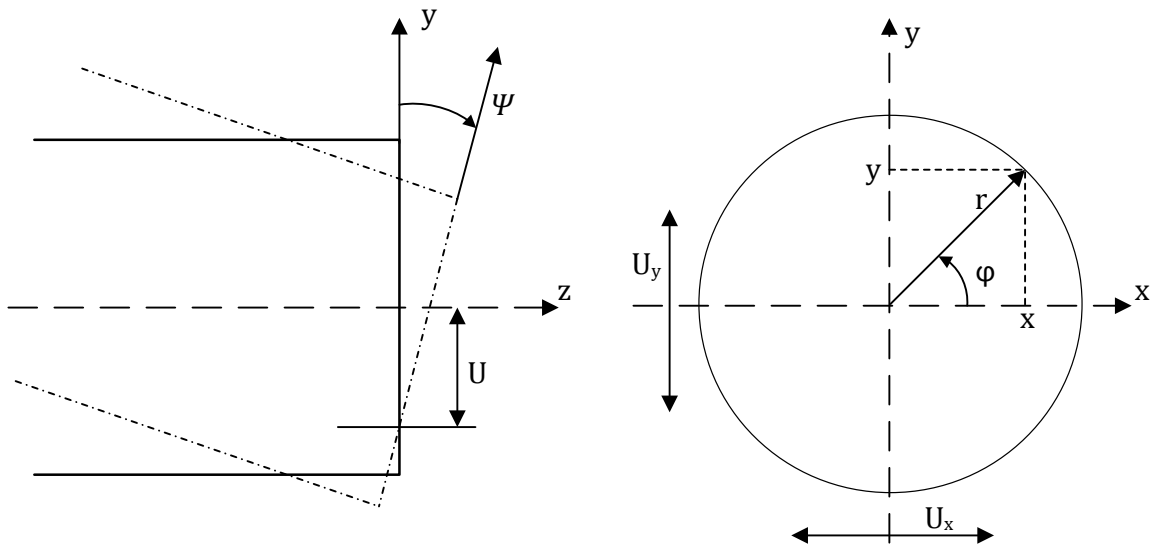

Fig. 4.22 Stator (counter-mass) deformations

Substituting the equations (4.56) to the (4.58), the displacements can be expressed as follows:

$$\begin{aligned} u_x &= -x\frac{\partial U_x}{\partial z} = -xU_0' \cos(\omega t) \\ u_y &= -y\frac{\partial U_y}{\partial z} = -yU_0' \sin(\omega t) \end{aligned} \tag{4.59}$$

Finally, the trigonometric identities in Fig. 4.22:

$$\begin{aligned} u_x &= -r\cos\varphi\ U_0'\ cos\ (\omega t) \\ u_y &= -r\sin\varphi\ U_0'\ sin\ (\omega t) \end{aligned} \tag{4.60}$$

The sum of u_x and u_y using equitations (4.60)

$$\begin{aligned} u &= u_x + u_y = \\ &= -r\cos\varphi\ U_0'\ cos\ (\omega t) - r\sin\varphi\ U_0'\ sin\ (\omega t) = \\ &= -rU_0'\ cos\varphi(\omega t - \varphi) \end{aligned} \tag{4.61}$$

where, u is a traveling wave.

Juxtaposition of the equitation's:

$$u = u_x + u_y = -r\cos\varphi\, U_0' \cos(\omega t) - r\sin\varphi\, U_0' \sin(\omega t) = -rU_0' \cos(\omega t - \varphi)$$

$$\left\{ \begin{array}{c} U_\tau = U_0 \cos\ (\omega t - \varphi) \\ U_r = U_0 \sin\ (\omega t - \varphi) \\ u = -rU_0'\ cos\varphi(\omega t - \varphi) \end{array} \right\} \tag{4.62}$$

The traveling wave is a composition of two elliptical movements – tangential (u and U_τ) and radial (u and U_r). Driving movements is due to tangential movements. Final equitation for "useful" movements is:

$$\left(\frac{U_\tau}{U_0}\right)^2 + \left(\frac{u}{rU_0'}\right)^2 = 1 \tag{4.63}$$

The contact between stator and rotor takes place where u reaches maximum value. The radial movement is a parasite movement; however, it does not have essential influence on the tangential movement.

4.4.3 TORQUE VS. SPEED CHARACTERISTIC

In preceding paragraph the tangential movements has been calculated. Therefore, it is possible to determine the tangential velocity (Fig. 4.23). It can be determined from eq. (4.63):

$$V = U_\tau = U_0\omega\cos\left(\frac{x}{r}\right) \tag{4.64}$$

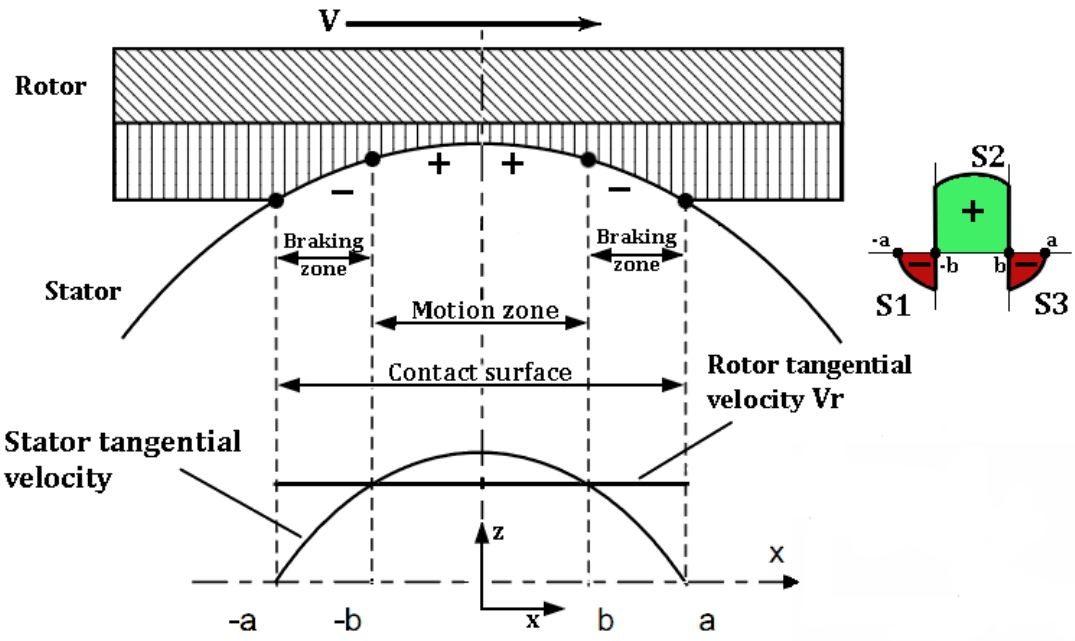

Fig. 4.23 Tangential velocity and friction distribution

Referring to the drawing in Fig. 4.23 the surface between "b" points corresponds the rotor speed V_r. Thus, using the equitation (4.64) and after transforming it, it is possible to calculate this coordination:

$$V_r = U_\tau = U_0\omega\cos\left(\frac{b}{r}\right) \longrightarrow b = Rcos^{-1}\left(\frac{V_r}{U_0\omega}\right) \tag{4.65}$$

The rotor movement directions depend upon the negative or positive V_r values. It is negative when $V<V_r$, and positive when $V>V_r$.

The length of contact is derived from:

$$a = 2\sqrt{\frac{F_{lin}R_{ext}}{\pi e_{el}}} \tag{4.66}$$

where:

$F_{lin} = \frac{Fpres}{c_w}$ – linear load

c_w – width of contact

e_{el} – modulus of equivalent elasticity.

As it was explained above, the rotation speed of the rotor corresponds to the integral of the speed of each point of the contact zone stator/rotor. It should be noticed that all the points of the driving area tend to pull the rotor for a speed greater than the relative speed of the rotor. Opposite, all points in the braking zone tend to slow down the relative velocity for a smaller than the rotor. Considering that there is a point *b* being identical to the rotor relative velocity (4.65). Assuming that the friction coefficient is constant, it can be concluded that the contact surface is divided into three zones – S_2 as a motions area, S_1 and S_3 as a braking area. These surfaces represent the tangential friction, which is really an image of the torque.

The point *d* on the torque vs. speed characteristic (Fig. 4.24) corresponds to rotor speed, when the torque is null, i.e., the sum of the three surfaces is $S_1+S_2+S_3 = 0$. Therefore, there is a balance between the driving force and the braking forces for the no loaded motor.

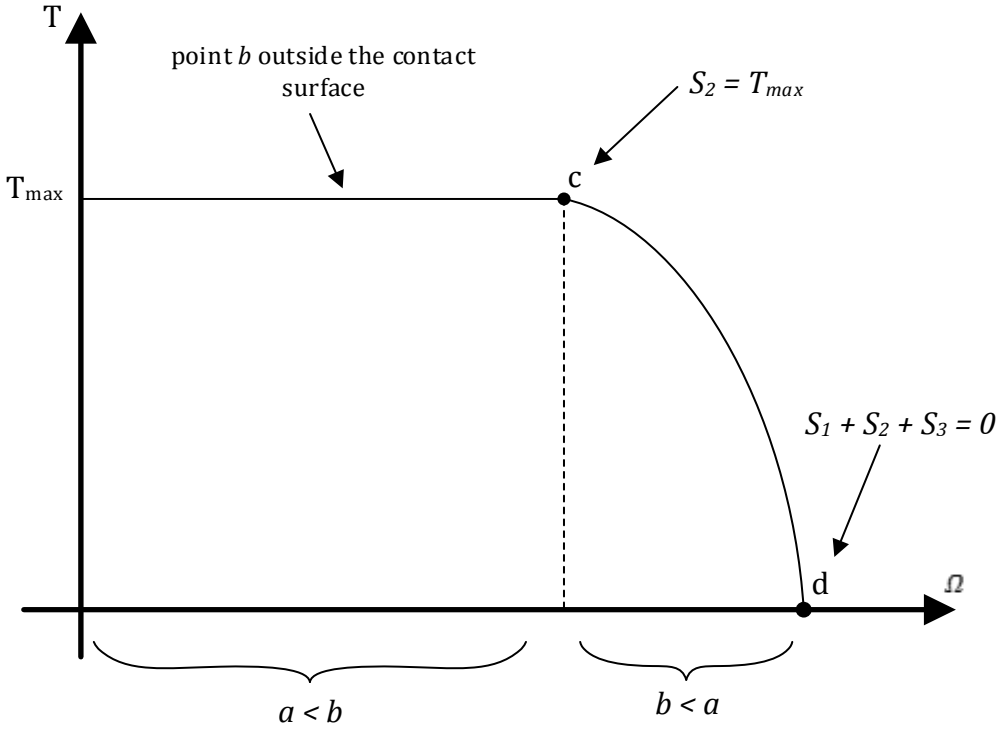

Fig. 4.24 Theoretical torque vs. speed characteristic of a rotating-mode piezoelectric motor

If the motor load is changing, then its speed is decreasing, i.e., the point *b* will move to the zone where the braking points are smaller, until they reach the surface of the contact area (previously called *a*). When *a* = *b* then the torque has its maximum value, since the surface S_2 gets its maximum value. If the motor load is constant then the point *b* will move outside the contact surface, however it has no influence on the torque. Therefore, the torque/speed curve is still linear.

If it assumed that the coefficient of friction is independent of the particular velocity, and using one of the Coulomb barrier description, then the friction force is given by expression $dF = \mu psg(\dot{U_\varphi} - V_r)dS$. Then the theoretical torque value for the case, when $b < a$, can be calculated using the following formula:

$$T = 2\mu r \left(\int_0^b p(x) l_c dx - \int_b^a p(x) l_c dx \right) \tag{4.67}$$

and for the case $b > a$, after transformation eq. (4.68), the maximum torque is given by formula:

$$T_{max} = \frac{\pi}{2} \mu \, a \, l_c \, r \, P_r \tag{4.68}$$

where:

$p = P_r \left(1 - \left(\frac{x}{a}\right)^2 \right)^{\frac{1}{2}}$ - pressure distribution

$P_r = \frac{2F_{lin}}{\pi a}$

μ - friction coefficient,

x - position on the external perimeter of the stator

l_c – contact width.

The formula (4.68) can by written in another way:

$$T_{max} = \mu \, r \, F_N \tag{4.69}$$

where F_N is a pressure force on the rotor.

In some cases the two rotors can be used in the rotating-mode motor. This structure is symmetrical, thus the output torque becomes two times larger:

$$T_{max} = 2 \, \mu \, r \, F_N \tag{4.69}$$

when it is compared to a single rotor structure.

The motor velocity at point $b = a$ can be expressed by formula:

$$\Omega = \frac{U_0 \, \omega \cos\left(\frac{a}{r}\right)}{r} \tag{4.70}$$

4.5 PRELIMINARY DIMENSIONING AND ANALYSIS OF THE PROTOTYPE MPM

Using the considerations that have been carried out in the preceding paragraph, the analytical model of the MPM has been developed [**56**]. This model is taking into account the MPM geometrical dimensions and the used piezoceramics. Since the diameter of the counter-mass is changing along its length, it is necessary to consider that in the analytical model while designing the prototype MPM.

The materials that have been used to design the prototype MPM are following:

- aluminum for the counter-mass,
- PZT 189 for the ceramics,
- steel for the rotor.

The other input parameters, and main geometrical dimensions are listed in Tab. 4.2.

The prototype MPM consists of three actuators, that are based on the rotating-mode motor structure, and one rotor (on one side only) (Fig. 6.2). Thus, the contact surface is not on the entire circumference surface, and it has been considered in the analytical model of the prototype MPM.

Generally, the proposed approach to design the prototype MPM is based on the approach used to design the piezoelectric rotating-mode motor [**6**]. However, due to specific features of the prototype MPM this approach has been modified, respectively [**56**]. It should be pointed out that this approach features some advantages due to the simplicity of the used motor model. Its implementation allows to model each MPM element separately, and also reduce the minimum number of the kinematic variables. However, for studying some cases of a more complex motor structure using a greater number of the motor equivalent schemes will be required. For the final MPM design stage its parameters (geometry dimensions) can be determined using a simple analytical motor model, or on the other hand - using the FEM approach as well.

The developed analytical model of the prototype MPM has been implemented in the MATLAB software. The program code is given in the Appendix 1.

The calculation results of the prototype MPM have been presented in Fig. 4.25 - Fig. 4.28.

The overall mechanical losses of the motor are sum of the losses in the vibrating stator and the losses due to the stator-rotor contact. The stator mechanical dissipation losses are comparable to the power generated at the contact points with the radial displacement amplitudes. Reducing of these mechanical losses will increase the rotational speed or torque of the motor for the same power supply voltage.

To obtain an overall performance of the prototype MPM, it is necessary to take into account the proper value stator/rotor contact surface. For the analytical calculations it has been assumed that the amplitude of the radial displacements is equal to 0.67 μm, and the supply voltage value is about 200 V.

Finally, the maximum total torque of the MPM has been calculated using the following approximation: the torque value computed for the single actuator has been multiplied by three, i.e., by the number of used driving actuators (rotating-mode motors). The result for the maximum total torque is about 0.6 Nm. The torque/speed curve of the MPM is shown in Fig. 4.27. The maximum torque of the prototype MPM is changing due to the applied force to the rotor.

The calculated efficiency is quite high, however some factors have not been included, e.g., mechanical losses, rotor/stator nonlinearity contact, and rotor vibrations due to the used “Smalley” springs. The mechanical losses (results of friction) are converted into heat, and thus the efficiency of the prototype MPM does not exceed 20%.

Tab. 4.2 The main input data for the prototype MPM: geometrical dimensions and parameters

Parameter	Value
External radius of the ceramic r_e	12.5 mm
External radius of the actuator r	12.5 mm
External radius of the contact surface r_{er}	26 mm
Quality factor	25
Pressure force F_N	125 N
Friction coefficient μ	0.29
Percentage contact area/surface	25%
Young's modulus of the stator	69 GPa
Young's modulus of the rotor	210 GPa
Poisson's ratio of the stator	0.34
Poisson's ratio of the rotor	0.3

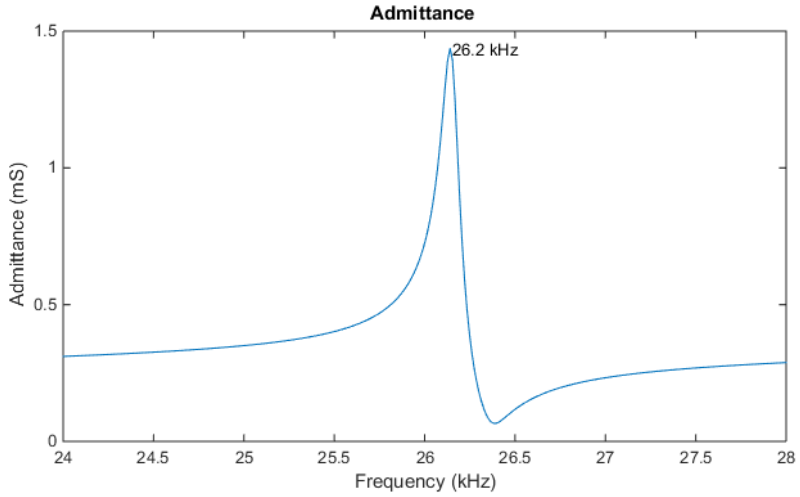

Fig. 4.25 Calculation results of the resonance frequency

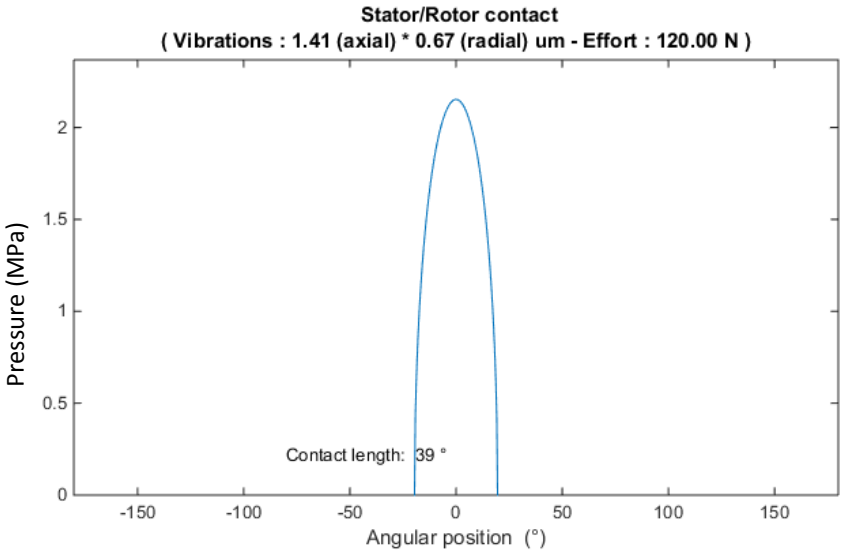

Fig. 4.26 Stator/rotor contact characteristic

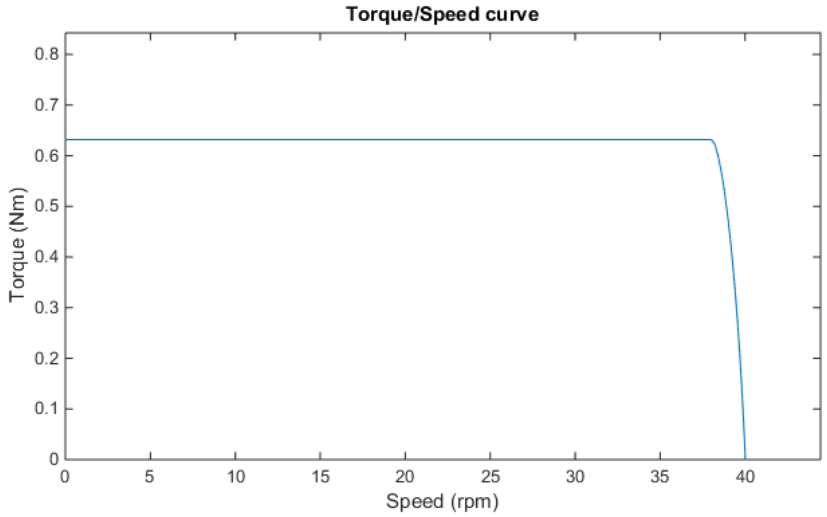

Fig. 4.27 Torque vs. speed characteristic

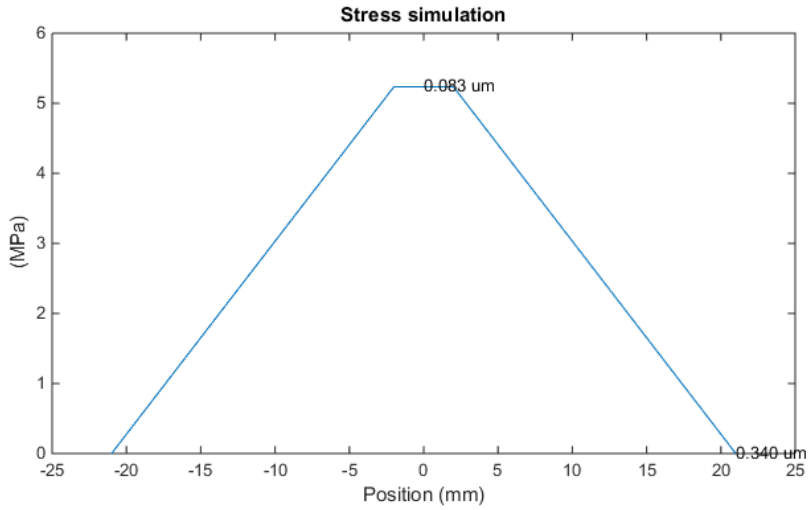

Fig. 4.28 Calculation results of the stress

To analyze the influence of the friction coefficients and pressure force values on the torque vs. speed characteristic of the prototype MPM some calculations have been carried out. The calculation results are shown in Fig. 4.29 and Fig. 4.30, and as a 3D plot in Fig. 4.30. For the analysis it has been assumed: friction coefficient μ = 0.29 for a metal-metal contact, whereas μ = 0.25 and μ = 0.21, respectively, for a lubrication system (oil).

As it has been expected that changing the friction coefficient or pressure force has an influence on changing the torque. Increasing the pressure force results in a better rotor/stator contact, and thus the torque has higher values.

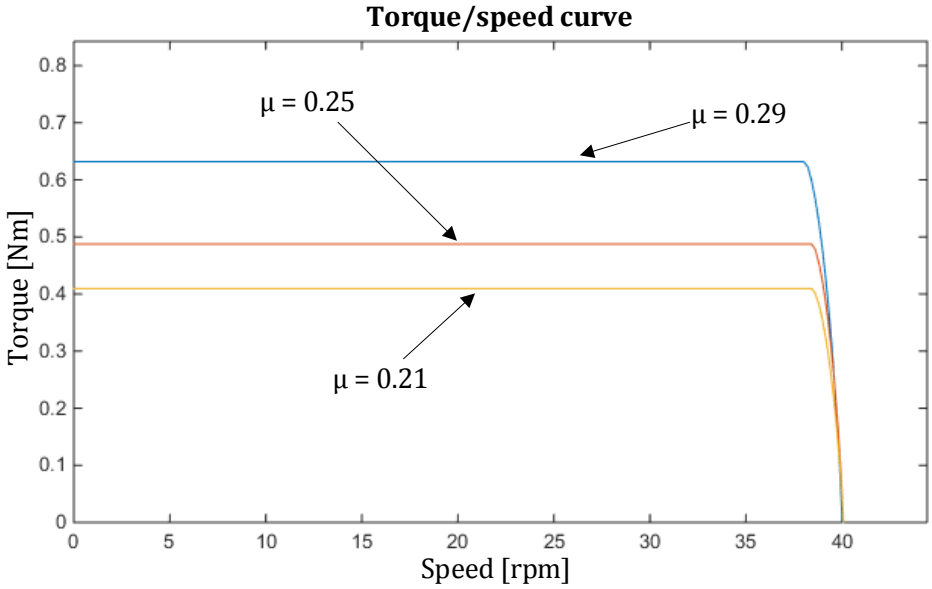

Fig. 4.29 Torque vs. speed characteristics for different values of the friction coefficients and the same value of the pressure force (F_n =120 N): blue curve - μ = 0.29, red curve - μ = 0.25 and yellow curve - μ = 0.21

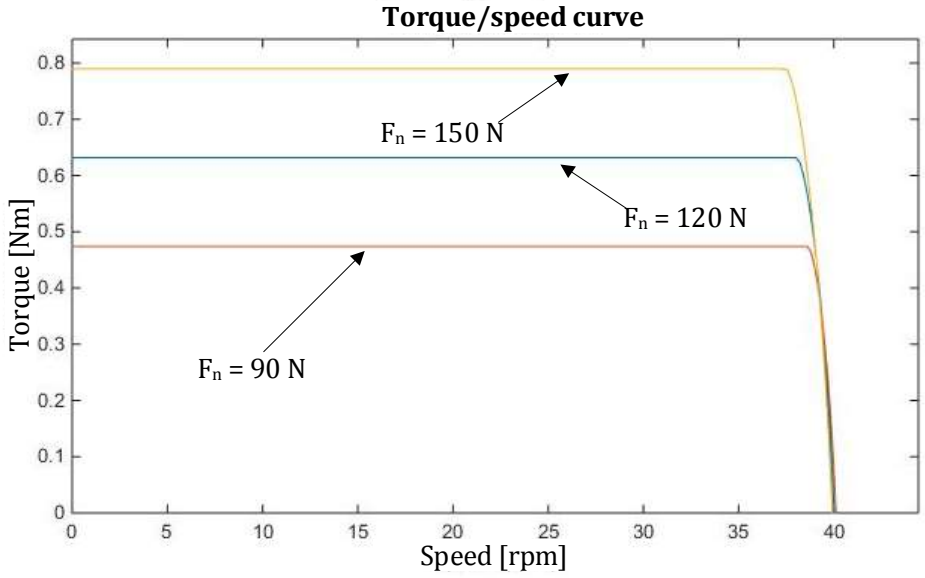

Fig. 4.30 Torque vs. speed characteristics for different values of the pressure force and the same friction coefficient (μ = 0.29): blue curve - F_n =120 N, red curve - F_n =90 N and yellow curve - F_n =150 N

In turn, in Fig. 4.30 is shown the torque vs. speed characteristic in terms of the stator/rotor contact surface. With higher contact surface the characteristic becomes more "smooth", however the efficiency of the motor becomes lower due to the heat generated by friction.

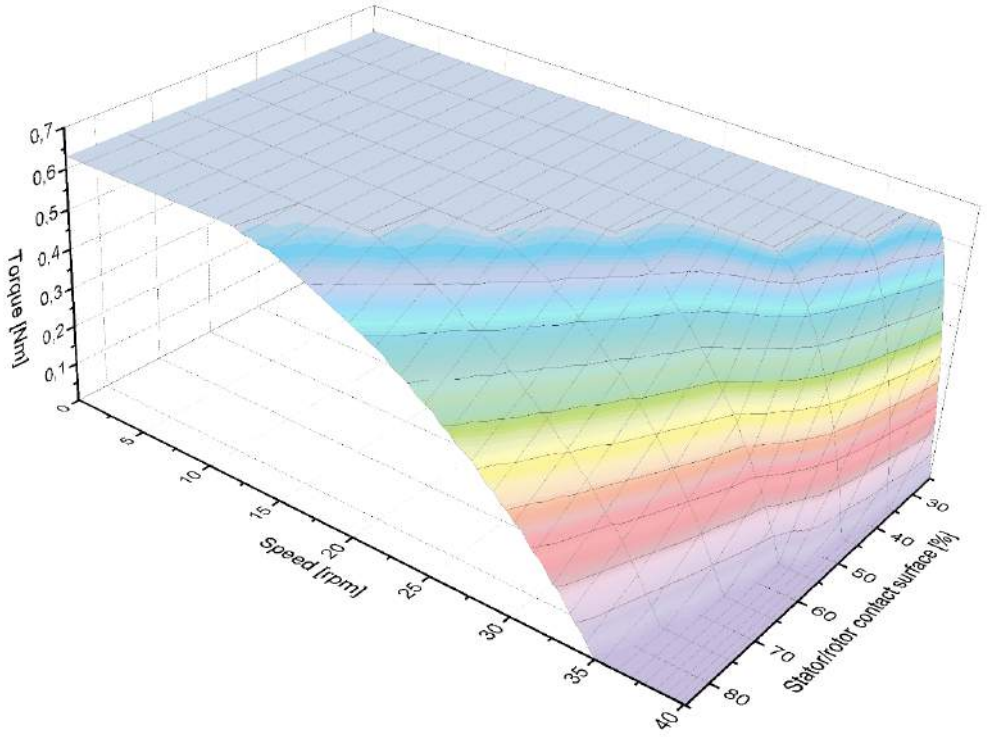

Fig. 4.31 Torque vs. speed 3D plot characteristics in terms of the stator/rotor contact surface

For comparison the torque vs. speed characteristic of the rotating-mode motor considered in [**6**] have been calculated (Fig. 4.32). For pressure force $F_n = 55$ N the results are following: the blocking torque - 0.15 Nm, and maximum speed - 67 rpm.

In turn in Fig. 4.32 are shown the torque vs. speed characteristics of the rotating-mode motor considered in [**6**] for different values of the pressure force.

From the comparison analysis it can be pointed out that values of the blocking torque for the rotating-mode motor considered in [**6**] are almost two times lower than for the prototype MPM.

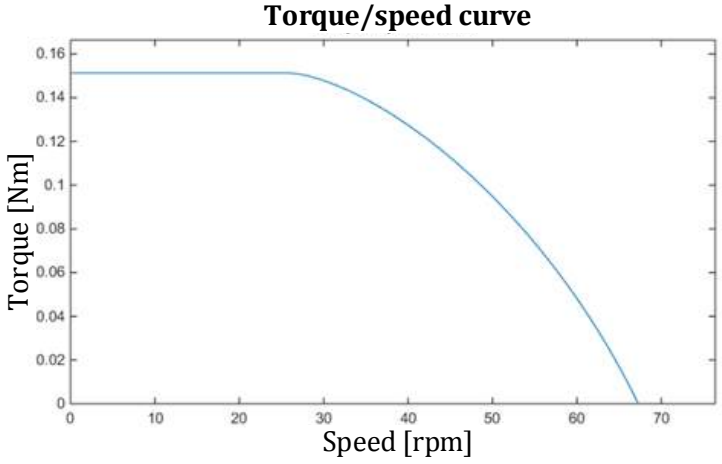

*Fig. 4.32 Torque vs. speed characteristic of the rotating-mode motor considered in [**6**]*

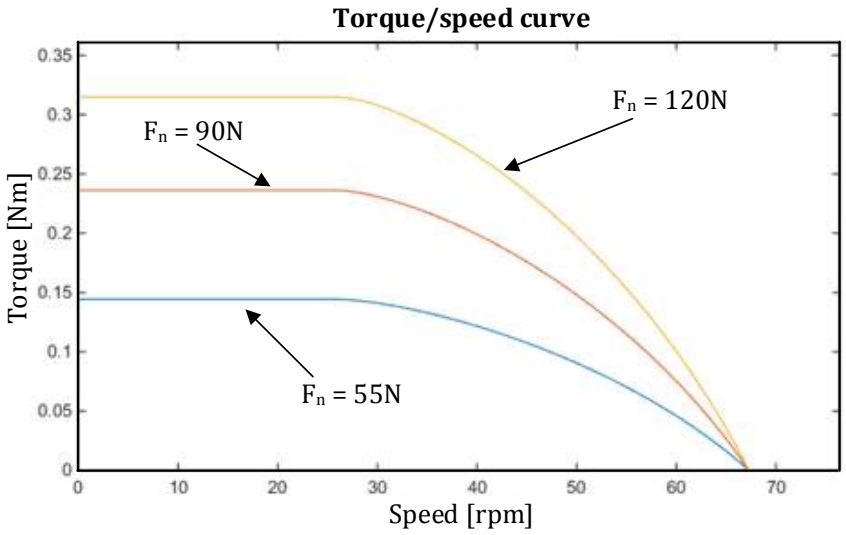

*Fig. 4.33 Torque vs. speed characteristics of the rotating-mode motor considered in [**6**] for different values of the pressure force*

The prototype MPM structures consists of three resonance actuators (rotating-mode motors) and one rotor (only on one side). Due to its specific stator geometry, its rotor/stator contact is only 25% of the overall circumference of the rotor, thus torque vs. speed characteristic is more "sharp". In turn, for the rotating-mode motor (considered in [**6**]) the rotor/stator contact is on the entire surface of the rotor circumference, and thus its torque vs. speed characteristic is more smoothed, while compared with prototype MPM.

For the both motors the measured torque vs. speed characteristics will be compared in subchapter 6.5.

4.6 CONCLUSIONS

Referring to the Langevin's transducer equivalent circuit the analytical model for the prototype MPM has been developed, and implemented in the Matlab software. The developed model has been based on a modified analytical model of the rotating-mode motor considered [**6**].

The preliminary dimensions and parameters of the prototype MPM have been determined using its developed analytical model.

At the next design stage of the prototype MPM its preliminary determined dimensions and parameters will be verified using its virtual (geometrical) model, and numerical methods (FEM) [**57**] and [**58**]. This is the scope of the following chapter.

5 SIMULATIONS OF THE PROTOTYPE MPM

In this chapter the prototyping process of the MPM has been carried using its virtual (geometrical) model and numerical methods [**57**], [**58**]. In the Fig. 5.1 a flowchart of the prototyping process have been presented.

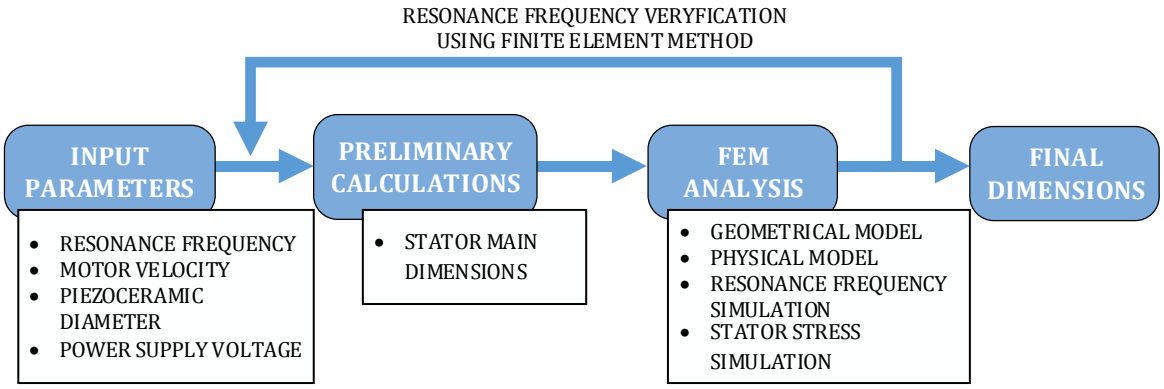

Fig. 5.1 The MPM virtual prototyping flowchart

To design the final structure the simulations using the finite element method (FEM) have been carried out. For this purpose the two types of Autodesk software **[84]** have been used. The Autodesk Inventor has been used for modal analysis to determine the resonance frequencies of the counter-mass, and the Autodesk Multiphisics for:

- static simulation of the electrostatic module to study the deformation of the piezoceramic,
- static stress simulation to verify the MPM virtual model in terms of material strength.

5.1 FINITE ELEMENT METHOD

The FEM is used for finding approximate solutions of boundary value problems for differential equations. It uses variety of methods to minimize an error function and produce a stable solution. Analogous to the idea that connecting many tiny straight lines (mesh) can approximate a larger circle, FEM encompasses all the methods for connecting many simple element equations over many small subdomains, named finite elements, to approximate a more complex equation over a larger domain. Using the finite element method, it is possible to represent the dynamic behavior of physical system. In practice, this allows to calculate numerically the characteristics of very complex objects with differential equation.

The general flowchart presenting the various stages of the FEM simulation has been shown in Fig. 5.2. The most important part in the simulation is preprocessor where the model geometry, boundary conditions, properties of the materials and mesh density are defining. Depends of parameters variety the postprocessor will calculate more or less accurate results [**52**].

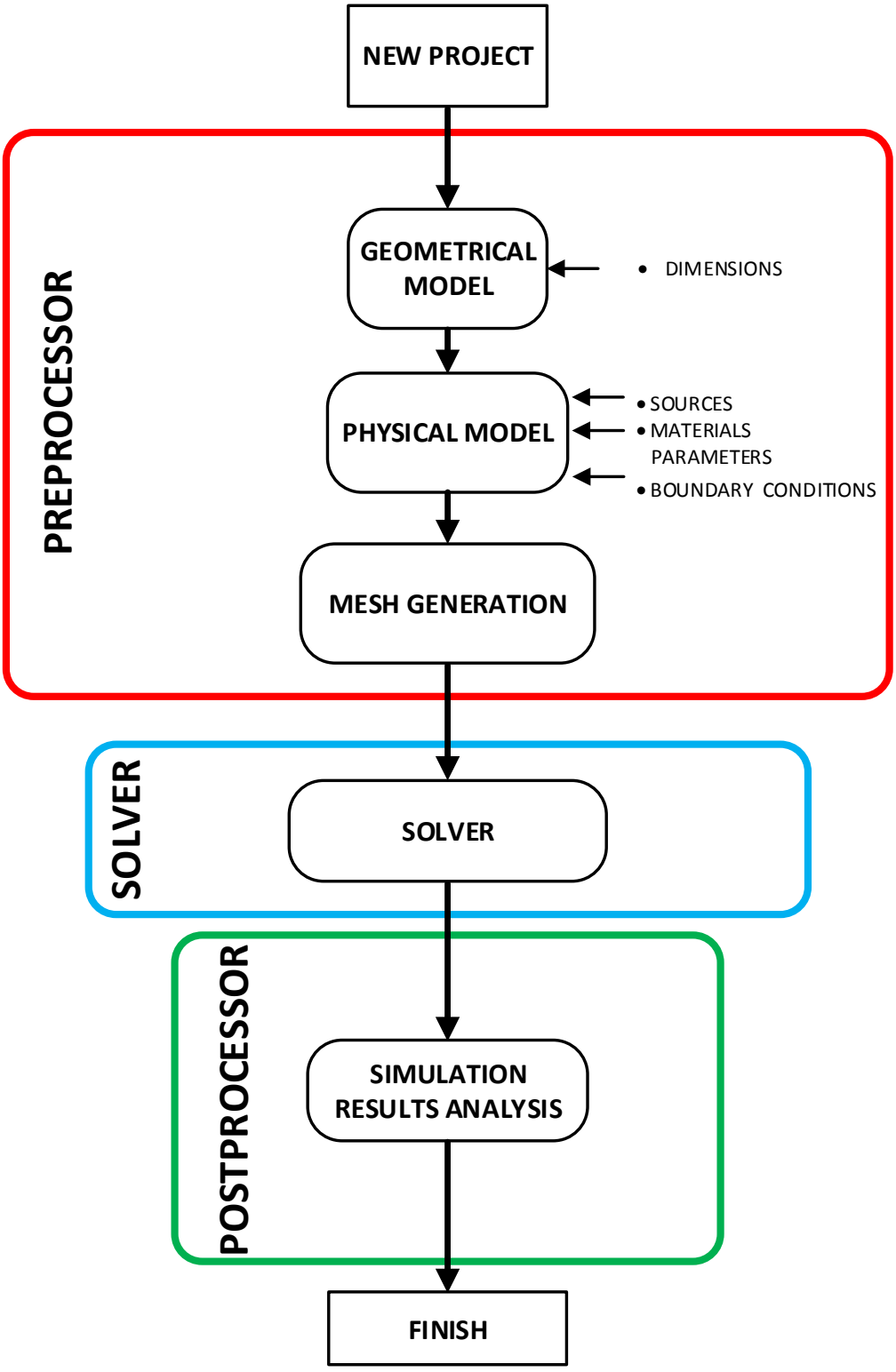

Fig. 5.2 Finite Element method flowchart

5.2 PIEZOCERAMIC STRUCTURE

The first step for motor's FEM analysis is the simulation of the piezoceramic ring to determine the deformation directions. As it was motioned above, to simulate the deformation of the ceramic the Multiphisics has been used. Firstly, the static simulation with electrical/thermal module has been prepared.

Initially the MPM geometry has been defined. The two half rings have been created and connected by "contact elements" option. The ceramic dimensions are following: external diameter 12.5 mm, internal diameter 5 mm and thickness 1 mm. To complete the geometry it was necessary to lock the degrees of freedom in contact surfaces.

Next, it is crucial to define the material – PZT 189. The material characteristics is defined by using three matrices: [*e*] to the piezoelectric constant effect, [*c*] for stiffness and density of the piezoceramic. To simulate the stress-charge condition, the two types of material has been defined. To simulate the positive and negative polarization, the piezoelectric coefficient e_{33} have positive or negative value. The materials have been assigned to the each volume.

The electrical voltage has been assigned – 100V on the top and 0V on the bottom of the ceramic. In physical model the voltage is applied by electrodes but in FEM model this solution has been made by surface with electrical charge. If the generated electric field is in the same direction as the positive polarization, the sector expands. In contrast, for a negative polarization, the sector shrinks.

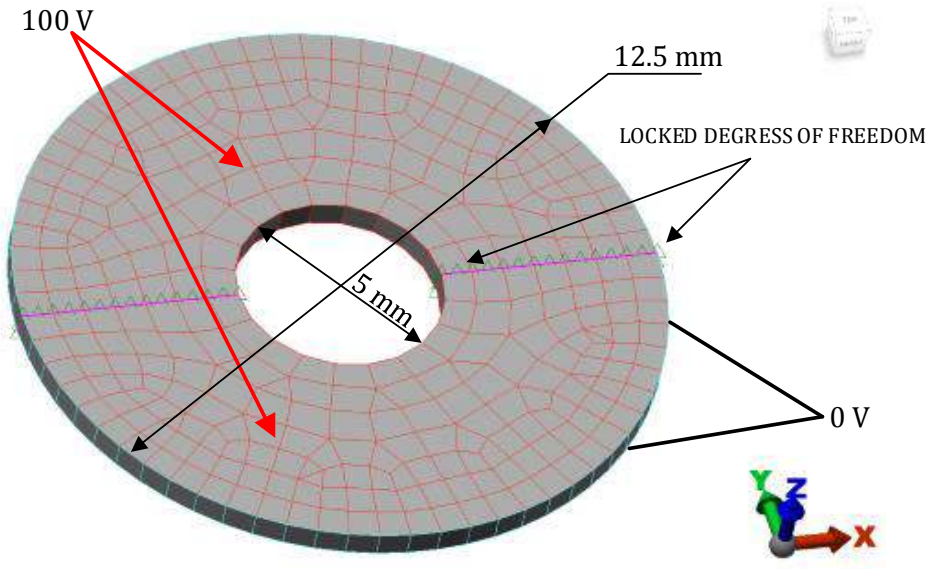

Fig. 5.3 Piezoceramic geometry and dimensions used in FEM software

The simulation results of the PZT, i.e., deformations, have been shown in Fig. 5.3. As expected, the largest displacements appeared on the edges of the ceramic. It needs to be mentioned, that the displacements appeared on the three axes X, Y and Z. Applying the DC voltage causes

displacements in one direction. For this case, the highest displacements were obtained in Z axis, due to the highest value of the coefficient e33 (comparing with the e.g. e_{31} or e_{23}).

To obtain the traveling wave the two pairs of ceramics oriented by 90° are needed. In addition, the two sinusoidal AC source shifted by 90° are necessary as well.

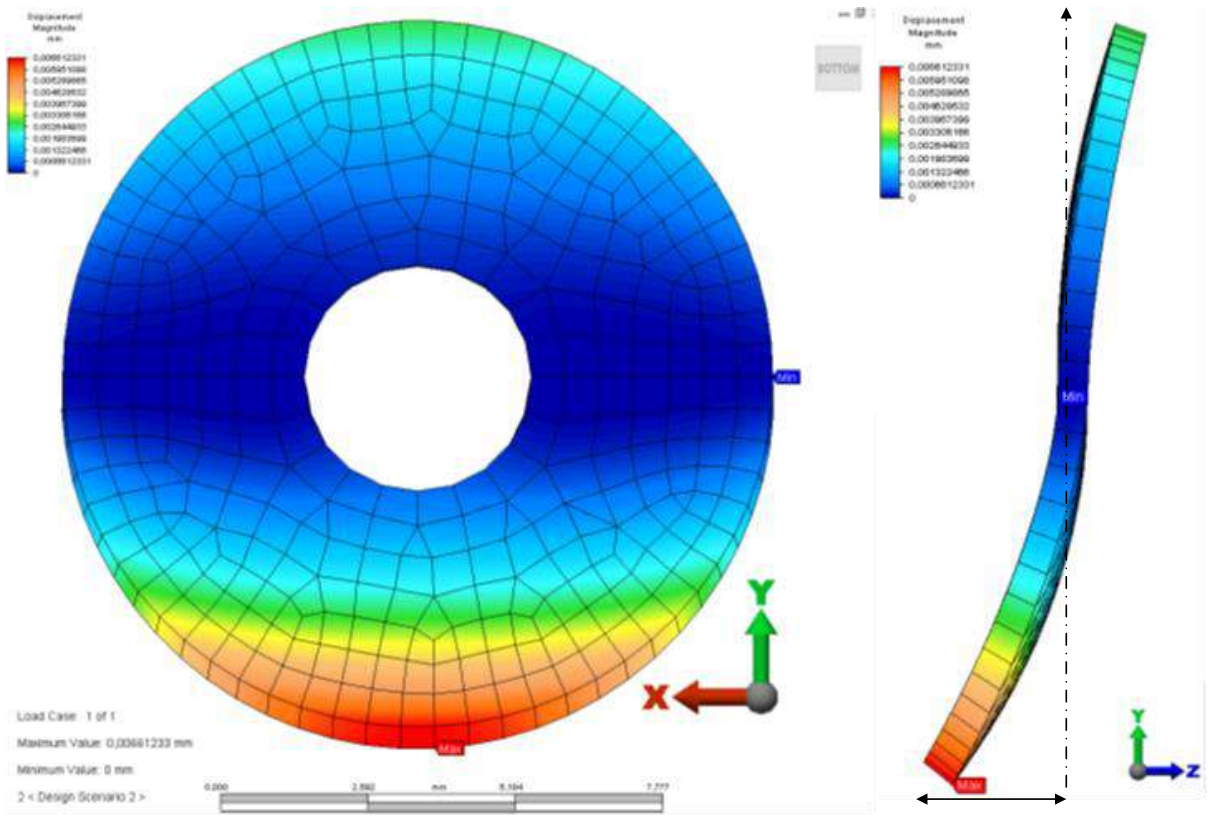

Fig. 5.4 Piezoceramic deformation determined by the FEM software

The maximum displacements occur on the edges of the ceramics in Z axis (Fig. 5.4). The results have micro meter range, the maximum value is approx. 6.66 μm. Maximum displacement in X axis are approx. 0.25 μm and in Y axis 0.86 μm.

5.3 COUNTER-MASS

During designing process some important aspects have been considered. The main goal was to obtain the resonance frequency higher than 20 kHz – ultrasonic range, diameter and length of the contra-mass should be as small as possible, because the compact structure is needed.

The prototyping process has started from the design of the basic shape of the contra-mass. The aim is to verify the resonance frequency. In the preliminary study the two material were considered - beryllium copper and aluminum. In terms of nature of counter-mass, the materials with low mechanical losses are needed. The properties of the materials are shown in Tab. 5.1. The beryllium copper is used in ultrasonic motors (Shinsei), therefore it was decided to compare it with aluminum. The decrease the mechanical loss is favored by the use of aluminum as the material of the counter-mass.

Tab. 5.1 The most important properties of the materials

Properties	Beryllium-copper	Aluminium
Density [g·cm^{-3}]	8.25	2,69
Elastic modulus [GPa]	131	69
Poisson's ratio	0.285	0.33
Yield point [MPa]	103.4	275
Stress–strain curve [MPa]	270	310
Thermal conductivity 20°C [W/mK]	110	167

5.3.1 THE FIRST STRUCTURE OF THE ACTUATOR

In this step, the chosen geometry has a shape close to the bushing, which will be a starting point for further simulation. In addition, due to the geometry the resonant frequency can be easily determined. The following parameters were chosen:

- length of the single actuator - 18 mm,
- external diameter - 12.5 mm,
- internal diameter - 5 mm.

The thickness of the piezoceramic is 1 mm, so the whole structure of stator is 40 mm long. Increasing length of the counter-mass causes the reduction of the resonant frequencies. By contrast - reducing the length of the structure, increases the resonant frequency.

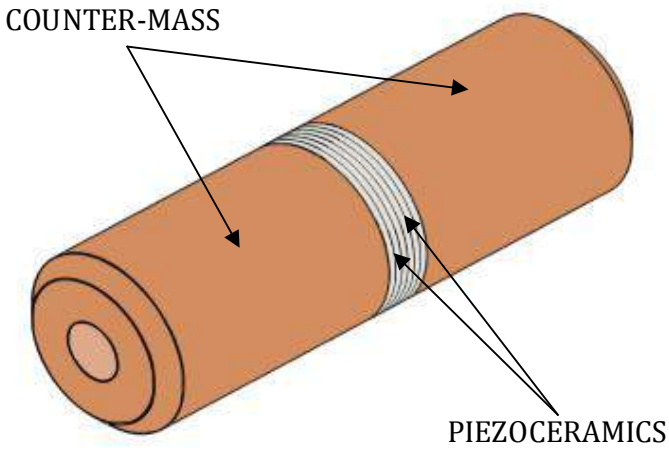

Fig. 5.5 First structure of the actuator

The precision of the simulation depends on the mesh density and mesh form. The mesh nodes was set at more than 140 thousands, which provides accurate results. It has to be mentioned that mesh has higher density in the ends of the actuator or where the shape is changing (Fig. 5.6).

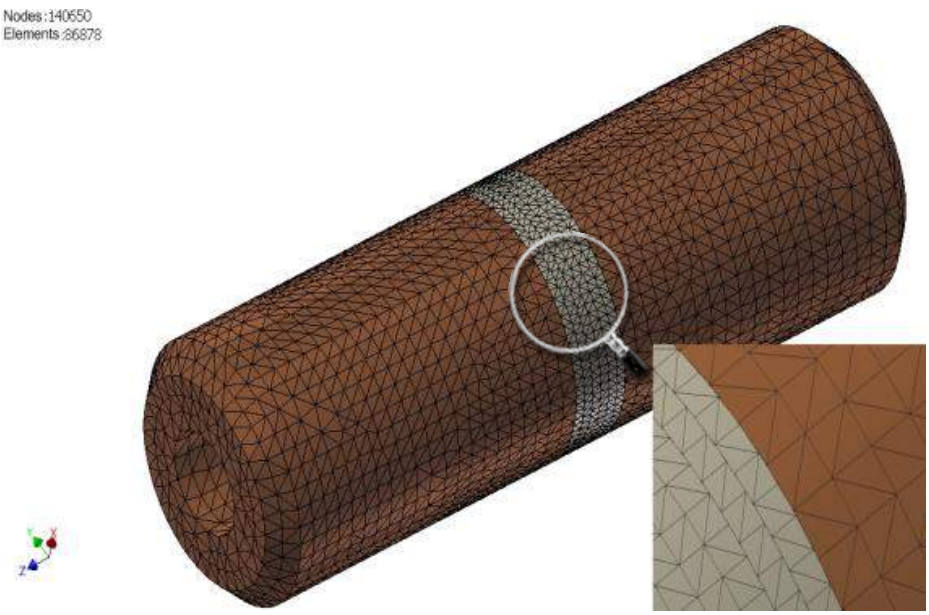

Fig. 5.6 The full view of the counter-mass mesh

The model made of aluminum has higher resonance frequencies than the model made of beryllium copper. The mechanical losses was also acceptable. In addition the aluminum has lower weight, high elasticity and it is durable. Beryllium copper has a greater Young's modulus, but higher density. One of the limitation in prototyping the actuator is the weight, which should not exceed 300 grams. Higher material density results in higher weight, so this properties should be considered as well. The detailed comparison between materials are show in Tab. 5.1.

For the static simulation the three values of the resonance frequences were obtained (in range 10 kHz to 50 kHz). The counter-mass has two bending modes and the third one is the respiration mode. The results are presented in Tab. 5.2. The obtained results are higher than assumed conditions, thus the length reduction has been considered. Fig. 5.7 shows the displacements of the cylinder according to the longitudinal axis.

At one end of the counter-mass all degrees of freedom were blocked. The biggest displacements are marked by red color. The differences between the values of resonance frequencies of the first and second mode are very small for both aluminum and copper-beryllium.

Tab. 5.2 The resonance frequencies calculated by Autodesk Inventor

No.	Beryllium copper (CuBe)	Aluminium
1.	23 579.06 Hz	29 348.45 Hz
2.	23 581.58 Hz	29 352.85 Hz
3.	29 883.94 Hz	40 120.74 Hz

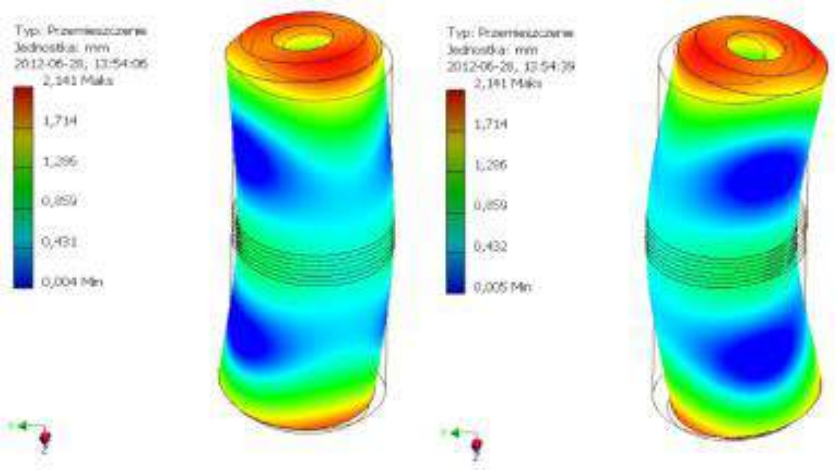

Fig. 5.7 The deformation principle in the first structure of the actuator

In the next step the designing of the full counter-mass structure was considered. As stated above, three actuators have been used. The counter-mass is constructed as a single element. All actuators are connected and oriented by 120°. This design helps to keep the solid structure and provides a good integration of mechanical parts. The full structure is presented in Fig. 5.8. The counter-mass thickness is set on 3 mm. Additionally, the part of the stator around each actuator has been made thinner. The thickness was set on 1 mm and the shape is circular. Reducing the thickness of this layer allows to maintain the higher displacements and helps to avoid the micro cracks as well. If the stator surface around the actuator is too thick the displacements are reduced, the construction is too rigid.

The stress simulations were also conducted. The purpose of this simulation was to check the compressive strength. The constant force 100N has been applied on the contact surface between rotor and stator. As can be seen in the Fig. 5.8, the contact area appears in single point, the stress value is 19 N/mm^2. This value is relatively high for the counter-mass.

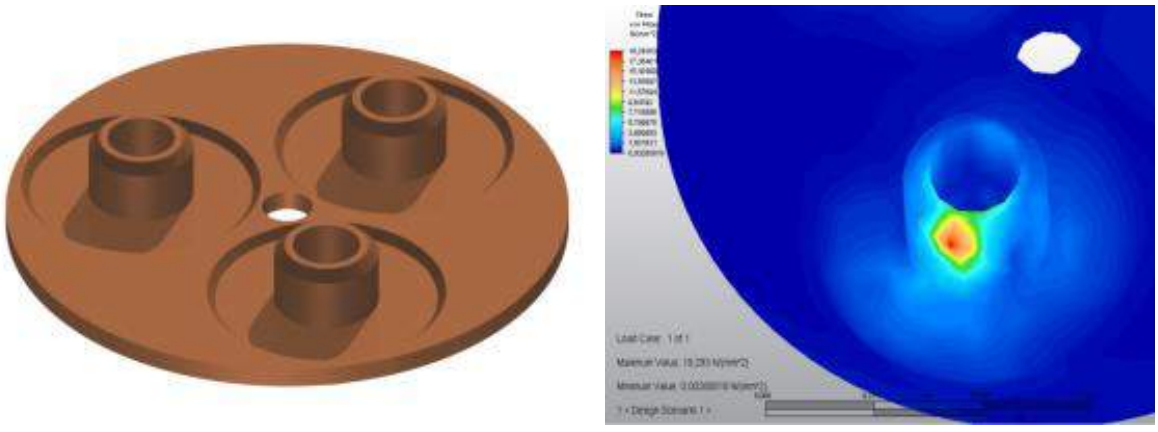

Fig. 5.8 The full counter-mass structure and the stress simulation results

The results obtained from the simulations are satisfactory and provide a good basis for further analysis. On the other hand, the stress simulation has shown that the stress level is too high and it may cause degeneration of the material.

To improve the properties of the motor, it was decided to increase the diameter at the end of the actuator. The second structure is described in the next section.

5.3.2 THE SECOND STRUCTURE OF THE ACTUATOR

To improve the torque of the motor, the contact surface between stator and rotor should be increased by resizing the diameter of the single actuator. The decided shape has been presented in the Fig. 5.9. The resonance frequencies had been changed due to modification of the dimensions. Volume had been changed as well.

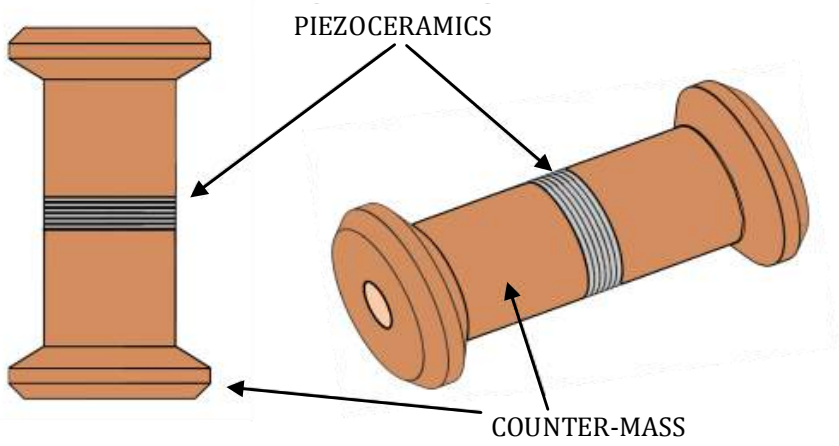

Fig. 5.9 The second structure of the actuator

The simulations of the resonance frequency were carried out. The results are shown in Tab. 5.3. Only for aluminum the results were satisfactory. The copper-beryllium results are limited to 20 kHz. This results are not acceptable. It has been decided to use the aluminum in the next simulation.

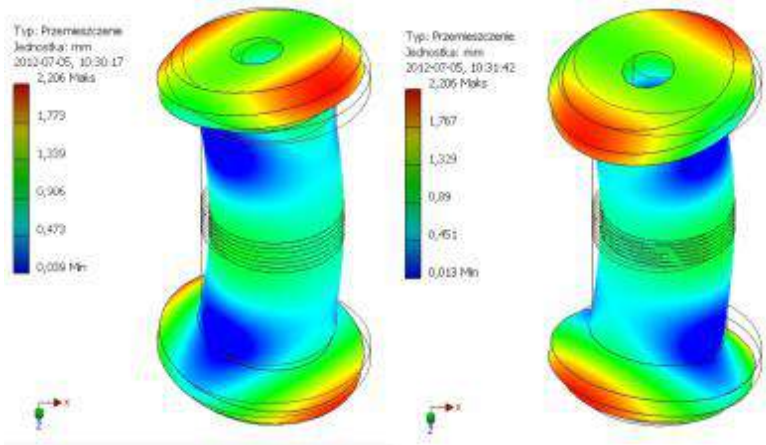

Fig. 5.10 The deformation principle in the second structure of the actuator

The length of the actuator has been reduced from 20 mm (first structure) to 16 mm. Including the piezoceramics the total length of the actuator is 36 mm. Due to reduction of the length the resonance frequencies were increased. From the simulation the three resonance modes have been found, as in the first simulation. The first and second mode are shown in Fig. 5.10.

Tab. 5.3 The resonance frequencies calculated by Autodesk Inventor

No.	Beryllium copper (CuBe)	Aluminium
1.	20 462.48 Hz	25 938.12 Hz
2.	20 698.08 Hz	25 940.74 Hz
3.	20 733.13 Hz	27 072.08 Hz

Referring to the above considerations, the stress simulation has also been carried out. Mechanical stress values obtained in the counter-mass are lower due to increasing the dimensions in the actuator's end. Comparing with the previous shape, the contact surface is greater. The highest value of mechanical stress is 14 N/mm^2. The results are presented in Fig. 5.11. Although, the properties have been improved but the contact surface is still not satisfactory.

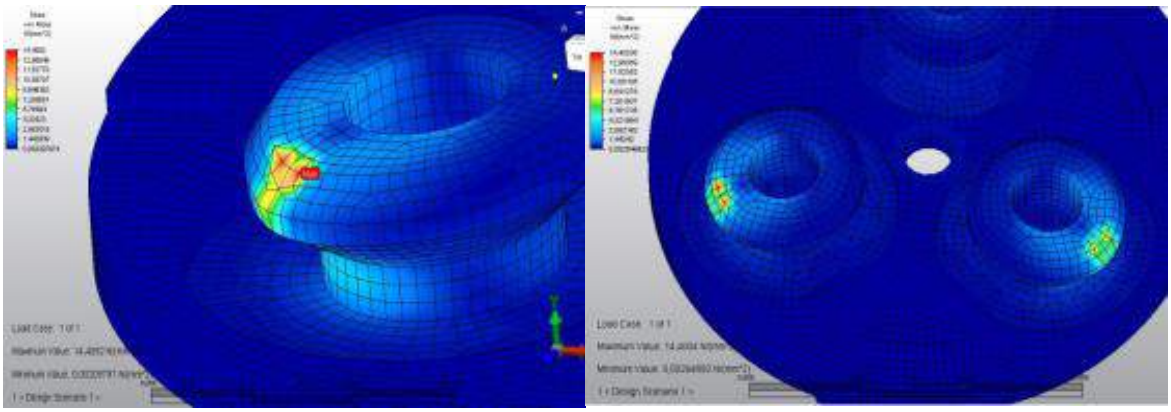

Fig. 5.11 Stress simulations results of the second actuator

5.3.3 THE THIRD STRUCTURE OF THE ACTUATOR

Basing on above simulation results, the final shape (geometry) of the actuator has been determined (Fig. 5.12). Keeping the proper actuator proportions, the contact rotor/stator surface has been increased. This solution should improve the following mechanical properties: torque, rotation velocity and pressing distribution rotor/stator.

In turn, reducing the length of the single actuator the resonance frequencies have been increased. To get the required frequency the length has been set up to 15 mm (1 mm less than the previous one).

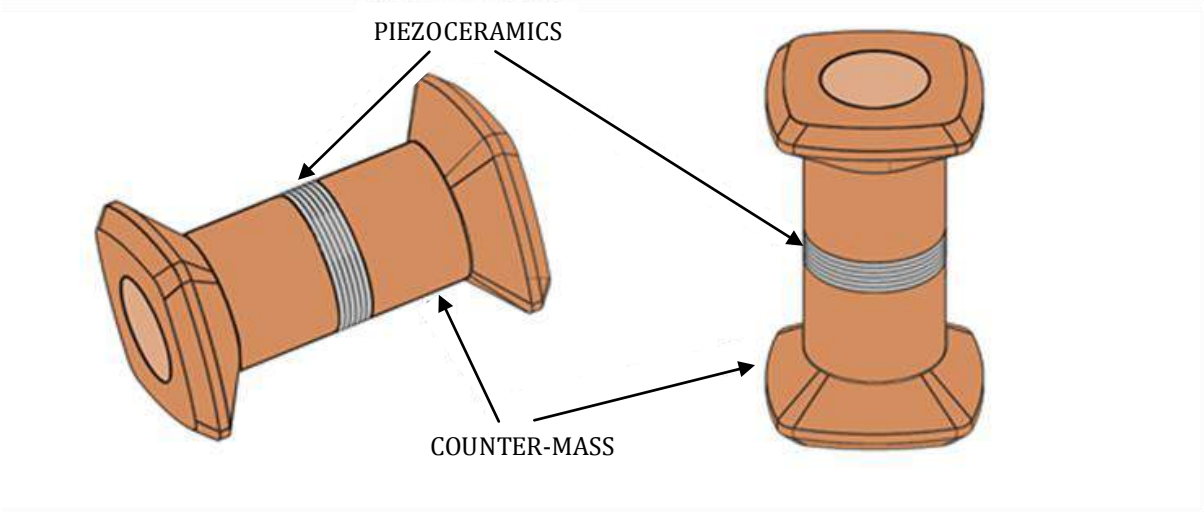

Fig. 5.12 The final shape of the actuator

The resonance frequencies have lower values than for the second structure but still acceptable. In the physical model the resonance frequencies will be lower due to pressure force. The purpose to obtain the resonance frequencies above 20 kHz is reached. The results are presented in Tab. 5.4.

Tab. 5.4 The resonance frequencies calculated by Autodesk Inventor

No.	Aluminium
1.	25 615.32 Hz
2.	25 636.73 Hz
3.	25 675.23 Hz

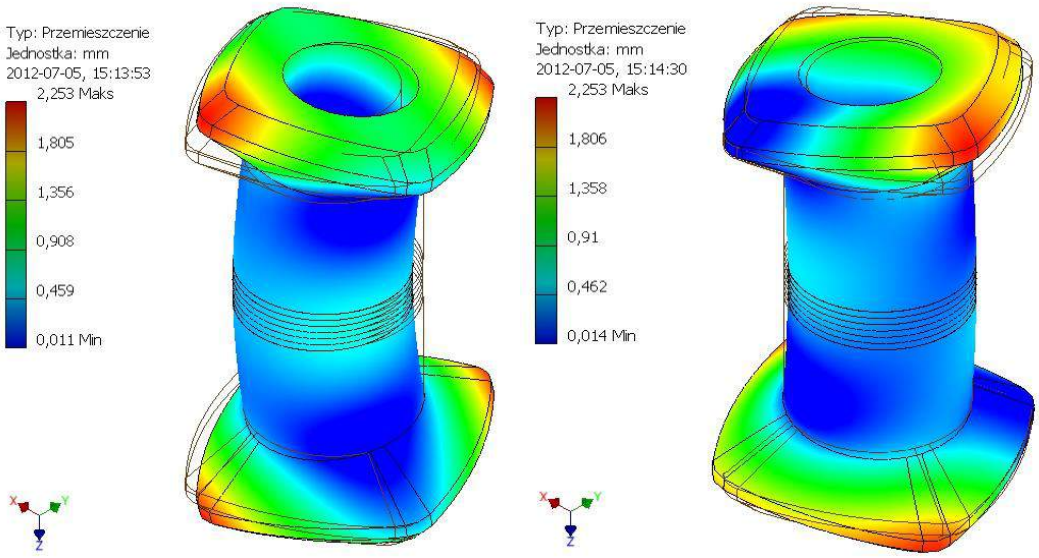

Fig. 5.13 The deformation principle in the third structure of the actuator

As expected, the stress is spread on the whole surface now. This type of structure is increasing the stability and extends working cycle of the motor. The maximum stress value is 9 N/mm^2 which is an acceptable value. The results are shown in Fig. 5.14.

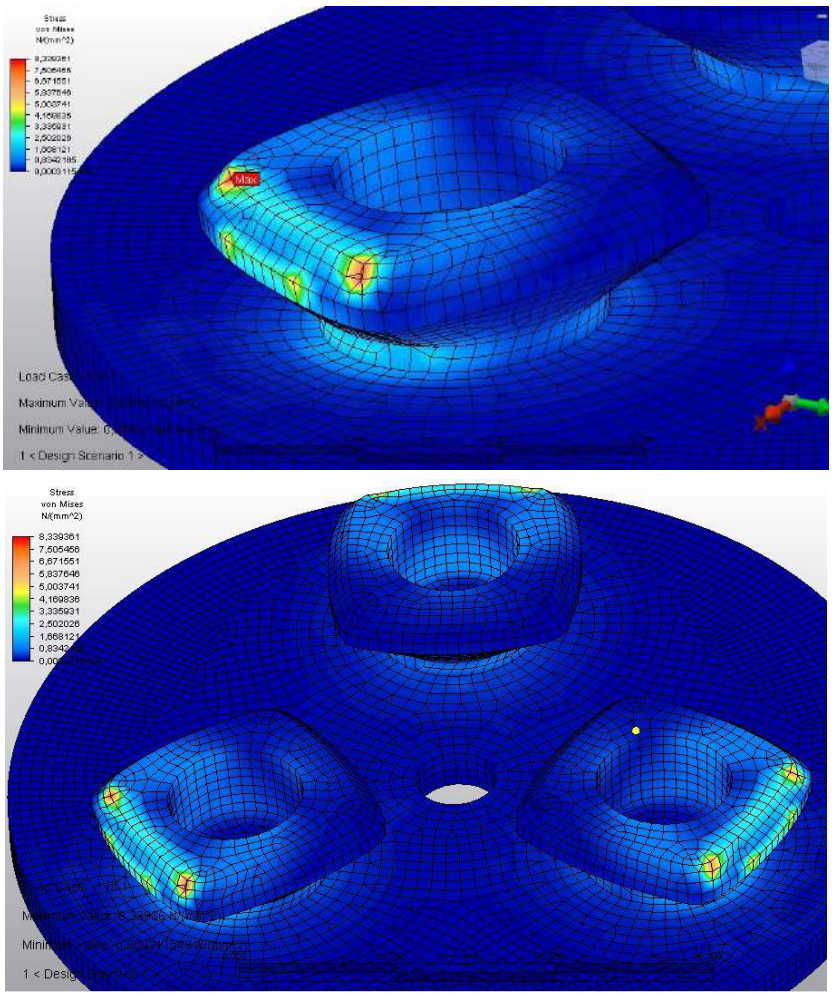

Fig. 5.14 The stress simulation results for the final version of stator

In summary, the static and stress simulations have given very good results. Resonance frequencies are in inaudible range due to used material and proper shapes of the actuators. Due to use the aluminum, the mechanical losses are lower in comparison to steel. Another important advantage of aluminum is the lower weight. The density is 2.71 g/cm3 and the volume of the counter-mass is 13 887 cm3, so the weight is 38g.

As was mentioned above, the structure of the motor is symmetrical and consists of two contra-mass, piezoceramics, two rotors, two ending plates and springs. It keeps construction more stable and helps to obtain better mechanical characteristics.

5.4 ROTOR

The conception of the rotor was prepared using the approach in [**6**], [**70**], [**71**]. The full structure has been presented in Fig. 5.15.

The dimensions of this part has been fixed as following: the external diameter is 60 mm, the internal is 10 mm and the inclination angle at 45°. The internal diameter is greater than diameter

of the shaft. For this solution the rotor has few degrees of freedom, it helps to obtain better adjustment between surfaces of the stator and rotor.

Rotor is not fixed on the shaft directly, thus the top side has holes where special spring could be placed. The springs are a kind of mechanical transmission/coupling. To create a rotational movement the ending plate will be used.

Fig. 5.15 Rotor full view

To get different pressure condition, the special springs from "Smalley" company have been chosen (Fig. 5.16). They offer an advantage of space savings when used to replace coil springs. By reducing spring operating height, the wave springs also produce a decrease in the spring cavity. With a smaller assembly size and less material used in the manufacturing process, a cost savings is quite good. Typically, a wave spring will occupy an extremely small area for the amount of work it performs [**85]**.

The ordered sizes of the springs have 8 mm and 10 mm diameter. Combination of this two sizes gives better torque, adjustment and no latency. Shim ends provide a 360° contact surface when compared to standard springs. The shim-ends under load more evenly distribute the springs force upon adjacent components. This feature is similar to the concept of double-disc grinding springs for a flat surface. Shim ends have also been used to affix springs to mating components, as a flat locating surface that may be attached by various methods in the assembly process.

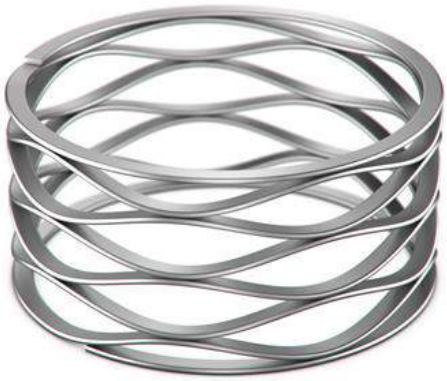

*Fig. 5.16 Crest-to-Crest Wave Springs with Shim Ends **[85]***

Two structures of rotors with different materials had been prepared. The first structure was made of steel. The second structure was prepared using Nylatron GF30-66.

Particularly, the polymeric materials are interesting because they have good physical properties. A polymer is a substance composed of macromolecules known as monomers into a covalently bonded chain or network. Nylatron is a tradename for a family of nylon plastics. Typically it is filled with molybdenum disulfide lubricant powder. It is used to cast plastic parts for machines, because of its mechanical properties and wear-resistance. Nylatron is used in rotary lever actuators where unusual shapes are required. They are also used as heavy-duty caster wheels, normally as a replacement for cast iron or forged steel.

5.5 CONCLUSIONS

Using the developed FEM model of the prototype MPM the resonance frequencies and stress values have been determined. Their values are following:

- resonance frequency - 25.6 kHz,
- stress – 9 N/mm^2.

Comparing the resonance frequency values determined using the analytical model (25.9 kHz) and FEM model (25.6 kHz) of the prototype MPM, it should be underlined that develop analytical model of the MPM can be considered as a relatively highly accurate model.

The maximum stress (9 N/mm^2) can be considered as an acceptable value for the prototype MPM.

The dimensions and parameters determined using analytical model and numerical will be verified on the built prototype MPM in the laboratory.

6 MANUFACTURING AND MEASUREMENTS OF THE PROTOTYPE MPM

In this chapter the manufacturing process, assembling and measurements of the prototype multicell piezoelectric motor has been described. A flowchart of the measurement procedure is shown in Fig. 6.1, and an exploded view of the prototype MPM is presented in Fig. 6.2.

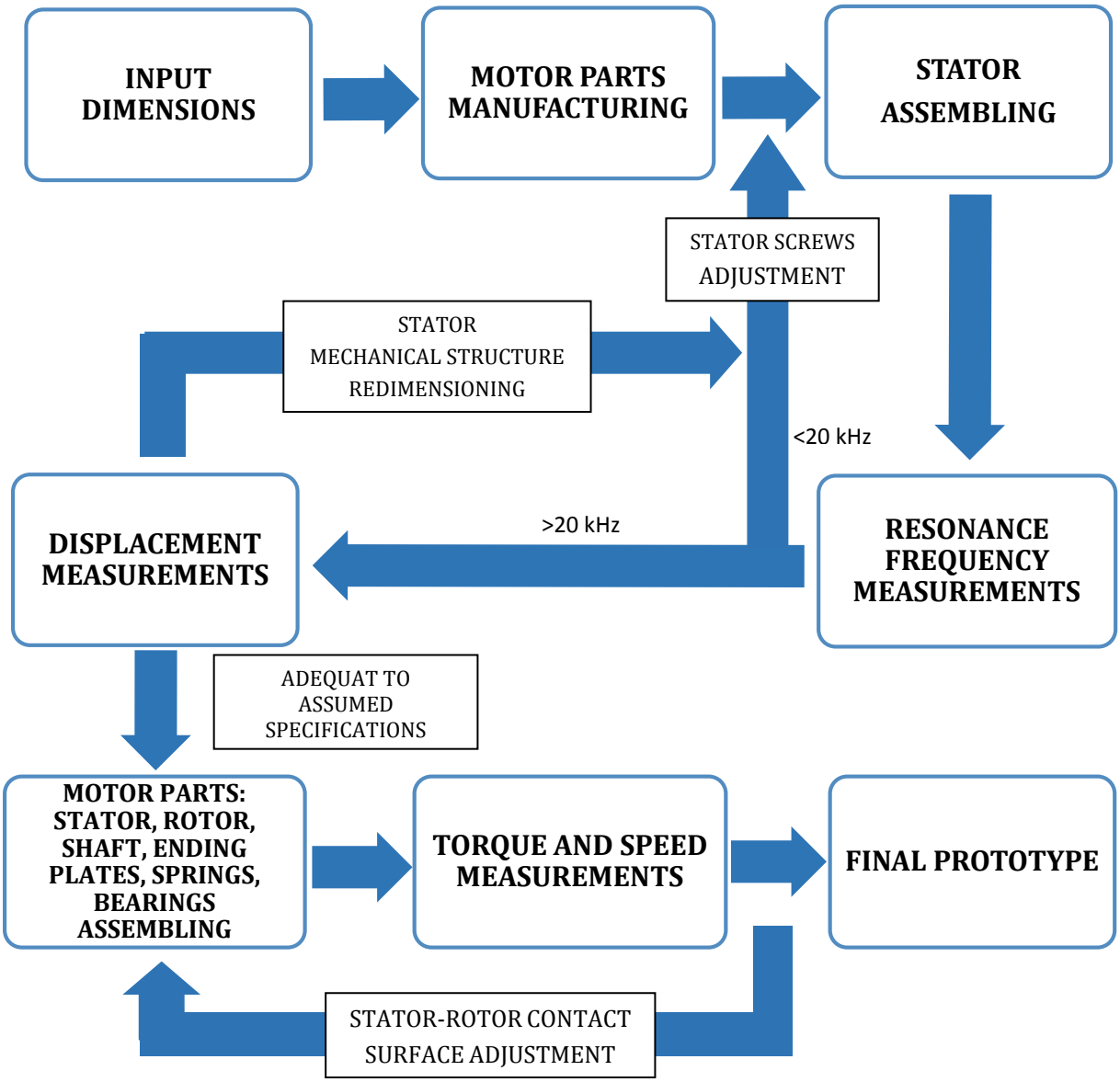

Fig. 6.1 The flowchart measurement procedure of the prototype MPM

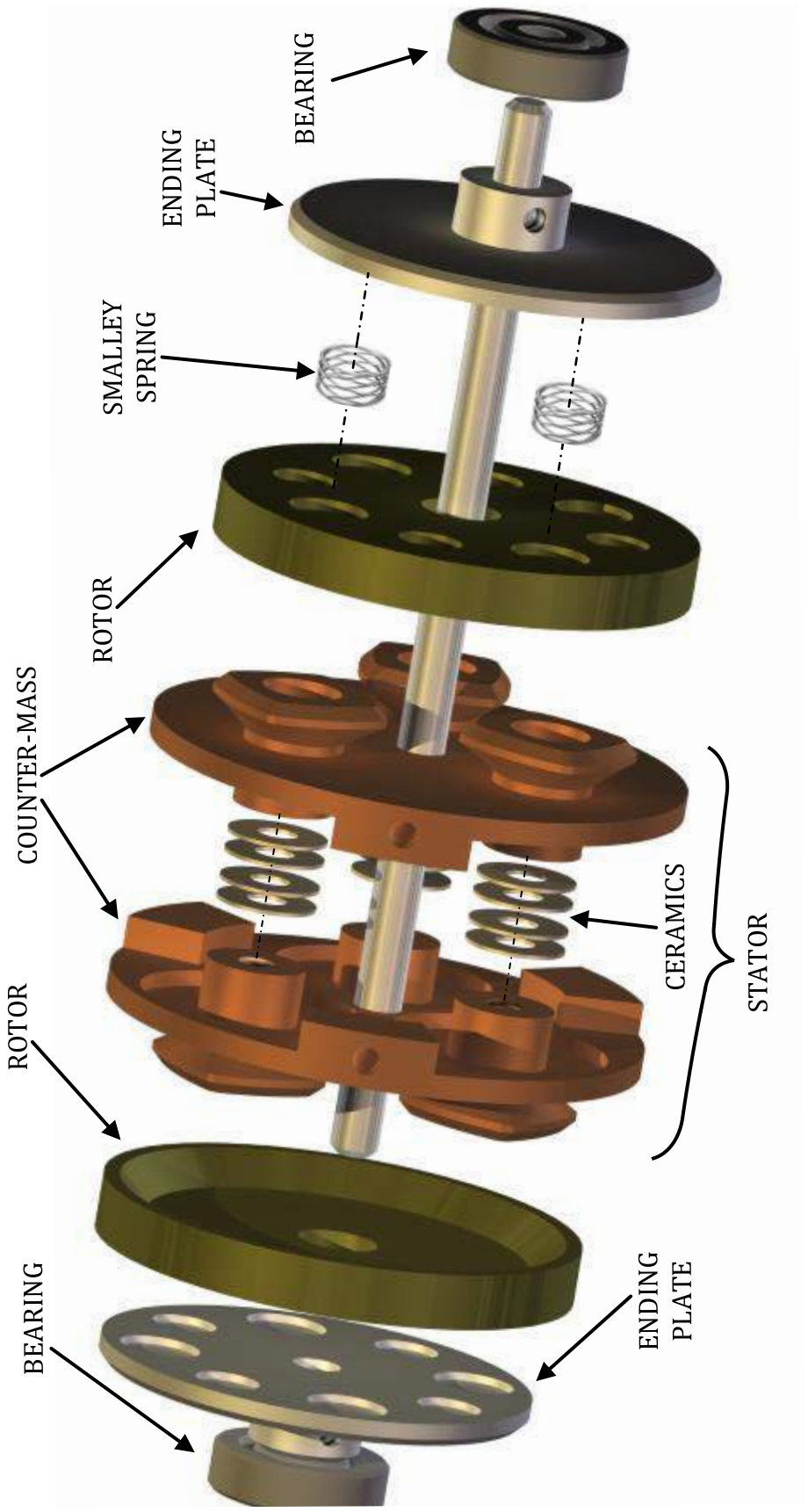

Fig. 6.2 The exploded view of the prototype multicell piezoelectric motor

6.1 MOTOR PARTS MANUFACTURING

6.1.1 POLARIZATION PROCESS OF THE PIEZOCERAMICS

Materials that reveal a significant and an applicable piezoelectric effect fall into the three main groups: natural (quartz, Rochelle salt), synthetic crystals (lithium sulfate, ammonium dihydrogen phosphate), and polarized ferroelectric ceramics, including selected polymer films. The main piezo material that is used for engineering applications is ferroelectric ceramics, especially, the Plumbum Zirconate Titanate (PZT). The PZT ceramics is characterized by high coupling factors, piezoelectric and dielectric constants over an extended temperature and a stress range. Because of their natural asymmetric structure, the crystal materials exhibit the piezoelectric effect without further processing. However, ferroelectric ceramics must be artificially polarized, because before the polarization process the electrical dipoles inside the crystal structure are oriented chaotically, and the total dipole moment is zero. When the strong electric field (a few kV/mm) is applied to the material, the electrical dipoles are being aligned to the lines of the field (Fig. 6.3). Due to that, the remnant polarization is being retained, and the material has the piezoelectric effect.

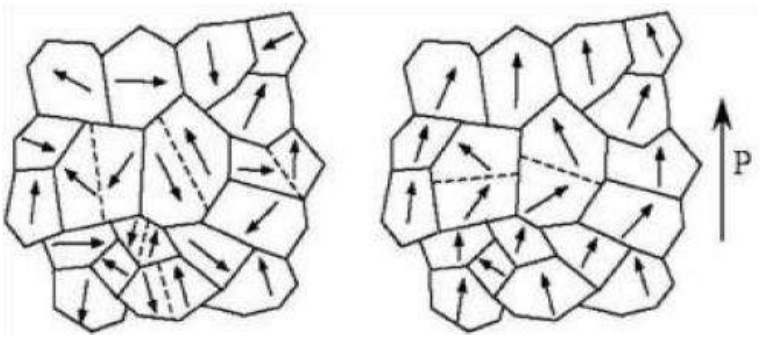

Fig. 6.3 Polarisation process of the ferroelectric domains that are subjected to an external electric field

It is crucial to heat the material over its Curie point during the application of the high electrical filed. Typical polarization process is described on the graph shown in Fig. 6.4.

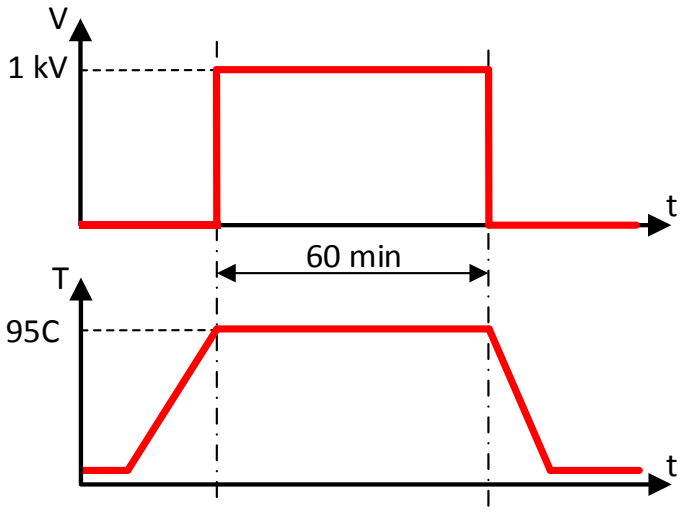

Fig. 6.4 An example of the polarization cycle

Briefly explained, the preparation stages of the ceramic are following:

1. laser sectorization of the ceramics, dividing it into two areas of the same size;
2. ceramic polarization, i.e., the ceramics are placed in a container of dielectric oil between the two + electrodes of the power supply, the voltage value is 1.0 kV, and it lasts minimum 60 min;
3. verification of polarization, i.e., checking the value of d_{33} coefficient of the ceramic;
4. capacity calculation.

At initial stage of the motor construction you have to carry out the preparation of the piezoceramics. Certain tests have been carried out on the piezoceramics polarization. The tests have shown that the polarization in the laboratory has given better d_{33} coefficient parameter than the purchased from the manufacture.

At the beginning, the piezoelectric material has to be sectorized into halves because the negative and positive charge will be applied (Fig. 6.5). The ceramics shall be sized with 1 mm width and around 0.1-0.2 mm depth. The PC controlled laser has been used for this task. After that, the results of the laser cut have been verified under the microscope to check if the gap is large enough (Fig. 6.6).

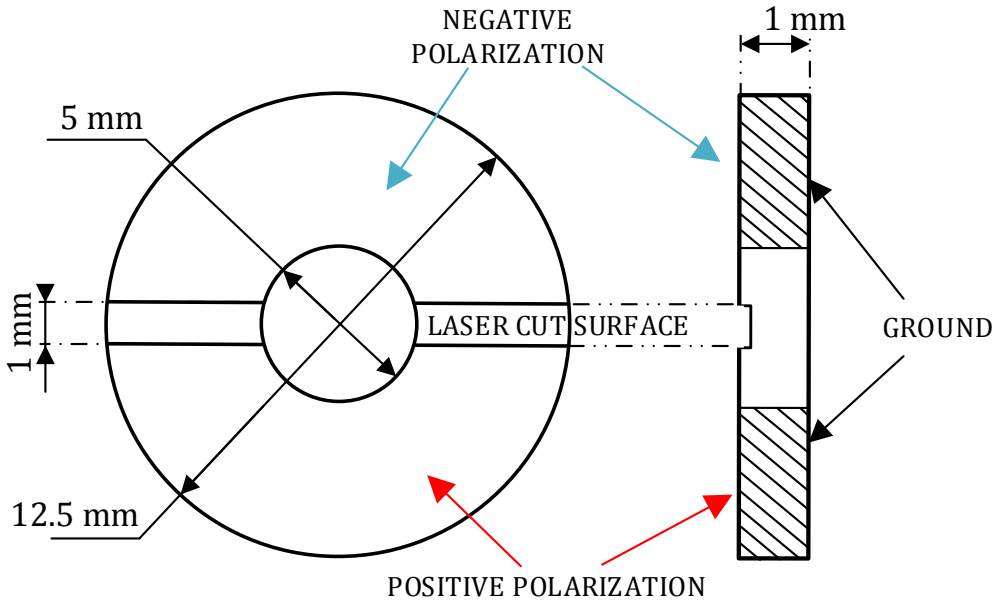

Fig. 6.5 A sketch of the used piezoceramic

Fig. 6.6 Sectorization of the ceramics: on the left – microscope, on the right - laser

The prototype MPM has three resonance actuator, and for each actuator four piezoceramic have been used. To begin the polarization process the ceramics have been placed in a special holder submerged in oil (Fig. 6.7a). The crucial issue was to evenly distribute the ceramics on the holder so there would be not electrical arcs that could affect negatively the polarization process. The process of the polarization, heated in a special oven to 95˚C, lasted about one hour. After the proper temperature was reached, the voltage of +/- 1 kV was applied to the piezoceramics (Fig. 6.7b and Fig. 6.8a).

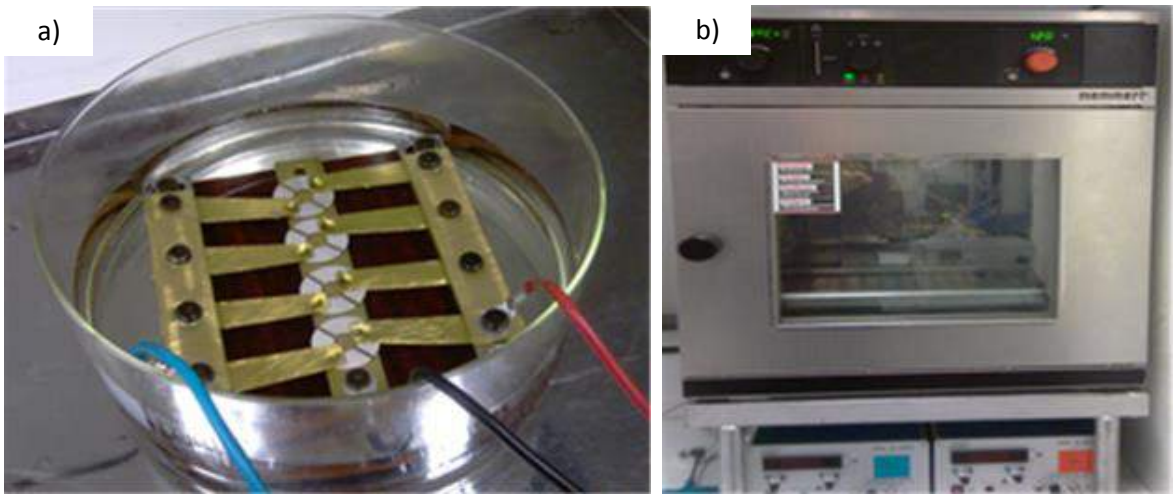

Fig. 6.7 The polarization process of piezoceramics – a) the special holder with positive and negative electrodes, b) the furnace

In order to check if the polarization were properly done, it was necessary to use a device to measure the piezoelectric constant (d_{33}) (refer to chapter 2.2) – "Model ZJ-4B series quasi-static d_{33} Meter" (Fig. 6.8 b) [**86**]. The coefficient d_{33} for the ceramics (given by the manufacturer) was at average $250 \cdot 10^{-12}\, C/N$. The parameters obtained in the laboratory were better, i.e., the d_{33} has a range from $290 \cdot 10^{-12}\, C/N$ to $380 \cdot 10^{-12}\, \frac{C}{N}$, and its average value was around $350 \cdot 10^{-12}\, C/N$. It

should be noticed that the measured results were not equal for all piezoceramics. The ceramics having the highest coefficient values have been chosen.

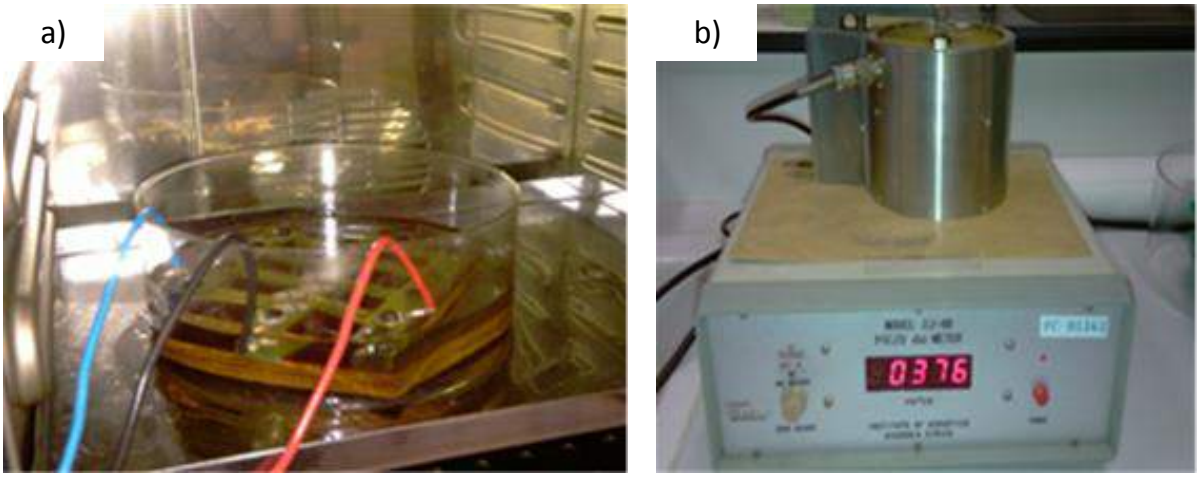

Fig. 6.8 The polarization process of the piezoceramics: a) holder with piezoceramics in the furnace, b) measuring constance d_{33}

At the last stage the calculation of the piezoceramics capacity was done. It can be calculated using the following formula:

$$C_0 = \frac{\varepsilon_r \cdot \varepsilon_0 \cdot S}{\frac{e}{2}} \tag{6.1}$$

where, ε_r is the relative permittivity of the ceramic, ε_0 is the relative permittivity of the vacuum, S_c is the surface of the ceramic, and e is thickness of the ceramic. And therefore:

$$Sc = \pi \cdot \left(R_{ext}^2 - R_{int}^2\right) = \pi \cdot (6.25^2 - 2.5^2) = 103.08\, mm^2 \tag{6.2}$$

$$Se = 2 \cdot a(R_{ext} - R_{int}) = 7.5\ mm^2 \tag{6.3}$$

where, S_c is the total surface of the ceramic, and S_e is the ceramic surface removed by laser. Thus the ceramic surface is:

$$S = Sc - Se = 95.6\ mm^2 \tag{6.4}$$

And finally, the single ceramic capacity:

$$C_0 = \frac{8.85 \cdot 10^{-12} \cdot 1000 \cdot 95.6}{\frac{0{,}001}{2}} = 1.69 \cdot 10^{-9}\, F \tag{6.5}$$

For the single phase, the two piezoceramics are connecting parallel, and therefore:

$$C = 2 \cdot C_0 = 3.38^{-9}\, F \tag{6.6}$$

Next, the equivalent circuit parameters of the motor structure have been measured. The values (e.g. of the blocking capacity) are presented in Fig. 6.9 and Fig. 6.10. Comparing these results with the results calculated using eq. (6.6) it can be noticed that the results are similar. The obtained results for C_0 of the prototype are: 3.23 nF for phase *A,* and 3.31 nF for phase *B*. The calculated value are 3.38 nF, respectively. Approximately the error is 4.48%.

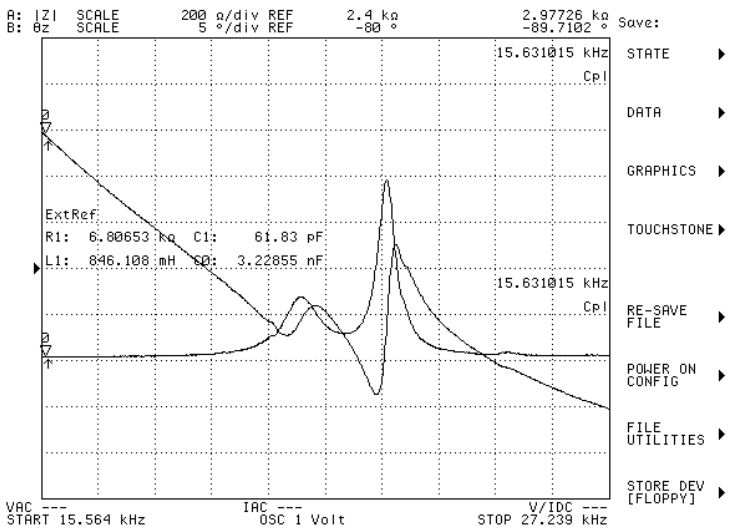

Fig. 6.9 The measured equivalent circuit parameters using impedance analyzer: phase A of the actuator

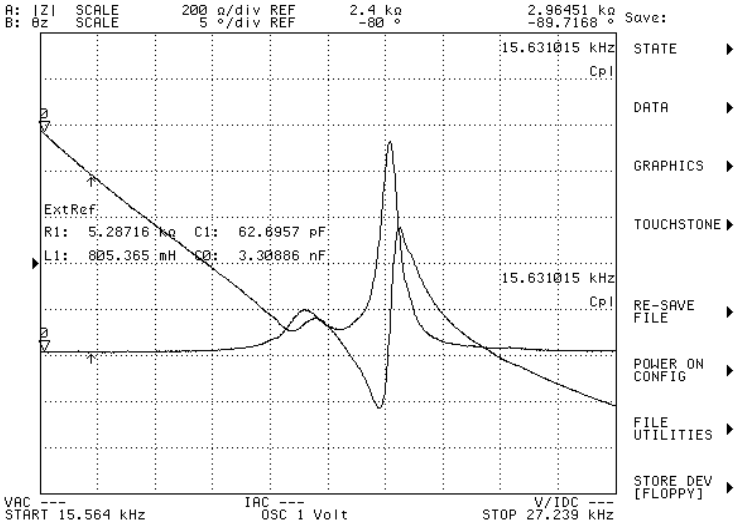

Fig. 6.10 The measured equivalent circuit parameters using impedance analyzer: phase B of the actuator

Additionally, the impedance analyzer can be used to measure other parameters of the motor equivalent circuit, like resistance. The result of the measured resistance are following:

$$\text{phase } A\text{: } R = 6.8\ k\Omega \qquad \text{phase } B\text{: } R = 5.3\ k\Omega.$$

6.1.2 MOTOR PARTS PREPARATION

In Fig. 6.2 the virtual model of the MPM has been presented. In comparison to a simple piezoelectric motors, this prototype motor has a more complicated topology. The shape of the used resonance actuators is more complicated than for used common solutions. The possibility to manufacture the counter-mass using the 3D printer has allowed to produce it, regarding its complicated structure. The material used for the counter-mass production is aluminum due to its high resonance frequencies. It should be noticed that using the 3D printer changes the

material properties, so the frequencies will be lower than for the solid piece of aluminum. The counter-mass surface were not enough smooth, so the stator-rotor contact surfaces has been polished. On the other hand, 3D printer ensures much faster and easier production of a single part. Also, it is more expensive manufacturing method, than using the milling machine (computer numerical control - CNC). The single piece has been shown in Fig. 6.11. The prototype counter-mass has been produced by French company INITIAL [**87]**. The technical documentation (the drafting and the STL files as well) was developed using Autodesk Inventor. The STL file – StereoLithography - is a file format native to the stereolithography CAD software developed by 3D Systems. This format is very useful for rapid prototyping because it describes only the surface geometry of the three-dimensional object without any representation of color, texture or other common CAD model attributes.

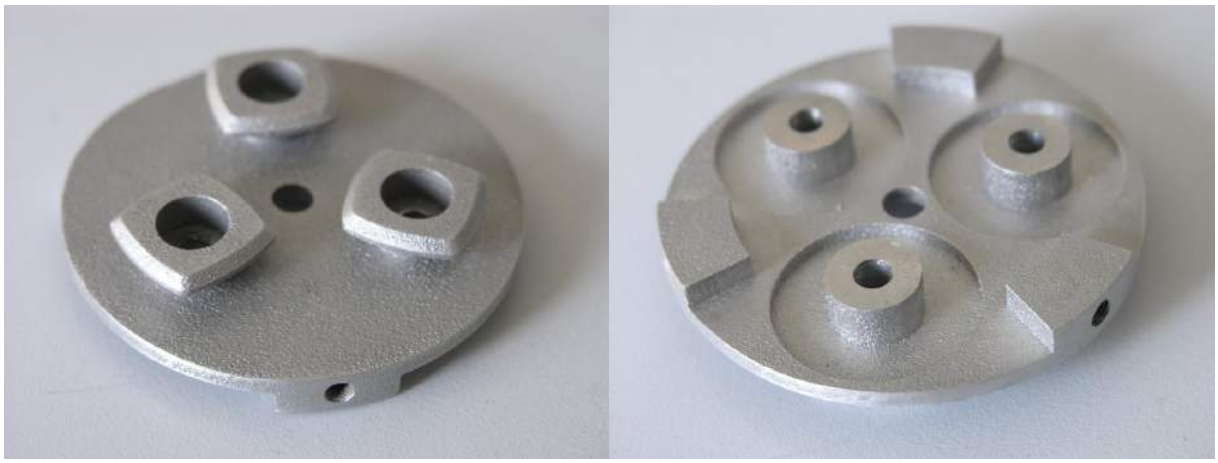

Fig. 6.11 The outside and inside view of the prototype counter-mass

It should be underlined that during the assembling process of the prototype MPM the high accuracy was required. The stator consists of two counter-masses, and 12 ceramics (four for each actuator). The diameter of the stator is 50 mm and each actuator has the diameter of 12.5 mm. As stated above, in chapter 5.2, the surface around the actuator was 1 mm thick, and diameter of the surface was 8 mm. During the designing process it was considered if thickness was properly determined. It is easier to remove some material than to add an extra layers afterwards.

The ceramics have to be oriented as it is shown in Fig. 4.2 – the two phases arranged by 90°at each other. The ceramics have to perform in pairs to obtain traveling wave. In theory, to get the same resonance frequencies for each actuator, the screw shall be fixed with the same torque. In practice, due to minor differences in the structure, the resonance frequencies are set with different torque and force. The main purpose was to obtain the same frequency for each actuator. The designed construction of the single actuator requires to use five electrodes – three electrodes for the mass, one for the phase A, and one for the phase B.

The first rotor prototype has been made of steel by milling machine. This material gives a good coefficient of friction that provides minimum abrasion of the outer surface. The ending plate has been manufactured by milling machine also, from aluminum to reduce the weight of the motor. The case was produced using 3D printer from Nylatron to reduce the weight as well. All motor components are presented in Fig. 6.12. The assembled stator is shown in Fig. 6.13.

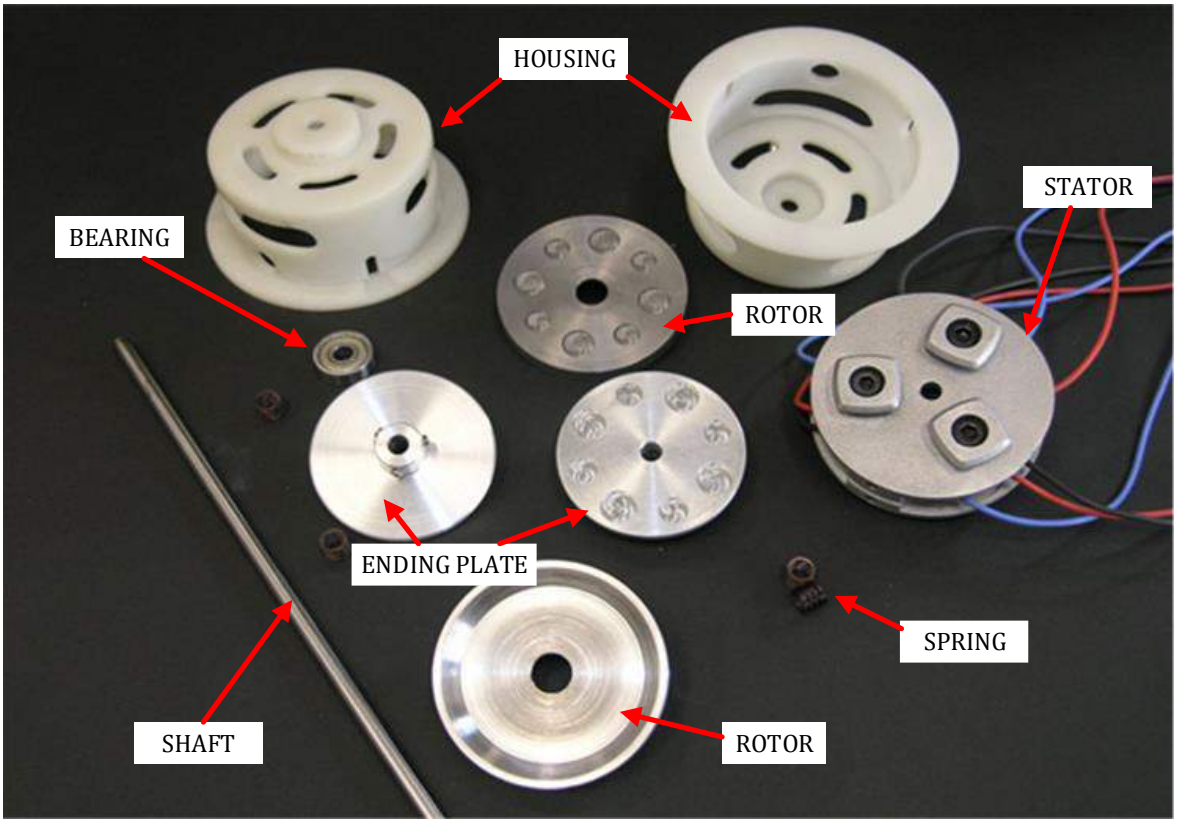

Fig. 6.12 The all parts of the prototype MPM

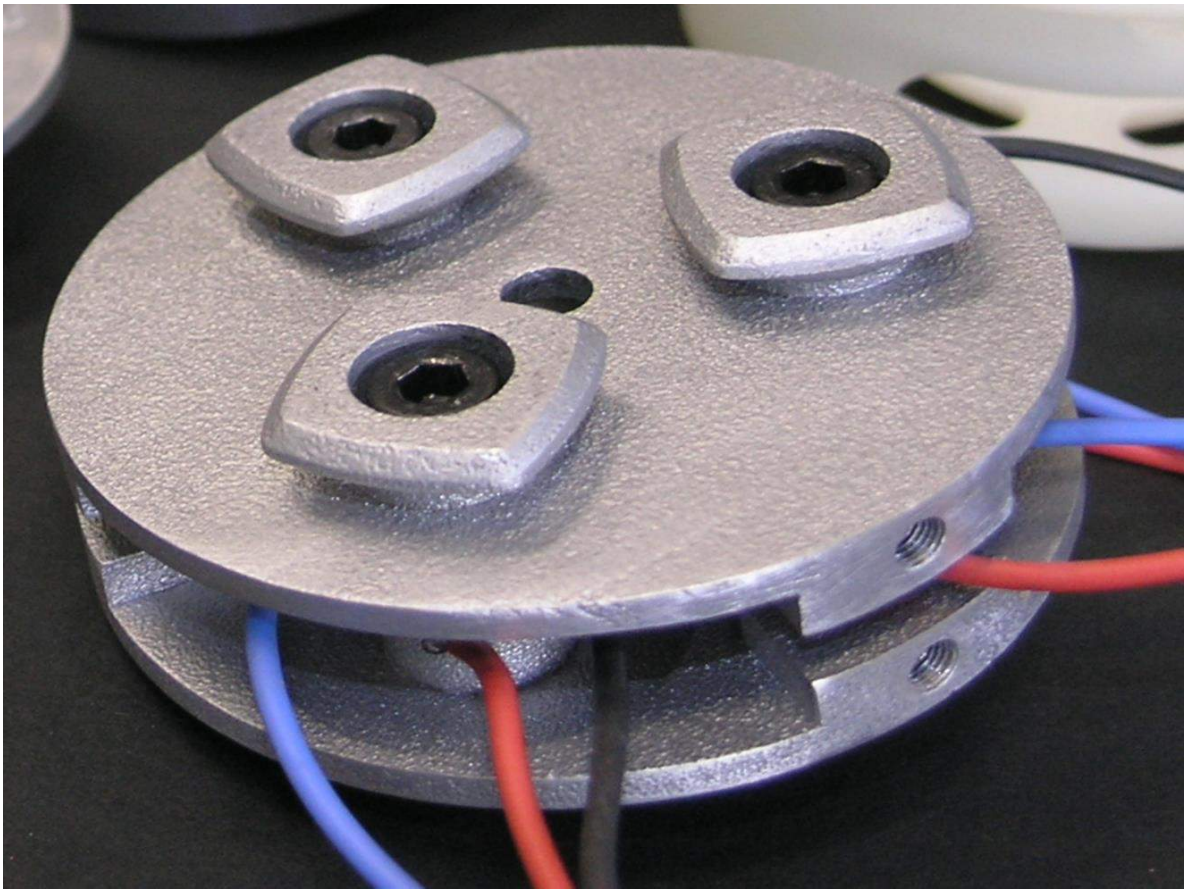

Fig. 6.13 The stator of the prototype MPM: two counter-masses, piezoceramics and electrodes

6.2 RESONANCE FREQUENCY MEASUREMENTS OF THE PRELIMINARY STRUCTURE

After assembling the prototype MPM, the measurements of the resonance frequencies have been carried out. It is considered as the first step for the verification process of the prototype MPM.

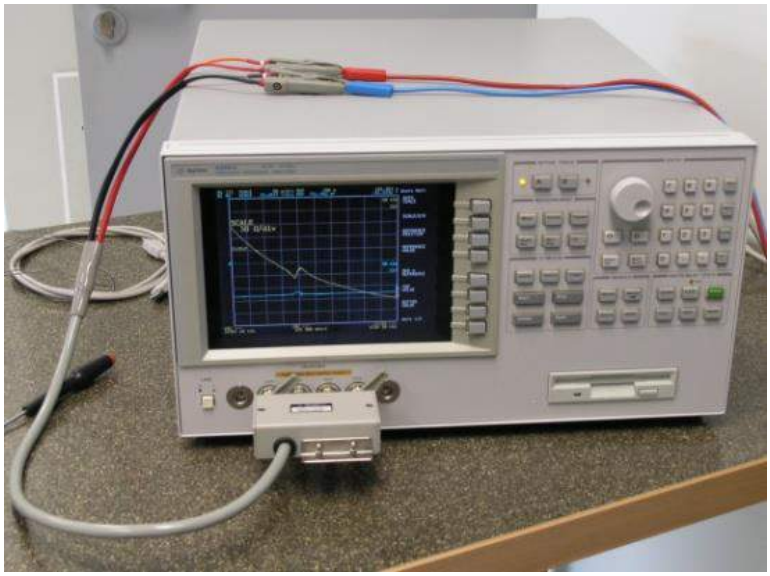

Fig. 6.14 Impedance analyzer – type Agilent 4294A

By detecting the minimum value of the impedance the resonance frequency has been measured using the impedance analyzer type Agilent 4294A (Fig. 6.14) **[88]**. This analyzer is a precision impedance analyzer (integrated solution for efficient impedance measurement), and also for analysis of components and circuits. It covers a broad test-frequency range (40 Hz to 110 MHz) with basic impedance accuracy: +/-0.08 %. Its High Q/Low D accuracy enables the analysis of low-loss components. The equivalent circuit function is used to fit a circuit model to the measured data, or to the simulate device performance based on the value of each circuit model element. Also, this analyzer has five equivalent circuit models to choose from.

The simulation of the resonance frequency using the Autodesk software has given the outcome of approx. 25.5 kHz. The measurements have been performed on each phase of the actuator. It is important to obtain the same resonance frequency for each phase of the single actuator. The value of the resonance frequency varies depending on the tightness of the combining screws. The higher was the tightness of the combining screws, the higher resonance frequency value has been obtained, due to the larger force acting on the piezoceramics. The measurement results are shown in Fig. 6.15 - Fig. 6.20.

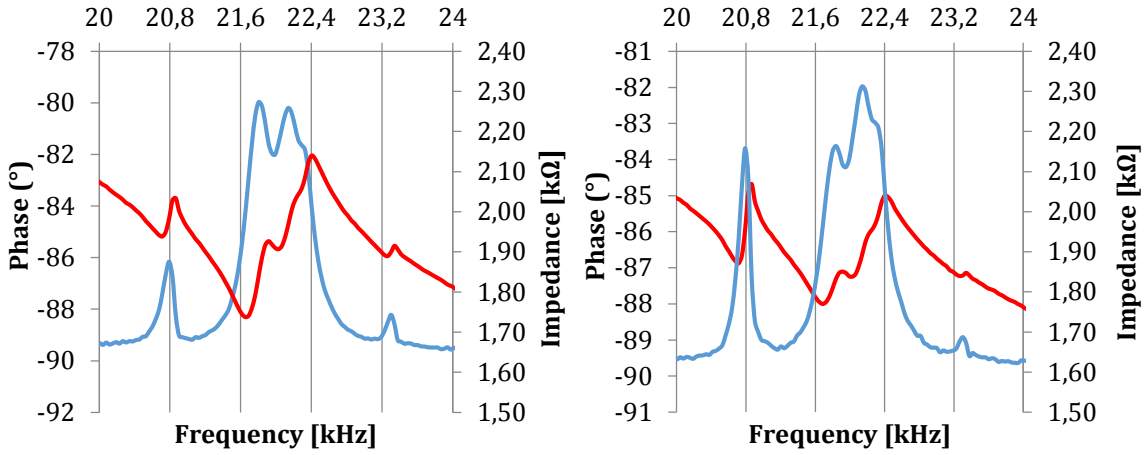

Fig. 6.15 The resonance frequency measurements: phase A and B (separated) for the "first" actuator

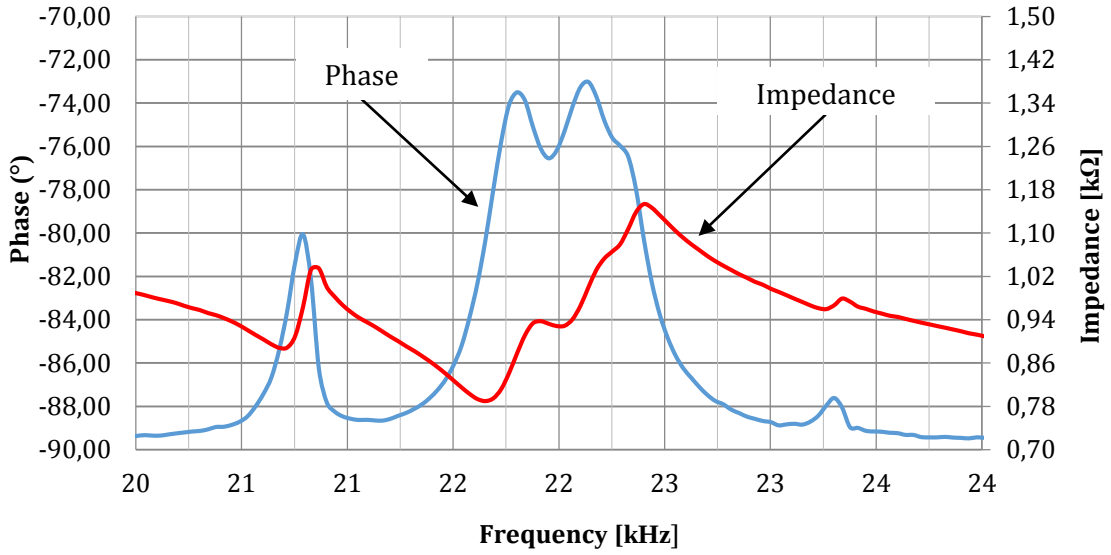

Fig. 6.16 The resonance frequency measurements: phase A and B (not separated) for the "first" actuator

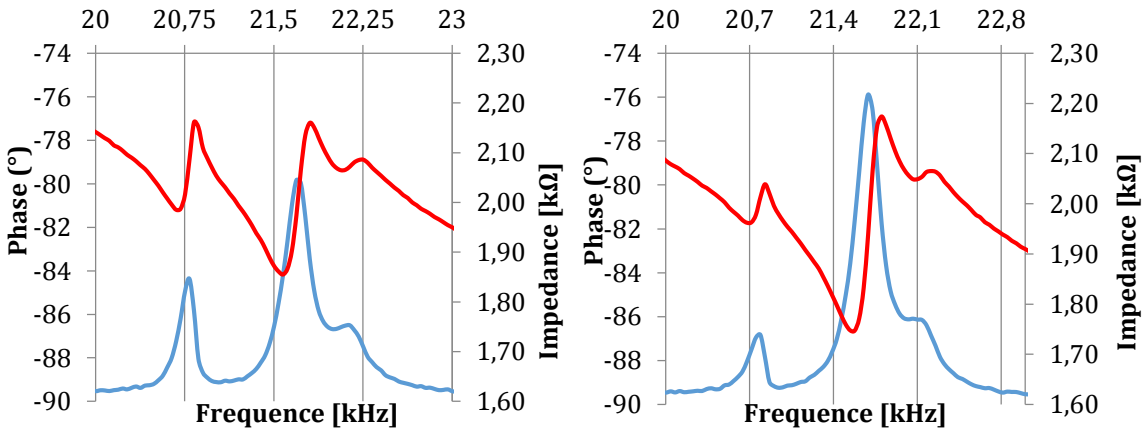

Fig. 6.17 The resonance frequency measurements: phase A and B (separated) for the "second" actuator

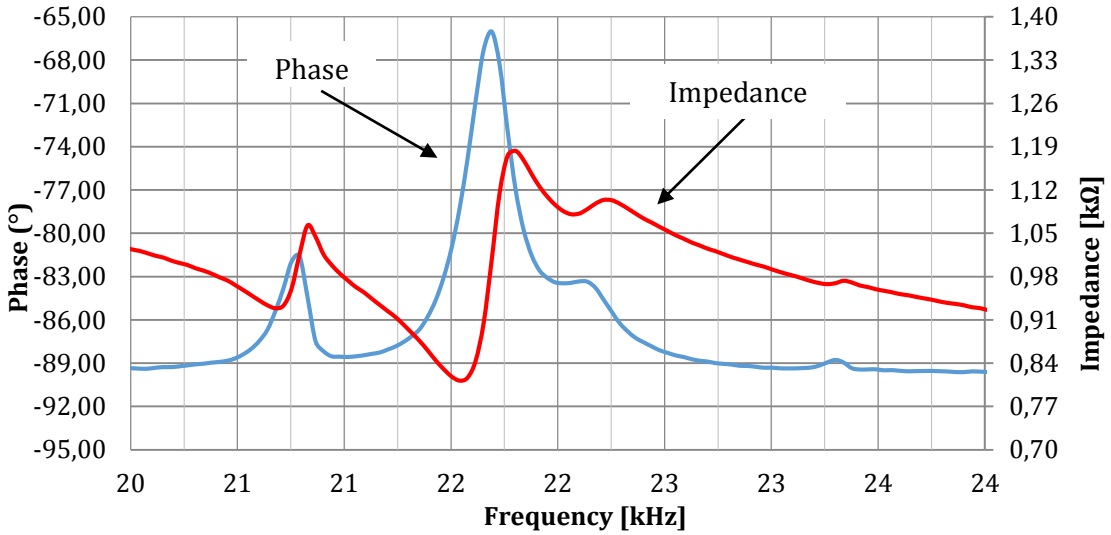

Fig. 6.18 The resonance frequency measurements: phase A and B (not separated) for the "second" actuator

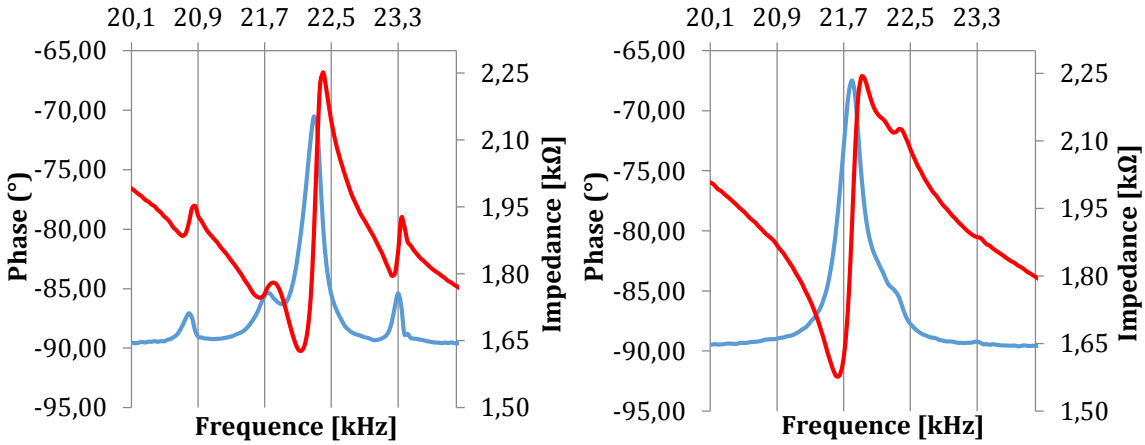

Fig. 6.19 The resonance frequency measurements: phase A and B (separated) for the "third" actuator

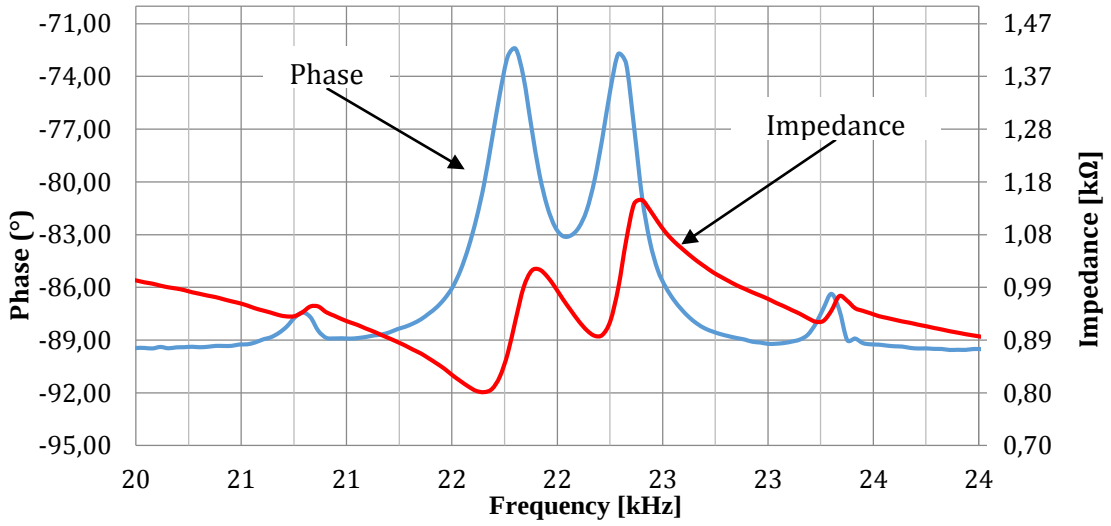

Fig. 6.20 The resonance frequency measurements: phase A and B (not separated) for the "third" actuator

Due to adjustment of the stator components, the mechanical resonance frequency was set to about 21,5 kHz. As mentioned above, the resonance frequency depends on the force applied by the screw and the tightening torque. The purpose of this assembling stage was to tighten all the actuators with the combining screws, with the same resonance frequencies.

The resonance frequency for the third actuator is not the same as for the others one. The issue was the proper orientation of the piezoceramics or the fact that all the ceramics were not sectorized properly. The difference between actuators was approx. 600 Hz, which can be assumed as an acceptable value. It should be pointed out that the tightness of the combining screws is not maximal because the material which counter-mass is made of is vulnerable to damage/fault.

6.3 DISPLACEMENT MEASUREMENTS

At the next stage of the prototype MPM verification the displacements caused by the ceramics have been measured. The displacements were verified at two places: on the contact point between rotor/stator, and around the single actuator. The vibration amplitude was measured by a laser vibrometer which detects vibrations along the stator.

The test characteristics are following:

- amplitude of supplying voltage – 100V,
- voltage frequency – 21.8 kHz,
- scale conversion of laser – 25 mm $\cdot s^{-1} \cdot V^{-1}$.

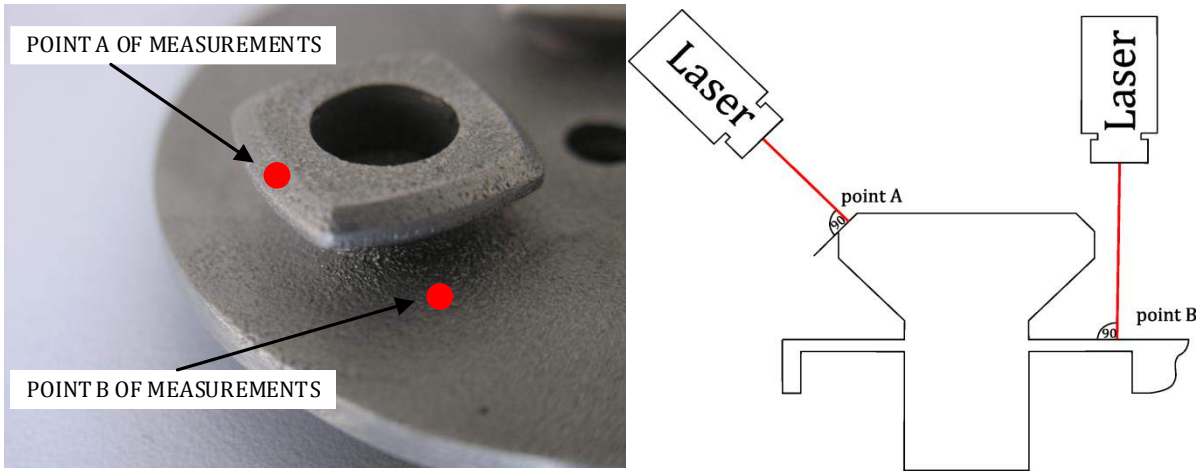

Fig. 6.21 Displacement points measurements

The measurement at point *A* was made on the surface which comes into contact with the rotor (Fig. 6.22). It was intended to check the size of the deformation and verify briefly the predesign stage. The obtained results has been considered satisfactory and consistent with the assumed objectives. The value of the sinusoidal displacements was 1.1 μm, and amplitude 0.55 μm.

Comparing the measured results to the calculated results using the analytical model (developed in chapter 4.5), it can be considered that the radial displacements 0.97 μm are acceptable.

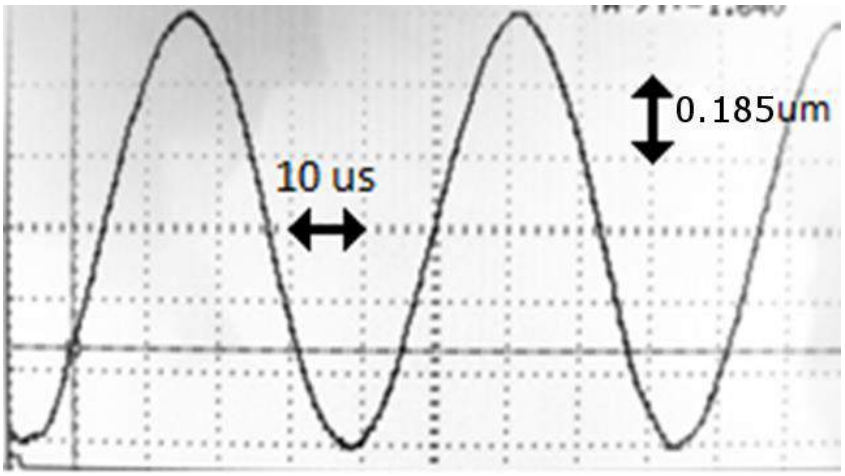

Fig. 6.22 Displacement measurements at point A

A measurement at point *B* was made on the flat surface near the placement of the actuator. It was intended to test the effect of vibration of the actuator for the entire structure. The displacements value was 0.65 μm (Fig. 6.23).

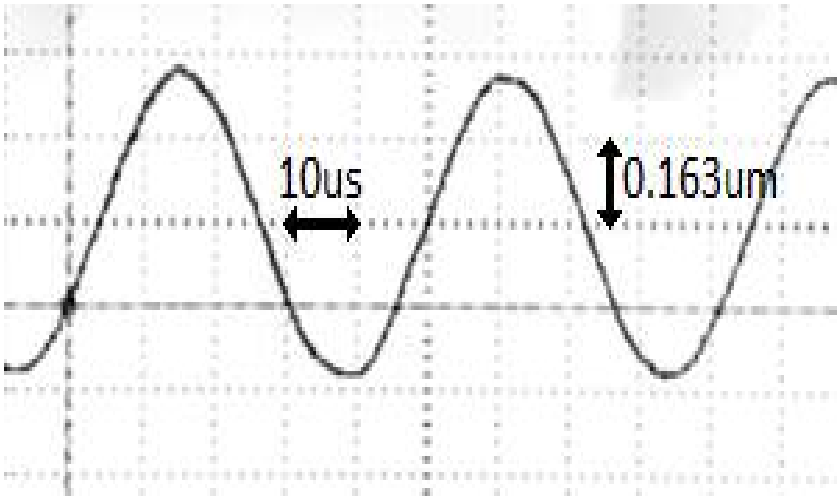

Fig. 6.23 Displacement measurements at point B

Comparing the displacements on the top of the actuator with the displacements on the flat surface around the actuator, it can be noticed that the displacements on the flat surface are smaller. The values are decreasing if the distance of the point B is increasing from the actuator. However, the value at point B is too high. These are parasite displacements which are interrupting the used working principle of the motor.

The measured displacement values can be considered satisfactory, and the measured displacement waveforms are sinusoidal as it was required. To eliminate the parasite displacements, it is necessary to reduce the thickness of the surface. The stator structure has been properly corrected, i.e., the thickness of the surface has been changed from 1 mm to 0.2 mm using the milling machine.

6.4 RESONANCE FREQUENCIES MEASUREMENTS OF THE FINAL STRUCTURE

After redimensioning the stator mechanical structure, i.e., the part of the counter-mass around each actuator palcement has been made thinner (refer to the right part of the Fig. 6.11), the resonance frequencies have been measured again. The measurement results are shown in Fig. 6.24 - Fig. 6.26.

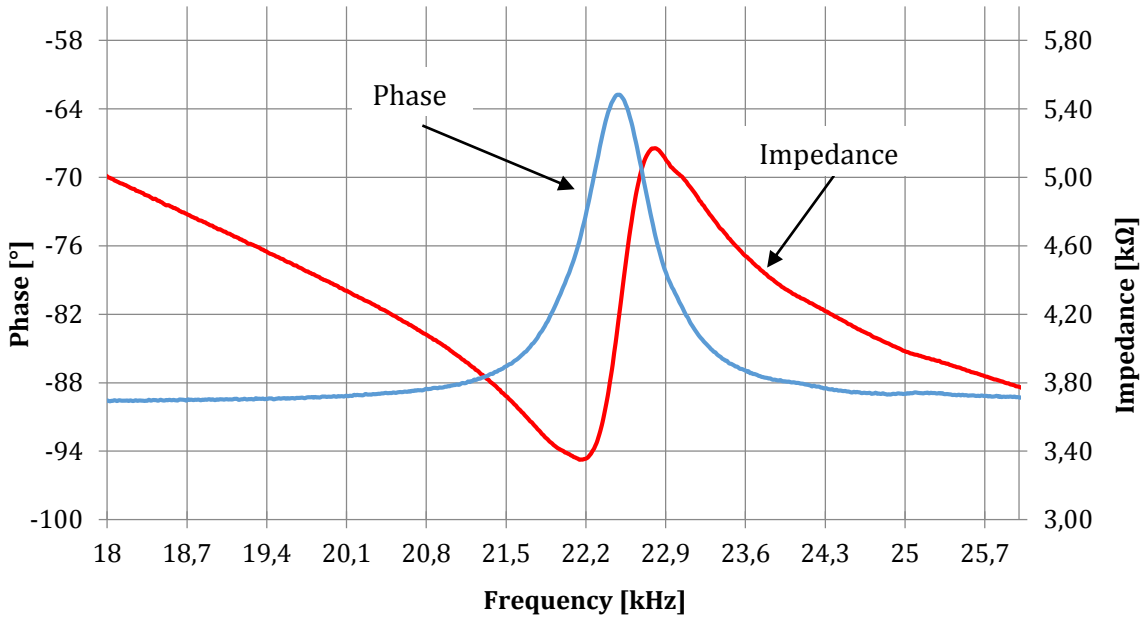

Fig. 6.24 The resonance frequency measurements: phase A and B (not separated) for the "first" actuator

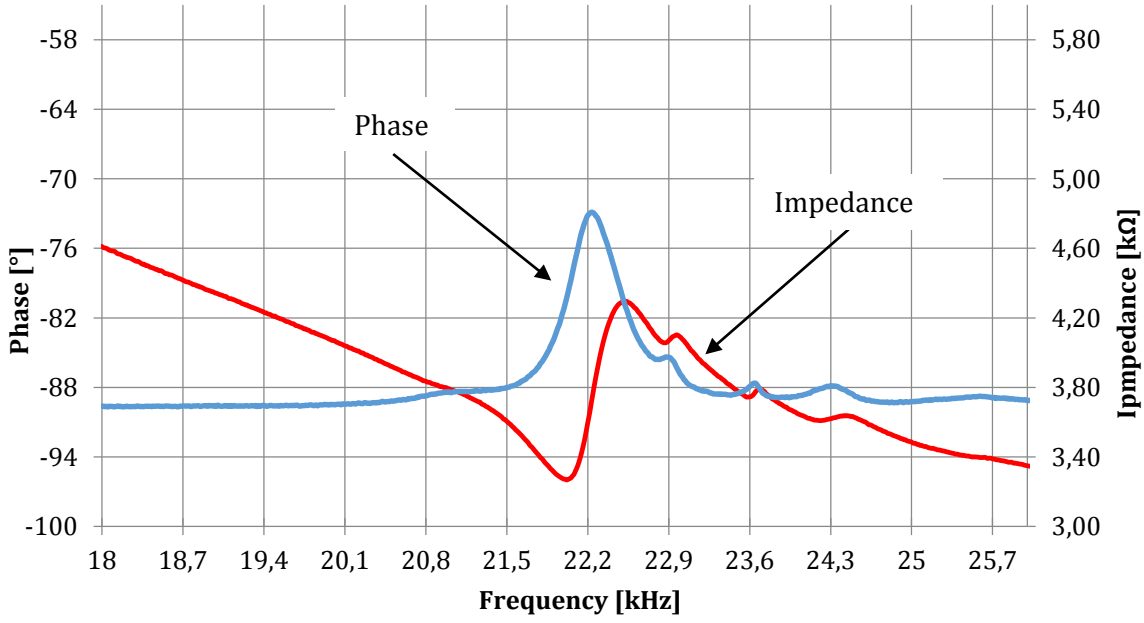

Fig. 6.25 The resonance frequency measurements: phase A and B (not separated) for the "second" actuator

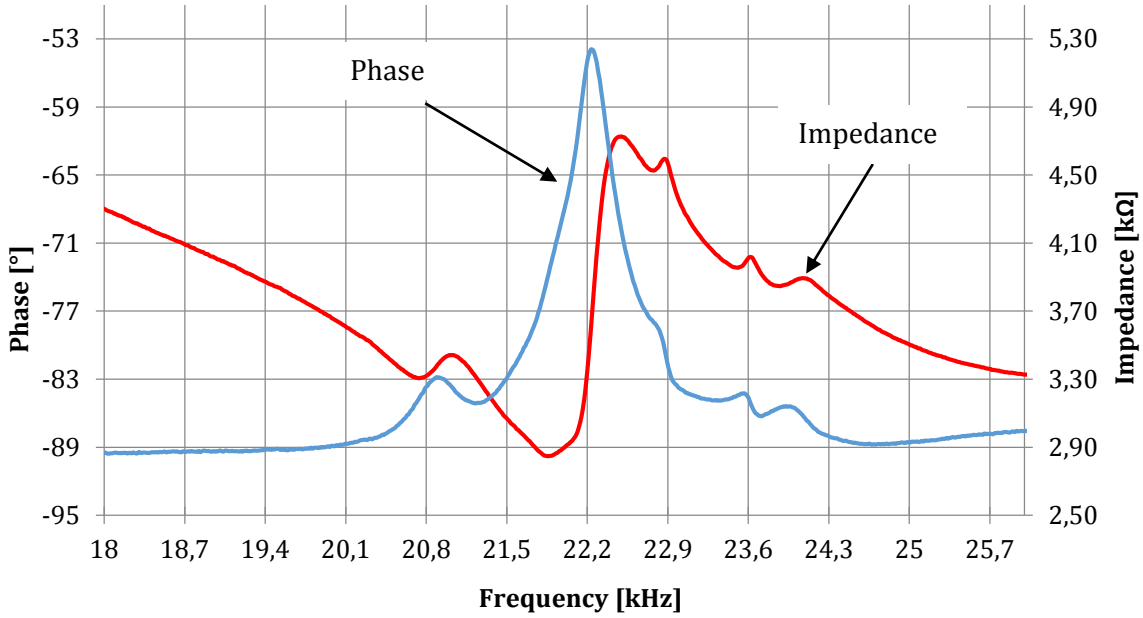

Fig. 6.26 The resonance frequency measurements: phase A and B (not separated) for the "third" actuator

Due to the improvement of the mechanical structure a better resonance frequency value has been obtained. Comparing it with the previous measurement results, the subsequent measurements have shown smoother waveforms. As could be noticed, there are no distortions and no extra peaks. All actuators have similar resonance frequency, since the difference is less than 200 Hz. The frequency is set on 22.0 kHz.

The results of the subsequent resonance frequency measurements have proved that they are higher, and are less dispersed, while comparing it with the previous measurements, as it was required.

6.5 TORQUE VS. SPEED CHARACTERISTIC MEASUREMENTS

The parts of prototype MPM have been assembled as shown in Fig. 6.27. The ending plate with four springs on each side is propelled by the rotor. Certain tests of the rotating movement have been performed using different force values acting on the stator. The first prototype performance test has been done using the linear power amplifier as power source. The second one has been done using the powerful tool - dSpace.

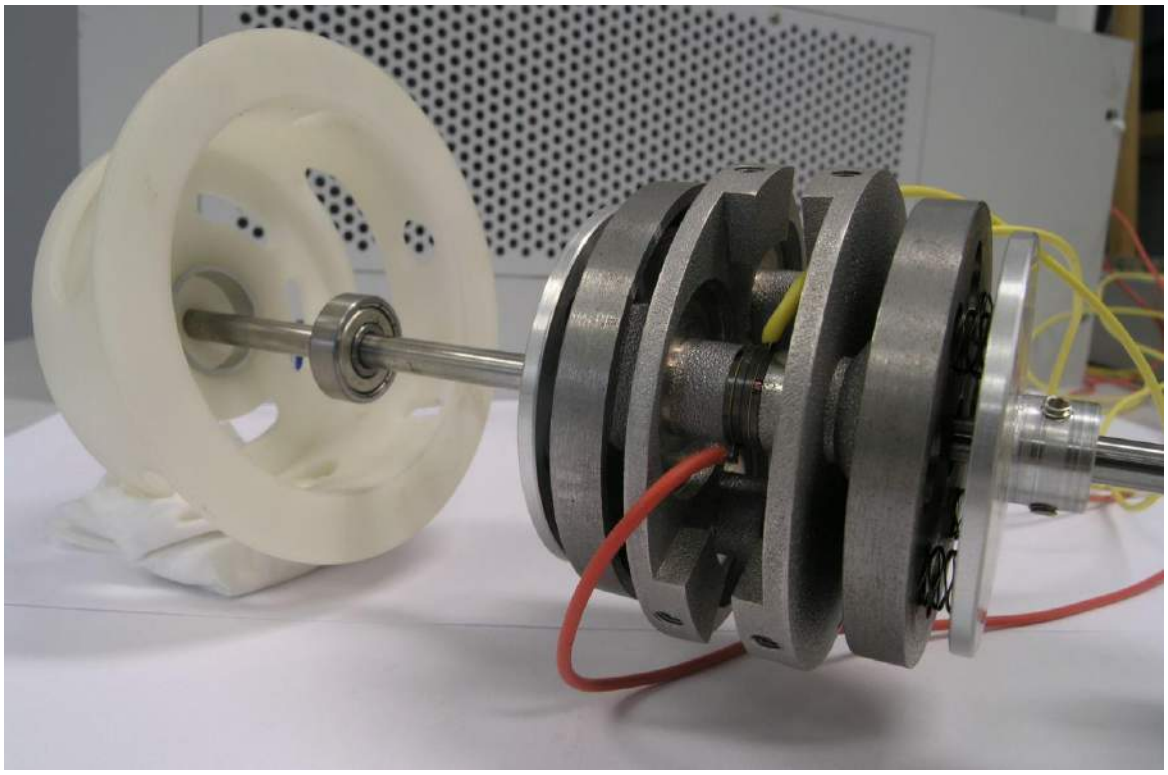

Fig. 6.27 The assembled parts of the prototype multicell piezoelectric motor

6.5.1 A CONCEPT OF POWER SUPPLY FOR PIEZO STRUCTURES

Requirements for the power supply of piezoelectric motors are much different comparing them to the electromagnetic motors. It is due to their much higher operating frequencies and the capacitive (or resistive in some cases) load character. Piezoelectric power amplifiers are divided into two groups:

- low frequency (less than one kHz), continuous mode for quasi-static operating,
- high frequency (several kHz) for a resonance band operating.

Due to the specific parameters of the piezoelectric motors a development of a special power supply control is required. For testing the prototype MPM a high frequency power supply system has been used.

A general structure of power supply system for the piezoelectric actuators/motors is presented in Fig. 6.28 (only one phase is shown).

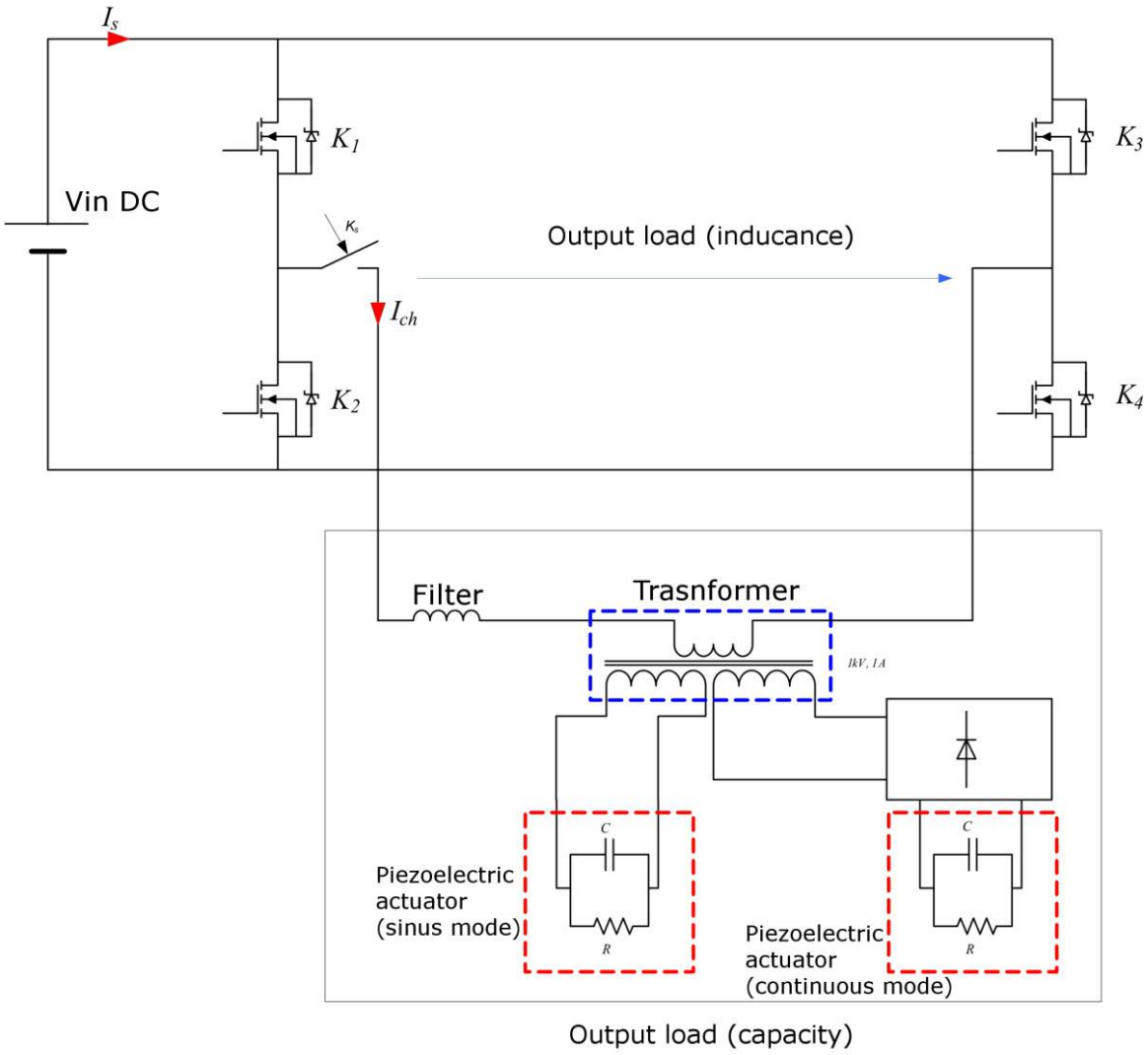

Fig. 6.28 A general structure of power supply system for piezoelectric actuators/motors (only one phase is shown)

6.5.2 A SIMPLIFIED SYSTEM FOR SUPPLY AND MEASUREMENTS

At first, the measurements of the mechanical parameters have been carried using linear amplifier designed to supply the rotating mode motor. The prototype amplifier has been developed in LAPLACE Laboratory (Fig. 6.29). The amplifier has two channels. On each channel there are two high frequency voltage outputs, DC input (max 50V) as a voltage source and input signal generator. This prototype amplifier is based on a resonance inverter which can be connected with a phase loop circuit for efficient controlling the motor.

Fig. 6.29 Linear amplifier power supply for piezoelectric motors - developed in LAPLACE Laboratory (INP-ENSEEIHT, Toulouse)

For the rotating-mode motor, the MOSFET transistors has been used for each phase of the amplifier. The power supply block diagram has been shown in Fig. 6.30. The output channels are supplying the three actuators connected parallel.

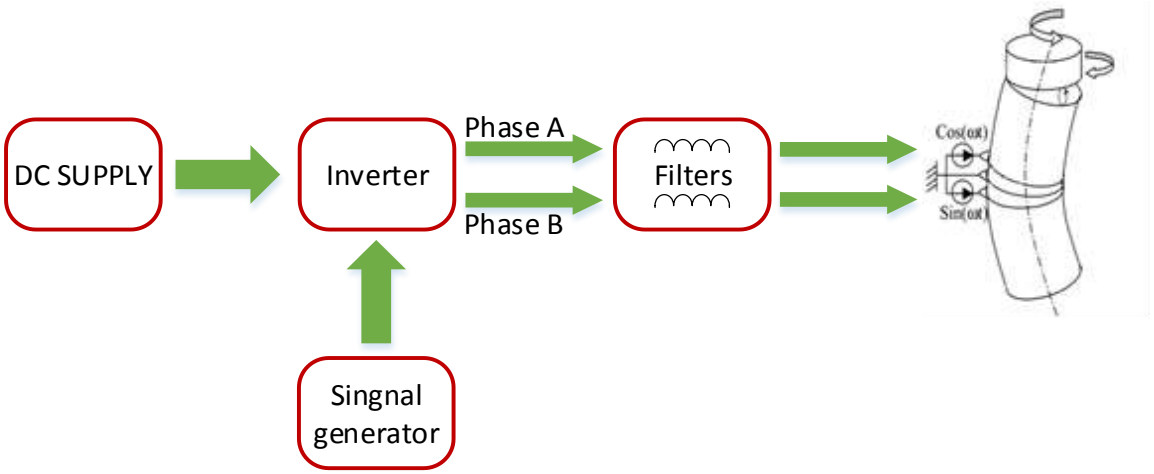

Fig. 6.30 Piezoelectric motor power supply system - block diagram of the laboratory stand

The laboratory stand could generate the maximum output voltage around the 160-170V rms sinusoidal signal with frequency up to several kHz. The two output signals are 90° phase shifted. For the first measurements only one actuator has been supplied. The measured waveforms have been shown in Fig. 6.31, for this case the frequency is 21 kHz.

Afterwards, the three actuators have been connected parallel at the output channels. The measurement results (Fig. 6.32) have shown, that the voltage is more distorted, because the load on the output increased in comparison to first measurement results. The maximum output voltage of the amplifier was limited to 165 V.

The measurements results of the supply current are given in the appendix 4.

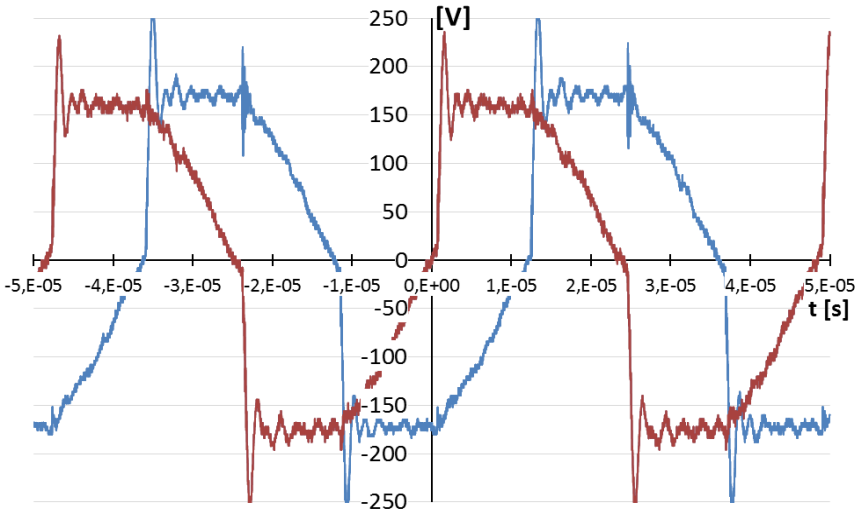

Fig. 6.31 The voltage supply measurements of the single actuator: red color phase A, blue color phase B

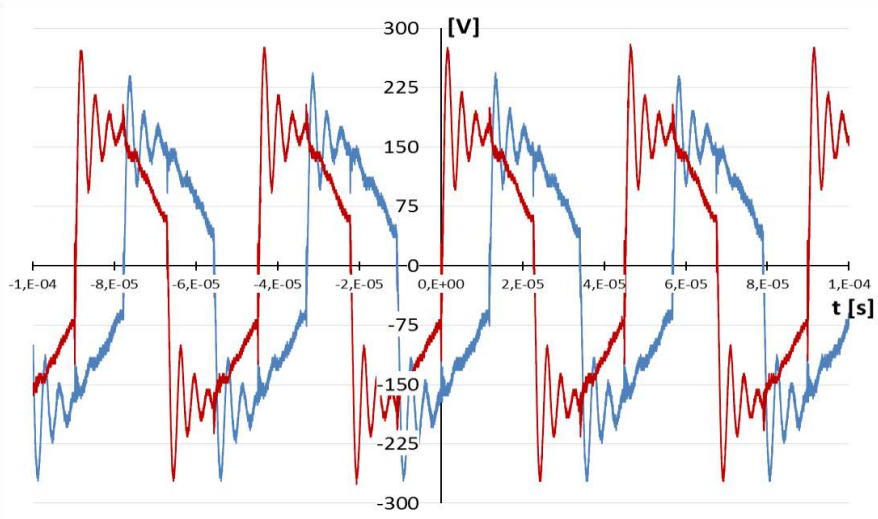

Fig. 6.32 The voltage supply measurements of three actuators connected parallel: red color phase A, blue color phase B

The measured velocity of the prototype MPM has a value 25 rpm. To obtain a better performance characteristics of the prototype MPM the voltage source having higher power (higher output current) is required. The next measurements have been carried out using dSpace laboratory stand.

6.5.3 POWER SUPPLY AND MEASUREMENTS SYSTEM USING DSPACE LABORATORY STAND

The dSpace system is a powerful engineering tool for monitoring, measuring and testing the mechatronics systems It has the following hardware and software parts:

- DS1005 PPC processor,
- PWM control board DS5101,
- conversion board measure DS2004,

- Matlab/Simulink used to control the card and system (Real Time Workshop: RTW),
- compiler for the implement the initial command for the computer,
- tool to design the user interface control system.

The type DS1005 controller, the power converter, and type DS2004 high-speed A/D board have been used. The DS1005 controller has a processor board providing the possibility for real-time monitoring, and also functioning as an interface to the I/O boards and the host PC (Fig. 6.33). The used power supply is based on the voltage fed, resonant, and full-bridge topology.

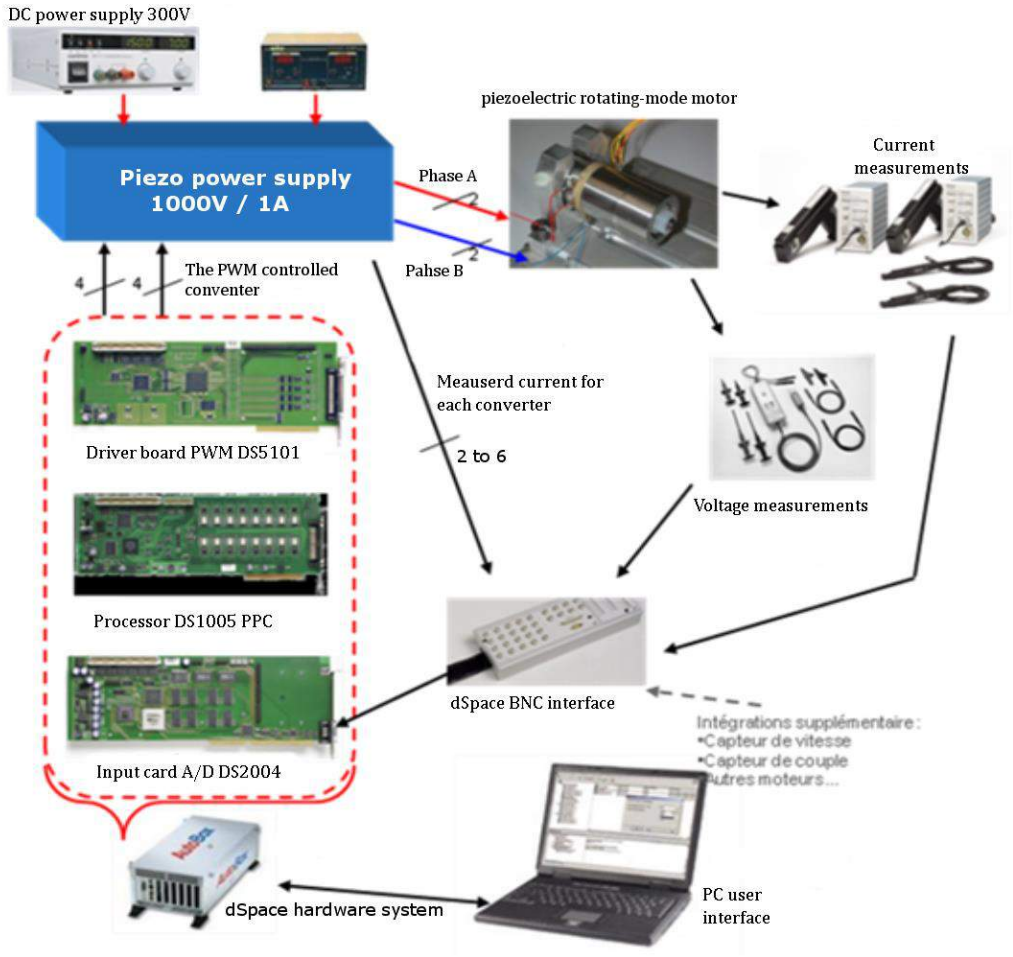

Fig. 6.33 System for power supply and measurements of the prototype MPM using dSpace laboratory stand

Tab. 6.1 Power supply characteristics

	Parameters	Specifications	Observations
Inductive loads	Voltage	0V → 300 V	
	PWM frequency	0 → 200 kHz	PWM
	Minimum time out	25 ns	
	Accuracy	25 ns	
	Maximum current	4 A	
	Power	900W	phase transition
		40W	continuous mode

Capacitive loads	Mode sinusoidal	Output Voltage	0V → 1000 V maximum peak	
		Output current	0 → 1 A maximum sinusoidal peak	
		Power supply loads	Resistance	1kΩ → 100kΩ
			Capacity	1nF → 100nF
		Output frequency	30kHz→ 50kHz	Basic wave
	Mode continuous	Output voltage	1000 VDC	
		Output current	100mA DC	
			1A (maximum)	
		Frequency cycles	100 Hz (maximum)	
		Load	Resistance	10kΩ to 100 kΩ
			Capacity	100nF to 1µF

The dSpace laboratory stand is shown in the Fig. 6.34. Matlab and dSPACE have been used to control the power supply for the prototype MPM. A simple program used to modify the resonance frequency, output amplitude and phase has been developed (Fig. 6.35). The main program blocs have been described in the appendix 5.

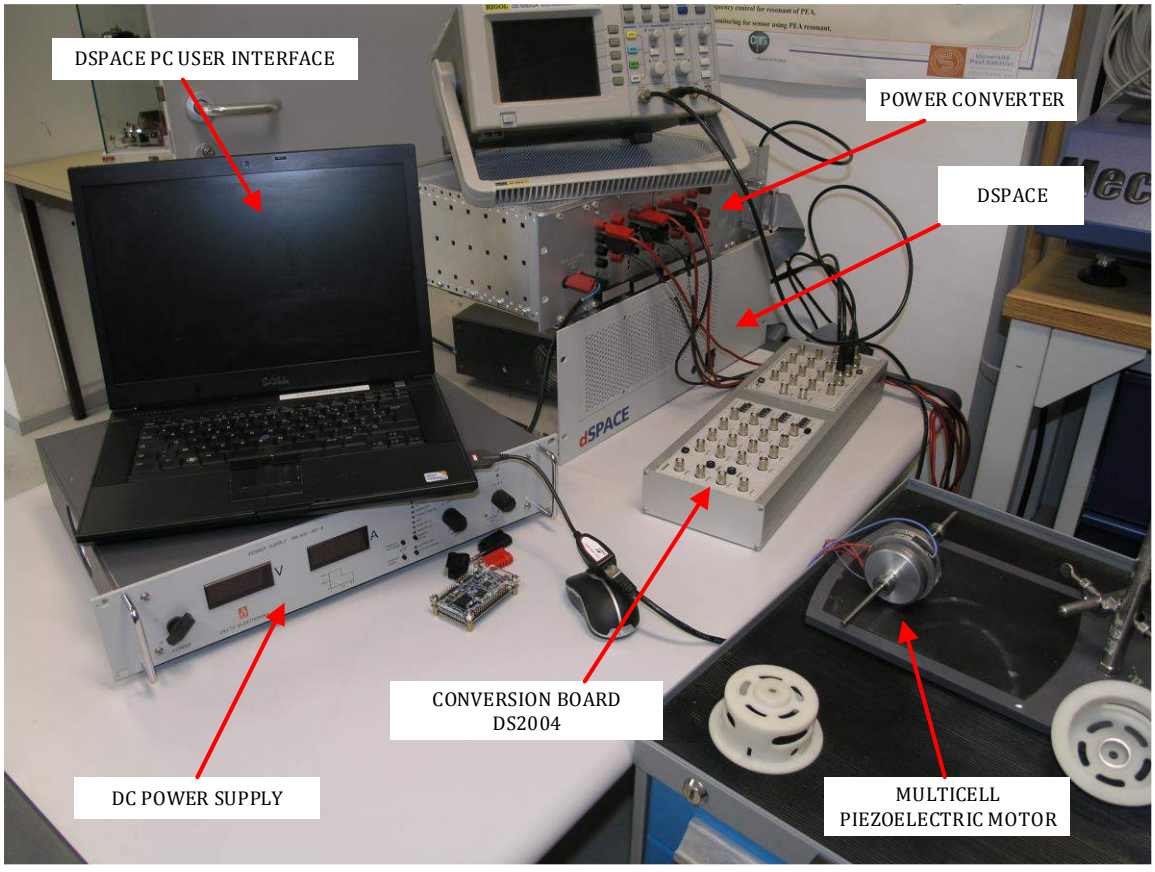

Fig. 6.34 dSpace laboratory stand at the Laboratory LAPLACE (INP-ENSEEIHT, Toulouse) used to test the prototype MPM

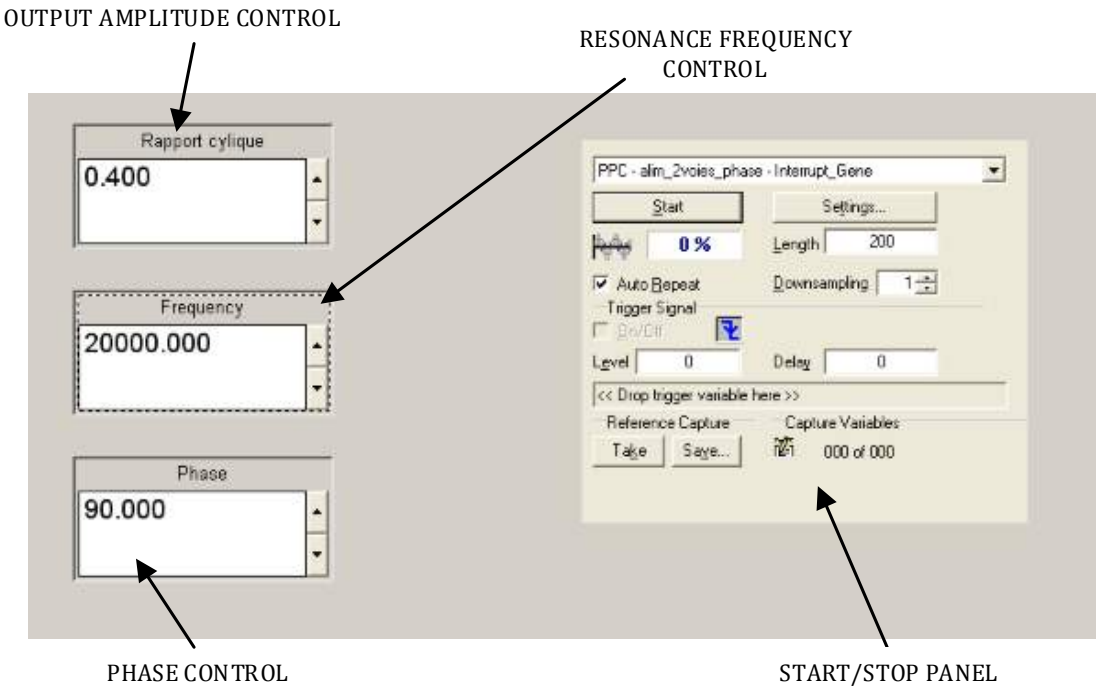

Fig. 6.35 The Matlab – Control Desk interface used to control the power supply parameters

Using this program you can control the output voltage amplitude from 0 to 1000V (Tab. 6.1). For the final measurements, the output voltage amplitude has been set at approx. 400V, i.e., its value was almost twice as high as in the measurements using simplified linear power supply. The results of the torque vs. speed measurements have been presented in Fig. 6.36. The values of the blocking torque and the speed are following:

- blocking torque ≈ 0.4 Nm
- velocity ≈ 46 - 48 rpm.

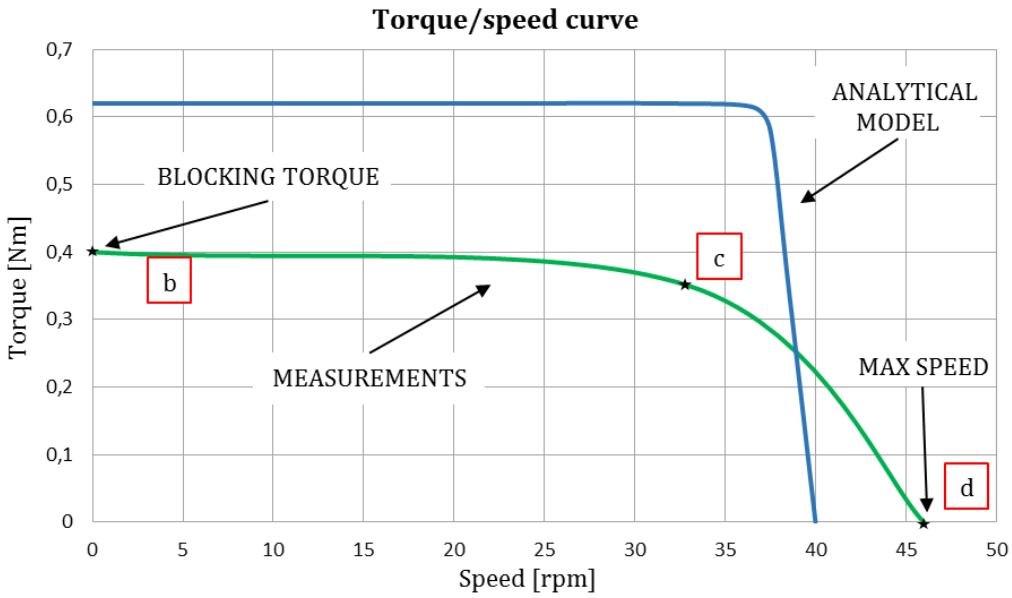

Fig. 6.36 Torque vs. speed characteristic of the prototype MPM: calculated (using analytical model) - blue color, measured - green color

The measurements of the torque vs. speed characteristic (Fig. 6.36) of the prototype MPM have been carried for three points, It can be considered as sufficient, since for the prototype MPM the most important points for this characteristic are following: point referred to the blocking torque, and velocity at no-load as well. In turn, the measured coordinates of the third point "*c*" depend on various factors, e.g., the proper contact adjustment between rotor and stator, the kind of lubrication on the rotor or the rotor driving force. While testing the prototype MPM it has appeared that an interesting issue was the number of the used Smalley springs. The prototype MPM has symmetrical structure and during the measurements four springs on each side have been used. When the number of these springs has been reduced then the velocity has become higher, but torque become lower, and the time response become longer as well. This was due to not properly adjusted rotor - stator contact. On the other hand, the increased number of these springs has caused a higher driving torque, and better performance features of the prototype MPM but the velocity has been decreased. As was mentioned above, the purpose of this effort was to obtain the velocity of the prototype MPM as high as possible, and generating a appropriate torque value (the value has been achieved) as well.

Comparing for the prototype MPM the measured and calculated results, it can be concluded that the calculated results have a satisfactory compliance level with the measured ones. However, it should be pointed out that the obtained compliance level could be higher, if the difference between the calculated (26.2. kHz) and real resonance frequencies (22.0-22.2 kHz) were smaller. Moreover, a properly adjusted rotor - stator contact has also an essential influence on the compliance level.

To explain further the issue of the obtained compliance level for the prototype MPM, the torque vs. speed characteristic of the rotating-mode motor considered in [**6**] has been shown in Fig. 6.37. It can be noticed that for this motor the measured values of the blocking torque and the speed are following: blocking torque ≈ 0.14 Nm, and velocity ≈ 54 rpm.

The highest difference between calculated and measured results for those motor is at the point of maximum velocity. The measured and calculated values of the blocking torque are practically the same.

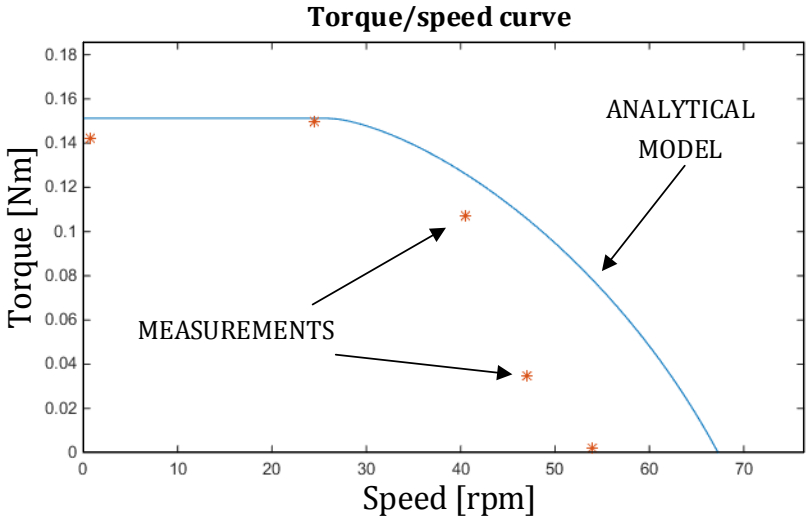

*Fig. 6.37 Torque vs. speed characteristic of the rotating-mode motor described in [**6**]*

It should be noticed that the prototype MPM has lower maximum velocity comparing to the referred rotating-mode motor (47 rpm vs. 54 rpm, respectively), however it has almost three times higher blocking torque (0.4 Nm vs 0.14 Nm, respectively). The results show an advantage of the prototype MPM over the referred rotating-mode motor [**6**].

6.6 CONCLUSIONS

The prototype MPM counter-masses and housing have been made using 3D printer. The input materials to the printer were following: aluminum and nylatron respectively. In turn, the other parts of the prototype MPM have been made on milling machine using steel.

The measured parameters of the prototype MPM are following:

- resonance frequency – 22 kHz,
- displacements at the contact rotor/stator point – 1.1 μm,
- speed– 46 - 48 rpm,
- blocking torque – 0.4 Nm.

Comparing for the prototype MPM the measured (shown above) and calculated results (speed 40 rpm and blocking torque 0.6 Nm), you can conclude that the calculated results have a satisfactory compliance level with the measured ones.

It should be noticed that for the prototype MPM the most important points for the torque vs. speed characteristic are following: point referred to the blocking torque, and velocity at no-load as well.

The prototype MPM testing has shown that an interesting issue is the applied number of the Smalley springs. Reducing the numbers of the springs decreases torque and increases velocity. On the other hand, increasing the number of those springs generates higher driving torque, but the speed is decreasing, and the MPM has better performance features.

7 FINAL CONCLUSIONS

The main scope of the dissertation was following: development a novel concept, implementation and analysis of the multicell piezoelectric motor for the control of the car seat position. The research work has been carried out at the INP-ENSEEIHT-LAPLACE, Toulouse, France, and at the Gdansk University of Technology, Faculty of Electrical and Control Engineering, Department of Power Electronics and Electrical Machines, Gdańsk, Poland.

7.1 RESEARCH RESULTS AND THE DISSERTATION ACHIEVEMENTS

A descriptions of the piezoelectric phenomenon, piezoelectric materials, structures of piezoelectric motors and actuators have been studied in terms of the dissertation scope.

Known structures of the multi piezoelectric motors have been considered in view of their applications for the control of the car seat position.

New concept piezoelectric motor, referred to as "multicell piezoelectric motor" (MPM), has been developed. It is based on a combined topology using the working principles of the traveling wave motor/actuator (known as the Shinsei motor), and the electromechanical structure of the rotating-mode motor/actuator. The electromechanical structure of each rotating-mode motor is considered as an independent one – referred to as a "single cell".

The concept MPM is dedicated to control the position of the car/plane seats. The application of the MPM will reduce the number of gears due to its direct coupling with the driving/movement shaft of the positioning system. The achieved effects of a such integrated structure are following: a higher efficiency, a very low noise of performance, a low cost of manufacturing, and in general a lower pollution of the environment.

Using the equivalent circuit of the Langevin's transducer the analytical model of the MPM has been developed and implemented in the Matlab software. The developed model of the MPM is based on modified analytical model of the rotating-mode motor. The MPM preliminary dimensions and parameters (resonance frequency, velocity, blocking torque, displacement) have been determined using this developed analytical model.

The preliminary dimensions and parameters of the prototype MPM have been verified using its developed virtual (geometrical) model and numerical methods (FEM) implemented in the ANSYS software. Using the FEM model the resonance frequencies and stress values of the prototype MPM have been determined. Their values are following:

- resonance frequency - 25.6 kHz,
- stress – 9 N/mm^2.

Comparing for the prototype MPM the resonance frequency values (determined using the analytical model) (26.2 kHz) and FEM model (25.6 kHz), it should be underlined that the developed analytical model of the MPM can be considered as a relatively highly accurate model.

The maximum stress (9 N/mm^2) can be considered as an acceptable value for the prototype MPM.

The prototype MPM has been manufactured. The MPM counter-masses and housing have been made using 3D printer technology. The input materials to 3D printer were following: aluminum and nylatron, respectively. In turn, the other MPM parts have been made on milling machine using steel. The main measured parameters of the prototype MPM are following:

- resonance frequency – 22 kHz,
- displacements at the contact rotor/stator point – 1.1 μm,
- velocity – 46 - 48 rpm,
- blocking torque – 0.4 Nm.

Comparing the velocity and blocking torque values determined using the MPM analytical model (40 rpm and 0.6 Nm) with their measured values (given above), the results can be assumed as acceptable.

The main contributions of the dissertation:

- development a novel concept of the MPM,
- development analytical model of MPM to determine its mechanical parameters and characteristics,
- virtual design of the MPM and its FEM analysis to determine the resonance frequencies and stress,
- manufacturing the prototype MPM using numerically controlled machines,
- verification of the prototype MPM using dSpace laboratory stand,
- specification of the future research work in view to optimize the prototype MPM.

7.2 FUTURE RESEARCH WORKS

Development an extended analytical model of the MPM for optimization. It seems that as a base of this model the Euler-Lagrange approach can be used

Optimization of the manufactured prototype MPM in terms of its loading limits.

For the MPM optimization in its manufacturing process a less expensive technology should be considered. For the prototype MPM the counter-mass has been manufactured on the milling machine (CNC) using aluminum (Fig. 7.1). The used material is more solid comparing it with the counter-mass manufactured using 3D printer technology. Tthus the mechanical parameter should be improved. The new rotor parts have already been manufactured using the 3D printer (Fig. 7.2). The used material is Nylatron to obtain better friction coefficient and to improve the performance of the prototype MPM. The MPM assembling using the new parts and verification of the resonance frequencies and mechanical characteristic (torque and velocity) should be carried out.

Fig. 7.1 The new counter-mass manufactured on the milling machine (CNC)

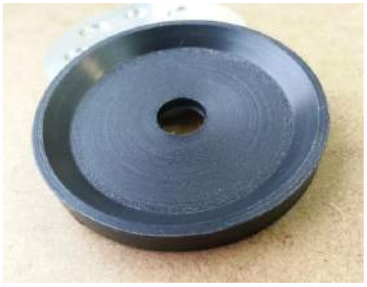

Fig. 7.2 The new rotor manufactured on the 3D printer using Nylatron

Other issue which should be considered is the stator/rotor contact. Extending the contact surface area, should improve mechanical parameter. The application of oil or polymer on the rotor/stator surface, help to obtain the better parameters as well – a higher velocity.

The negative effects of the MPM counter-mass displacements have been noticed. On the layer around the actuator the cracks have appeared. When ceramics are supplied and motor is running, the vibration acting on the actuator causes a small degradation of the material (Fig. 7.3). The part of the counter-mass around the rotating-mode actuator is too thin. One of the solution to eliminate this problem would be extending the diameter of the MPM counter-mass part.

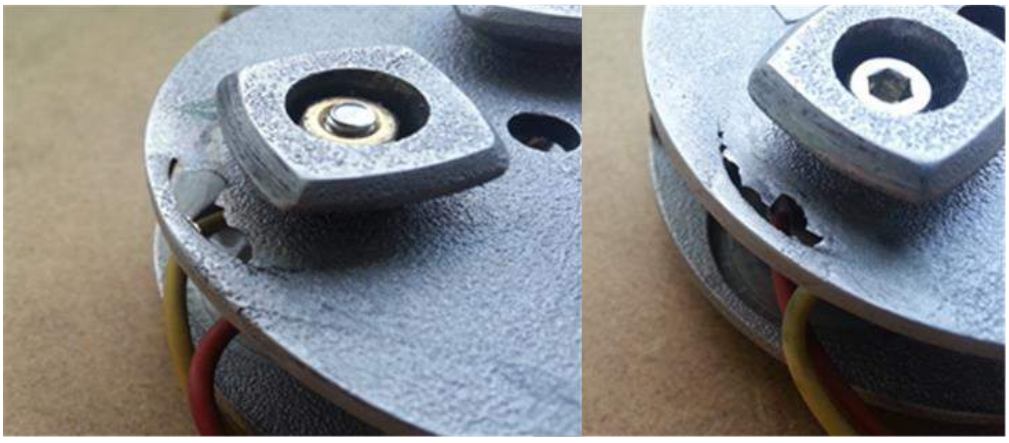

Fig. 7.3 The cracks caused by the vibration on the counter-mass

The final part of the future research work is associated with the optimization of the power supply system for the MPM.

8 BIBLIOGRAPHY

[1] Han A. Adriaens, Willem L. De Koning, and Reinder Banning, "Modeling piezoelectric actuators," *IEEE/ASME Transactions on Mechatronics*, vol. 5, no. 4, pp. 331-341, 2000.

[2] Franz Aepinus, *Memoir concerning some remarkable new electrical experiments*. Berlin: Histoire De L'académie Royale Des Sciences et des Belles Lettres, vol. 12, 1756.

[3] Yoseph Bar-Cohen, X. Bao, and Willem. Grandia, "Rotary ultrasonic motors actuated by traveling flexural waves," *Proc. of SPIE's 6th Annual International Symposium on Smart Structures and Materials*, Newport, 1999.

[4] Robert H. Bishop, *The Mechatronics Handbook*. Austin: The University of Texas, 2002.

[5] Stéphane Bocage, "Conception et mise en oeuvre d'actionneurs piézo-électriques à fréquence de rotation synchronisée," INP - ENSEEIHT, Toulouse, Thesis 1996.

[6] Mark Budinger, "Contribution à la conception et la modélisation d'actionneurs piézoélectriques cylindriques à deux degrés de liberté de type rotation et translation," INPT - ENSEEIHT - LEEI, Toulouse, Thesis 2003.

[7] Matteo Bullo, "Modélisation et commande du moteur piézoélectrique à onde progressive," École Polytechnique Fédérale de Lausanne, Lausanne, Thesis 2005.

[8] Kurt Heinz Jürgen Buschow, *Encyclopedia of materials: science and technology*. Elsevier, 2001.

[9] William D. Callister*, Materials Science and Engineering – An Introduction*. John Wiley and Sons, 2009.

[10] Céline Cénac-Morthé, "Contribution au dimensionnement et à la réalisation d'un moteur piézoélectrique hybride pour application à haut niveau de sécurité," INP - ENSEEIHT - LAPLACE, Toulouse, Thesis 2009.

[11] Hong-Yi Cheng and Jen-Yuan Chang, "A novel piezoelectric rotary motor with cyclic symmetric stator," *Mechatronics and Embedded Systems and Applications (MESA)*, Suzhou, 2012, pp. 1-6.

[12] Jacques Curie and Pierre Curie, *Contractions et dilatations produites par des tensions dans les cristaux hémièdres à faces inclinées*., vol. 93, 1881.

[13] Mirosław Dąbrowski, "Evolution of the theory and applications of ultrasonic motors," *Prace Instytut Elektrotechniki*, no. 12, pp. 33-45, 2001.

[14] Clarence W. De Silva, *Mechatronics: an integrated approach*. CRC Press, 2005.

[15] Akira Endo and Nobutoshi Sasaki, "Investigation of frictional material for ultrasonic motors," *Japanese Journal of Applied Physics*, vol. 26, pp. 197-199, 1987.

[16] A.B. Flatau and K.P. Chong, "Dynamic smart material and structural systems," *Engineering Structures*, pp. 261-270, 2002.

[17] H. Foch, "Éléments constitutifs et synthèse des convertisseurs statiques," Techniques de l'Ingénieur (D3 152), 1989.

[18] Frédéric Galiano, "Conception et mise en oeuvre d'un actionneur piézoélectrique plan à onde stationnaire," INP - ENSEEIHT - LAPLACE, Toulouse, Thesis 2000.

[19] Lauric Garbuio and Jean-Francois Rouchon, "Electroactive lubrication: application to the friction reduction in a thermal engine," *Proc. JFT05*, Tarbes, 2005.

[20] Jacek F. Gieras*, Advancements in electric machines*. Heidelberg: Springer, 2009.

[21] Dariusz Grzybek, "The use of the energy conversion mechanism in the piezoelectric materials into the vibration control," *Technical Transactions*, pp. 51-59, 2011.

[22] M. Hao and W. Chen, "Analysis and Design of a Ring-type Traveling Wave Ultrasonic Motor," *IEEE Proc. International Conference on Mechatronics and Automation*, Luoyang, China, pp. 1806-1810, 2006.

[23] Hiroshi Hirata and Sadayuki Ueha, "Design of a traveling wave type ultrasonic motor," *IEEE Transactions On Ultrasonics, Ferroelectrics, And Frequency Control*, vol. 42, no. 2, pp. 225-231, 1995.

[24] F. Hodar, E. Merlet, and JT. Audren, "Conception et essai d'un moteur piézoélectrique haute puissance," Magelec, Toulouse, pp. 129-137, 2001.

[25] "IEEE Standard on Piezoelectricity," *An American National Standard*. New York, USA: The Institute of Electrical and Electronics Engineers, 1987.

[26] Takuro Ikeda, *Fundamentals of piezoelectricity*. Oxford: Oxford Science Publication, 1990.

[27] J.P. Joule, "On the effects of magnetism upon the dimensions of iron and steel bars," *The London, Edinburgh and Dublin philosophical magazine and journal of science.*, pp. 225-241, 1847.

[28] Shaul Katzir, *The Beginnings of Piezoelectricity: A Study in Mundane Physics.* Springer, 2006.

[29] Andrzej Kołodko, "Beztarciowe silniki piezoelektryczne," *Zeszyty Naukowe Politechniki Gdańskiej. Elektryka 87*, pp. 99-103, 2000.

[30] Marek Krawczuk, Magdalena Palacz, and Żak Arkadiusz, *Materiały o sterowanych właściwościach fizycznych i ich zastosowania*. Gdańsk: Wydawnictwo Politechniki Gdańskiej, 2009.

[31] Kamm. J. Lawrence, *Understanding Electro-Mechanical Engineering: An Introduction to Mechatronics.* Wiley-IEEE Press, 1995.

[32] C. K. Lim and I-M. Chen, "Systematic Design and Prototyping of a Disc-Typed Traveling Wave Ultrasonic Motor," International Conference on Advanced lnteligent Mechatronics. Proceedings of the 2003 IEEE/ASME, pp. 113-118, 2003.

[33] Carl von Linné, *The Flora of Ceylon: consisting of Indian plants of the island of Ceylon*. Sweden, 1747.

[34] Gabriel Lippmann, *Principe de la conservation de l'électricité*. 1881.

[35] Xiao-long Lu, Jun-hui Hu, and Chun-sheng Zhao, "A novel rotary piezoelectric motor for aerospace application," *Proc. Acoustic Waves and Device Applications Symposium,* Shanghai, pp. 41-44, 2012.

[36] Pin Lu, Hong Lee Kwok, Piang Lim Siak, and Zhong Lin Wu, "A kinematic analysis of cylindrical ultrasonic micromotors," *Sensors and Actuators*, vol. 87, issue 3, pp. 194-197, 2001.

[37] Mechanical and Mechatronics Engineering Department, *What is Mechatronics Engineering?* Prospective Student Information. University of Waterloo, 2011.

[38] Godfrey C. Onwubolu, *Mechatronics: principles and applications*, Butterworth-Heinemann, 2005.

[39] M. Mieloszyk, M. Krawczuk, A. Żak, and W. Ostachowicz, "An adaptive wing for a small-aircraft application with a configuration of fibre Bragg grating sensors," *Smart Materials and Structures*, no. 19, 2010.

[40] S.O. Reza Moheimani and Andrew J. Fleming, *Piezoelectric Transducer for Vibration Control and Damping*. Springer, 2006.

[41] Takeshi Morita, Minoru Kurosawa, and Toshiro Higuchi, "An ultrasonic micromotor using a bending cylndrical transducer based on PZT thin film," Sensors and Actuators A50, pp. 75-80, 1995.

[42] Bertrand Nogarede, "Moteurs piézoélectriques," *Techniques de l'Ingenieur (D3 765)*, pp. 1-20, 1996.

[43] Bertrand Nogarede and Dominique Harribey, "De la piézoélectricité aux actionneurs électromécaniques du futur.," INP-Enseeiht-LAPLACE, Le groupe de Recherché en Electrodynamique, 2005.

[44] Bertrand Nogarede, Carol Henaux, and Jean-Francois Rouchon, "Actionneurs électromécaniques pour la robotique et le positionnement," *Techniques de l'Ingenieur* (D53 41), pp. 1-20, 2009.

[45] Bertrand Nogarede, Jean-Francois Rouchon, and Alexis Renotte, "Electroactive materials: towards novel actuation concepts," *Recent Developments of Electrical Drives*, Springer, pp. 435-442, 2004.

[46] Jin-H. Oh et al., "Design and performances of high torque ultrasonic motor for application of automobile," *Proc. J. Electroceram*., vol. 22, pp. 150-155, 2009.

[47] Lionel Petit, Roland Briot, Laurent Lebrun, and Paul Gonnard, "A Piezomotor Using Longitudinal Actuators," *IEEE Transactions on Ultrasonics, Ferroelectrics and Frequency Control,* Vol. 45 No. 2, pp. 277-284, 1998.

[48] Lionel Petit and Paul Gonnard, "A multilayer TWILA ultrasonic motor," *Sensors and Actuators,* vol. I, no. 149, pp. 113–119, 2009.

[49] Lionel Petit and Paul Gonnard, "Industrial design of a centimetric “TWILA” ultrasonic motor," *Sensors and Actuators*, no. 120, pp. 211–224, 2005.

[50] Lionel Petit, P. Gonnard, and B. Grehant, "A piezomotor for the small actuator market," *Applications of Ferroelectrics, Proc. of the 2000 12th IEEE International Symposium*, vol. 1, pp. 33-36, 2000.

[51] Framework Programme, "Materials Innovation for Industry and Society – WING," Bonn, 2003.

[52] J.N. Reddy, *An Introduction to the Finite Element Method (Third ed.).* McGraw-Hill, 2005.

[53] Jean-Francois Rouchon, *Cours Mécatronique*, 2010.

[54] Jean-Francois Rouchon, Céline Cénac-Morthé, and L Garbuio, "Control of friction forces with stationary wave piezoelectric actuator," *Journal of Vibroengineering*, pp. 131-135, Oct. 2008.

[55] Jean-Francois Rouchon and P Jacob, "Structure de moteur pas à pas de type chenille," patent number: 2948244, France, 2011.

[56] Roland Ryndzionek, Mieczysław Ronkowski, Michał Michna, and Jean-Francois Rouchon, "Analytical Modelling of the Multicell Piezoelectric Motor Based on Three Resonance Actuators," *Proc. IECON 2014 - 40th Annual Conference of the IEEE, Industrial Electronics Society*, Dallas, 2014.

[57] Roland Ryndzionek, Mieczysław Ronkowski, Michał Michna, Łukasz Sienkiewicz, and Jean-Francois Rouchon, "Design, modelling and analysis of a new type of piezoelectric motor. Multicell piezoelectric motor," *Proc. IECON 2013 - 39th Annual Conference of the IEEE, Industrial Electronics Society*, Vienna, 2013, pp. 3910-3915.

[58] Roland Ryndzionek, Mieczysław Ronkowski, and Jean-Francois Rouchon, "Koncepcja, realizacja i analiza nowego typu silnika piezoelektrycznego o strukturze wielokomórkowej," *Maszyny Elektryczny: Zeszyty Problemowe*, vol. II, no. 100, pp. 77-82, Maj 2013.

[59] Roland Ryndzionek, Łukasz Sienkiewicz, Mieczysław Ronkowski, Wojciech Szłabowicz, and Marek Grzywacz, "Przegląd wybranych topolgii aktuatorów piezoelektrycznych," *Maszyny Elektryczne: Zeszyty Problemowe*, no. 92, pp. 115-120, 2011.

[60] Roland Ryndzionek et al., "Hybrid piezoelectric motor based on electroactive lubrication principle," *Prace Naukowe Instytutu Maszyn, Napędów i Pomiarów Elektrycznych Politechniki Wrocławskiej*, no. 66, pp. 326-331, 2012.

[61] Roland Ryndzionek et al., "Assembling and testing of hybrid piezoelectric motor based on electroactive lubrication principle," Archives of Electrical Engineering, no. 62, pp. 237-250, 2013.

[62] Roland Ryndzionek, Łukasz Sienkiewicz, Wojciech Szłabowicz, Marek Grzywacz, and Mieczysław Ronkowski , "Silniki piezoelektryczne/ultrasoniczne o ruchu prostym i złożonym: Przegląd topologii i metod sterowania," *Wiadomosci Elektrotechniczne*, no. 11, pp. 21-25, 2011.

[63] Jérome Salanson, "Motorisations piézoélectriques à fonctionnement quasirésonnant ou quasistatique: analyse des contraintes d'alimentatation et expérimentation de structures innovantes," INP - ENSEEIHT, Touluse, Thesis 2000.

[64] Anna Sapińska-Wcisło, "Mechatroniczne człony wyrównawcze z zastosowaniem materiałów inteligentnych," Akademia Górniczo-Hutnicza, Kraków, Praca doktorska 2006.

[65] Toshiiku Sashida and Takashi Kenjo, *An introduction to ultrasonic motors*. Oxford: Clarendon Press, 1993.

[66] Wolfgang Schinkoethe and Bastian Keller, "Multi-degree-of-freedom ultrasonic motors using rotation-symmetric piezoelectric vault geometries," *Proc. Innovative Small Drives and Micro-Motor Systems*, Nuremberg, Germany, pp. 51-56, 2013.

[67] Yun-Jui Shieh, Yung Ting, Bing-Kuan Hou, and Chin-Chih Yeh, "High Speed Piezoelectric Motor," *Proc. International Symp Piezoresponse Force Microscopy and Nanoscale Phenomena in Polar Materials*, Aveiro, pp. 1-3, 2012.

[68] John D. Skipper, "Piezoelectric motor," patent number: 5 027 028, USA, 1991.

[69] K. Spanner, "Survey of the various operating principles of ultrasonic piezomotors," *Proc. Actuator 2006, 10th International Conference on New Actuators*, Bremen, pp. 414-421, 2006.

[70] Wojciech Szlabowicz, Jean-Francois Rouchon, and Bertrand Nogarede, "Design and realization of a rotating-mode piezoelectric motor for aeronautic applications.," *Proc. 10th International Conference on New Actuators*, Bremen, Germany, 2006.

[71] Wojciech Szłabowicz, "Alimentation et Commande d'un moteur piézoélectrique à onde progressive avec contrôle du couple de freinage," *Proc. Conférence JCGE*, Montpellier, 2005.

[72] Wojciech Szłabowicz, "Contribution au dimensionnement et a la réealisation d'actionneur piézoeléctrique a rotation de mode fort coupe pour applications aéronautiques," INP-ENSEEIHT-LEEI, Toulouse, Thesis 2006.

[73] K. Uchino, "Piezoelectric actuator renaissance," *Proc. Actuator 2014, the 14th International Conference on New Actuators*, Bremen, pp. 37-48, 2014.

[74] Antonio Arnau Vives, *Piezoelectric Transducers and Applications*. Springer, 2008.

[75] K. Wen, W. Qiu, Y. Hong, and K. Nakamura, "Experimental study and modeling of non-contact piezoelectric rotary motor using giant electrorheological fluid," in ACTUATOR 2014, Bremen, 2014.

[76] Wolfram Wersing, Walter Heywang, and Karl Lubitz, *Piezoelectricity: Evolution and Future of a Technology*.: Springer Series in Materials Science, 2008.

[77] Paweł Zimny, silniki piezoelektryczne – wykłady, 2000.

Websites:

[78] PI ceramic: www.piceramic.com/piezo-technology/fundamentals.html, 2014.

[79] Sinocera: www.sinocera.net, 2014.

[80] Ferroperm Piezoceramics: http://app04.swwwing.net/files/files/Material%20Properties%202011.pdf, 2014.

[81] Shinsei Motors: www.shinsei-motor.com/English/techno/ultrasonic_motor.html, 2014.

[82] CANON Europe: cpn.canon-europe.com/content/education/technical/usmlens_technology, 2014.

[83] Mustang World: www.mustangworld.com/ourpics/fcar/samajmseats.htm, 2014.

[84] Autodesk | 3D Design, Engineering & Entertainment Software: www.autodesk.com, 2014.

[85] Smalley: www.smalley.com, 2014.

[86] H.C. Materials Corporation: www.hcmat.com/d33_Meter.html, 2014.

[87] INITIAL - Development and Production Centre: www.initial.fr, 2014.

[88] KEYSIGHT Technologies: www.keysight.com/en/pd-1000000858%3Aepsg%3Apro-pn-4294A/precision-impedance-analyzer-40-hz-to-110-mhz?cc=PL&lc=eng, 2014.

[89] LAPLACE - Laboratoire Plasma et Conversion d'Energie: www.laplace.univ-tlse.fr, 2014.

[90] Research Unit Department of Power Electronics and Electrical Machines, Gdansk Uniwersity of Technology, Faculty of Electrical and Control Enginiering : http://eia.pg.edu.pl/kelime, 2014.

[91] Erasmus Gdansk Uniwersity of Technology : http://pg.edu.pl/international/o-programie, 2014

[92] Advanced PhD - The Center for Advanced Studies - the development of interdisciplinary doctoral studies at the Gdansk University of Technology in the key areas of the Europe 2020 Strategy - http://advancedphd.pg.gda.pl/en, 2014

APPENDIX 1

Preliminary dimensioning and analytical calculation of MPM in Matlab

1. ROTAMOD – ROTATING-MODE MOTOR

```
function rotamod(f1,f2,Fpres,U0w)
% ----------------------------------------------------------------
% Admittance et caracteristique mecanique d'un transducteur
% piezoelectrique de type  moteur a rotation de mode
% function : [Y,f]=rotamod2(f1,f2,Fpres,U0w)
%
% ----------------------------------------------------------------
% Le but est de  :
% - trouver la matrice de transfert 4*4 de l'ensemble du  transducteur
% - en deduire la frequence de resonance, la relation lineaire  liant u et psi a la resonance. Le gain vibratoir entre les ceramique et la contre-masse
% - Trouver le schema equivalent de Mason de la partie dynamique a partir des composantes de la matrice 4*4
% - Trouver le facter d'effort equivalent a partir du facteur d'effort des ceramaques et du gain vibratoire
% - en deduire l'admittance a vide
% - A partir de U0w -> Psi0 calcul C(vitesse)
%  - pour Cmax on trouve le rendement, M2, et V
%
% R : resistance de charge
% f1 et f2 : gamme de frequence
% Fpres : Force de pression applique sur le rotor
% U0w : vitesse vibratoire tangentielle
%
% Le transducteur est constitué de deux phases
%
```

```
% Positions des elements dans le moteur :
%                                          _______
%                                         !       |
%                                         !_      |
%                                 --------|       |
%                                 !       ! |     |
%   ---------  ----   ---- ----------      ! |     |
%   !      ! !  ! !  ! !       !       ! |     |
%   ! CM1 ! !P1! !P2! !  CM11 !CM12! | rotor |
%   !      ! !  ! !  ! !       !       ! |     |
%   ---------  ----  ---- ----------!     ! |     |
%                                 !       ! |     |
%                                 --------|       |
% --------------------
% Definition du stator
% --------------------

Fpres=125;

% Parametres geométriques du stator
ria=2e-3;                               % rayon interieur acier
ri=2.5e-3;                              % rayon interieur ceramique
re=6.25e-3;                             % rayon exterieur
re2=8.50e-3;
L_cm11=9e-3;                            % longueur d'une contre-masse
L_cm12=6e-3;
L_cr=0.5e-3;                            % longueur d'une ceramique
L_el=0.1e-3;                            % longueur des electrodes
N=2;                                    % Nombre de ceramiques par phase

c=1e-3;                                 % largeur du contact
```

```
% Parametres mécaniques de la contre-masse, Alum
Qm=200;
C_cm=67e9;                  % module d'Young de l'Alum
p_cm=.346;                  % coef de poisson
G_cm=C_cm/2/(1+p_cm);% module de Coulomb
Ro_cm=3000;                 % densite

% Parametres mécaniques du rotor
C_ro=210e9;
p_ro=.3;                    % coef de poisson
G_ro=C_ro/2/(1+p_ro);           % module de Coulomb
Ro_ro=7800;                 % densite

% Parametres mécaniques des electrodes
C_el=140e9;                 % module d'Young de l'Acier
p_el=.3;                    % coef de poisson
G_el=C_el/2/(1+p_el);% module de Coulomb
Ro_el=7500;                 % densite

% Paramčtres electromécaniques des ceramiques

Qm=23;
e=12.4;                         % constante piezo
Ep_s=8.85e-12*1000;             % constante dielectrique
C_cr=(11.26e10+e^2/Ep_s)*(1+j/Qm);      % Compliance a D constant de la ceramique
p_cr=0.34;
G_cr=C_cr/2/(1+p_cr);   % module de Coulomb
Ro_cr=7650;                     % densite

% Paramčtres electromécaniques des ceramiques P1 89
%e=12.79;                       % constante piezo
```

```
%Ep_s=8.85e-12*668;                % constante dielectrique
%C_cr=13.74e10+e^2/Ep_s;           % Compliance a D constant de la ceramique
%p_cr=0.3;
%G_cr=C_cr/2/(1+p_cr);             % module de Coulomb
%Ro_cr=7650;                       % densite


% Coefficient de frottement
mu=0.21;

% charge lineique
Ln=Fpres/c;

% module d'Young equivalent au contact
E=1/((1-real(p_ro)^2)/real(C_ro)+(1-real(p_cm)^2)/real(C_cm));

% ----------------------
% Calcul de l'admittance
% ----------------------

f1=20000;
f2=30000;

% Gamme des frequences etudiees
f=[f1:(f2-f1)/300:f2];
f = linspace(f1,f2,300);

% Plage de frequences
for i=1:size(f,2);

  w=2*pi*f(i);
```

```
 % Matrice de transfert d'une contre-masse
  T_cm1=matrix44(ria,re,Ro_cm,C_cm,G_cm,L_cm11,w);
  T_cm2=matrix44(ria,re2,Ro_cm,C_cm,G_cm,L_cm12,w);
  T_cm=(T_cm1*T_cm2)^1.28;
  % Matrice de transfert d'une ceramique
  T_cr=matrix44(ri,re,Ro_cr,C_cr,G_cr,L_cr,w);

  % Matrice total
  M=T_cm*T_cr^(2*N)*T_cm;

  % Relation U/psi
  UPs(i)=-M(3,2)/M(3,4);

  % Resonance
  R(i)=abs(M(3,4)*M(1,2)-M(1,4)*M(3,2));

  % Calcul des impedences equivalentes
  B(i)=1/(j*w)/(M(2,1)-M(2,4)*M(3,1)/M(3,4));
  A(i)=(M(1,1)-M(1,4)*M(3,1)/M(3,4)-1)*B(i);

end

% ---------------------------------------
% Calcul de w0 et de l'admittance a vide
% ---------------------------------------

% frequence de resonance
[r,I0]=min(R);
f0=f(I0);
w0=2*pi*f0;

% rapport U/psi
```

```
UPsi=UPs(I0)

% gain vibratoire
T1=matrix44(ria,re,Ro_cm,C_cm,G_cm,L_cm11,w0);  % Matrice de transfert d'une contre-masse
T2=matrix44(ria,re2,Ro_cm,C_cm,G_cm,L_cm12,w0);
T=(T1*T2);
G=1/abs(T(2,2)+T(2,4)*UPsi)

% Facteur d'effort ceramique seule
Ip=4/3*((re-1e-3)^3-(ri+1e-3)^3);
%Ip=4/3*(re^3-ri^3);
Ncer=e/L_cr/N*Ip

% Facteur d'effort pondere
%Ne=Ncer/G*N*2;
Ne=Ncer/G*N/2;

% Capacité bloquee et de depolarisation
Aire=pi*(re^2-ri^2)*N;
I=pi/4*(re2^4-ri^4);

C0=(Ep_s*Aire/L_cr)*N;
%C0=Ep_s*Aire/L_cr*N*2;
Cd=Ep_s*Ip^2/I/L_cr*N*2;

% Admittance a vide
Zeq=(B+A/2)./Ne^2;
Zm=Zeq;
%Zm=-1./(j*Cd*2*pi*f)+Zeq;
Zb=1./(j*C0*2*pi*f);

Y=1./Zb+1./Zm;
```

```
% Affichage admittance
figure(1);
subplot(2,2,1);
plot(f/1000,abs(Y)*1000);
ylabel('Admittance (mS)');
xlabel('Frequency (kHz)');
title('Admittance ');

s1=sprintf('%1.1f kHz\n',f0/1000);
text(f0/1000,abs(Y(I0))*1000,s1);

% --------------------
% Contact stator/rotor
% --------------------
U0w=0.155;
rer=22e-3;

% Rayon du cylindre equivalent
U0=U0w/w0;                    % vibration radiale
Psi0=U0/abs(UPsi);   % deformee angulaire en bout de contre-masse
Req=rer/Psi0;

% largeur et profil du contact
a=2*sqrt(Ln*Req/pi/E)*0.25; % demi-largeur du contact
P0=2*Ln/pi/a;            % pression max an niveau du contact

% affichage du contact
figure(1);
subplot(2,2,2);
x=[-a:2*a/100:a];
plot(x/(2*pi*re)*360,P0*sqrt(1-(x/a).^2)/1e6);
```

```
axis([-180 180 0 P0*1.1/1e6]);
s2b=sprintf(' Stator/Rotor contact\n( Vibrations : %4.2f (axial) * %4.2f (radial) um - Effort : %5.2f N )',...
  Psi0*re*1e6,U0*1e6,Fpres);
title(s2b);
ylabel('Pression (MPa)');
xlabel('Angular position  (°)');
s2=sprintf('Contact length: %3.0f °', 2*a/(2*pi*re)*360);
text(-80,P0*.1/1e6,s2);

% ------------------------------
% Caracteristiques couple/vitesse
% ------------------------------

% Couple bloque
%Cm1=pi/2*mu*a*c*re*P0;
Cm=pi/2*mu*a*c*rer*P0;
%Cm=Cm1+Cm2;
% Vitesse limite
Vlim=U0w*cos(a/re)/rer;

% Puissance nominale
Pnom=Cm*Vlim;

% Essai sur proto
load c_55v.txt -ascii;
load v_55v.txt -ascii;

% calcul et affichage de la caracteristique
%b=[0:pi*re/2/100:pi*re/2];
%C1=2*mu*a*c*re*P0*(asin(b/a)+b/a.*sqrt(1-(b/a).^2)-pi/4);
%C=2*mu*a*c*re2*P0*(asin(b/a)+b/a.*sqrt(1-(b/a).^2)-pi/4);
```

```
%C=C1+C2;

b=[0:pi*re/2/100:pi*re/2];
C1=2*mu*a*c*rer*P0*(asin(b/a)+b/a.*sqrt(1-(b/a).^2)-pi/4);
C=C1;
figure(1);
subplot(2,2,3);
plot(U0w*cos(b/re)*60/2/pi/rer,real(C),v_55v,c_55v,'*');
%plot(U0w*cos(b/re)*60/2/pi/re,real(C),v_55v,c_55v,'*');
title('Torque/Speed curve');
xlabel('Speed (rpm)');
ylabel('Torque (Nm)');
axis([0 U0w*60/2/pi/rer 0 Cm*1.25]);

% ----------------------------------
% Calcul de la tension d'alimentation
% ----------------------------------

% Couple (V,I) au niveau du contact pour Cmax
Et=mu*c*abs(UPsi)*P0*pi/a/((pi/2/a)^2-1/rer^2); % fcem mouvement tangentiel
Er=mu*c*abs(UPsi)*P0*2*a*(a/rer-pi/2*sin(a/rer))/(-(pi/2)^2+(a/rer)^2); % fcem mouvement radial
Vi=Et+Er+A(I0)*Psi0*w0;
Vt=Vi+B(I0)*(Psi0*w0+Vi/A(I0));
V=((Vt)/Ne);

s3=sprintf('Puissance contact : %5.2f W\n',real((Et+Er)*Psi0*w0));
s3=sprintf('Facteur d ellipse : %5.3f\n',UPsi/re);
s4=sprintf('Machine power : %5.2f W\n', real(Vt*(Psi0*w0+Vi/A(I0))'));
s5=sprintf('Efficiency : %5.1f %%\n', 100*Pnom/real(Vt*(Psi0*w0+Vi/A(I0))'));
s6=sprintf('Amplification : %5.1f\n',G);
s7=sprintf('Facteur effort : %5.5f N.m/V\n',Ne);
```

```
s8=sprintf('Power supply : %5.1f V\n',V);
s9=sprintf('Torque max in sigle actuator: %5.1f V\n',Cm);

%text(Vlim*.5,Cm*0.5,[s3 s4 s5 s6 s8 s9]);

% ---------------------------------------
% Calcul des contraintes et des deformees
% ---------------------------------------

Xcer=T*[0 U0*UPsi 0 U0].';

x=[-(L_cm11+L_cm12+L_cr*N) -L_cr*N L_cr*N (L_cm11+L_cm12+L_cr*N)]
V=[ 0 Xcer(1) Xcer(1) 0];

I=pi/4*(re2^4-ri^4);

figure(1);
subplot(2,2,4);
plot(x*1000,abs(V)*re/I/1e6);
title('Stress simulation');
xlabel('Position (mm)');
ylabel('(MPa)');

% Affichage des déformees

s9=sprintf('%5.3f um ',Psi0*re*1e6);
text((L_cm11+N*L_cr)*1000,abs(V(1))*re/I/1e6,s9);

s10=sprintf('%5.3f um ',Psi0*re*1e6/G);
text(0,abs(V(2))*re/I/1e6,s10);
```

2. RESON – MATRIX44

```
function [M44]=matrix44(ri,re,Ro,c,G,L,w)
% ------------------------------------------------------------
% Calcule la matrice de transfert 4*4 d'un cylindre e
% a la pulsation w avec :
%  - ri, le rayon interne
%  - re, le rayon externe
%  - Ro, la densite
%  - C, la constante elastique (le module d'Young)
%  - G, mode de Coulomb (cisaillement)
%  - L, la longueur
% ------------------------------------------------------------

re=6.25e-3;
ri=2.5e-3;
Ro=7800;
c=1e-3;
C_cm=69e9;                  % module d'Young de l'Alum
p_cm=.38;                   % coef de poisson
G=C_cm/2/(1+p_cm)
L=20e-3;
f=25000;
w=2*3.1415*f;

% Calcul de I
I=pi/4*(re^4-ri^4);

% Calcul de la section A
A=pi*(re^2-ri^2);

% Coef cisaillement
a=3/4*(re^2+ri^2)*(re-ri)/(re^3-ri^3);
```

```
% Calcul des coef. des fonctions caracteristiques
delta=(Ro*I*(1+c/a/G))^2*w^4+4*c*I*(Ro*A*w^2-Ro^2*I*w^4/a/G);
k1=sqrt((sqrt(delta)+Ro*I*(1+c/a/G)*w^2)/2/c/I);
k2=sqrt((sqrt(delta)-Ro*I*(1+c/a/G)*w^2)/2/c/I);
Ac=c*I*(Ro*w^2/a/G-k1^2);
Bc=c*I*(Ro*w^2/a/G+k2^2);
Ap=k1*(a*A*G+Ac)/(a*A*G-Ro*I*w^2);
Bp=k2*(a*A*G+Bc)/(a*A*G-Ro*I*w^2);
At=a*A*G*(Ap-k1);
Bt=a*A*G*(Bp-k2);

% Calcul de la matrice de transfert  4*4
M2=[
  Ac*sin(k1*L/2), Ac*cos(k1*L/2), Bc*sinh(k2*L/2), Bc*cosh(k2*L/2)
  Ap*cos(k1*L/2), -Ap*sin(k1*L/2), Bp*cosh(k2*L/2), Bp*sinh(k2*L/2)
  At*cos(k1*L/2), -At*sin(k1*L/2), Bt*cosh(k2*L/2), Bt*sinh(k2*L/2)
  sin(k1*L/2), cos(k1*L/2), sinh(k2*L/2), cosh(k2*L/2)
];
M1=[
  Ac*sin(-k1*L/2), Ac*cos(-k1*L/2), Bc*sinh(-k2*L/2), Bc*cosh(-k2*L/2)
  Ap*cos(-k1*L/2), -Ap*sin(-k1*L/2), Bp*cosh(-k2*L/2), Bp*sinh(-k2*L/2)
  At*cos(-k1*L/2), -At*sin(-k1*L/2), Bt*cosh(-k2*L/2), Bt*sinh(-k2*L/2)
  sin(-k1*L/2), cos(-k1*L/2), sinh(-k2*L/2), cosh(-k2*L/2)
];

M44=M2*inv(M1);
```

APPENDIX 2

Ansys script for static simulation of ceramic and stator

1. PIEZOELECTRIC CERAMICS SIMULATION

```
! Definition des materiaux pour TER
! ---------------------------------

/PREP7
! Type d'elements
ET,1,SOLID98,0                          ! 3-D COUPLED-FIELD SOLID

! Definition des materiaux
! ------------------------
! Acier des contre-masses
! -----------------------
MP,EX,1,210E9                                ! ACIER : MODULUS OF ELASTICITY
MP,NUXY,1,.3                            ! ACIER : POISSON RATIO
MP,DENS,1,7700                          ! ACIER : DENSITY
!
! Ceramique polarise dans sens negatif
! ------------------------------------
MP,DENS,2,7400                          ! PC5H : DENSITY
TB,PIEZ,2
! DEFINE PIEZO. TABLE
! PIEZO MATRIX CONSTANTS
TBDATA,3,-4.9                           ! e31
TBDATA,6,-4.9                           ! e31
TBDATA,9,-21.4                          ! e33 , Signe - pour sens de polarisation
TBDATA,14,17.1                          ! e15
TBDATA,16,17.1                          ! e15
! PERMITTIVITY
MP,PERX,2,1820                          ! Eps_s_11
```

```
MP,PERY,2,1820                          ! Eps_s_11
MP,PERZ,2,1461                          ! Eps_s_33
! DEFINE STRUCTURAL TABLE FOR PC5H
TB,ANEL,2
! INPUT [C] MATRIX FOR PC5H
TBDATA,1,12.09E10,7.63E10,7.31E10               ! Ce11,Ce12,Ce13
TBDATA,7,12.09E10,7.31E10               ! Ce11,Ce13
TBDATA,12,11.26E10                      ! Ce33
TBDATA,16,2.23E10                       ! Ce66, attention inversion
TBDATA,19,3.36E10                       ! Ce44
TBDATA,21,3.36E10                       ! Ce44
!
! Ceramique polarise dans sens positif
! ------------------------------------
MP,DENS,3,7400                          ! PC5H : DENSITY
TB,PIEZ,3                               ! DEFINE PIEZO. TABLE
! PIEZO MATRIX CONSTANTS
TBDATA,3,-4.9                           ! e31
TBDATA,6,-4.9                           ! e31
TBDATA,9,+21.4                          ! e33, Signe + pour sens de polarisation
TBDATA,14,17.1                          ! e15
TBDATA,16,17.1                          ! e15
! PERMITTIVITY
MP,PERX,3,1820                          ! Eps_s_11
MP,PERY,3,1820                          ! Eps_s_11
MP,PERZ,3,1461                          ! Eps_s_33
! DEFINE STRUCTURAL TABLE FOR PC5H
TB,ANEL,3
! INPUT [C] MATRIX FOR PC5H
TBDATA,1,12.09E10,7.63E10,7.31E10               ! Ce11,Ce12,Ce13
TBDATA,7,12.09E10,7.31E10               ! Ce11,Ce13
TBDATA,12,11.26E10                      ! Ce33
TBDATA,16,2.23E10                       ! Ce66, attention inversion
TBDATA,19,3.36E10                       ! Ce44
TBDATA,21,3.36E10                       ! Ce44
!
! Creation des cylindres
```

```
CYLIND,6.25e-3,2e-3,0,0.5e-3,0,180,
CYLIND,6.25e-3,2e-3,0,0.5e-3,180,360,
!
!!!!!!!!!!!!!!!!!!!!!!!!!
!!!!!!!!!!!!!!!!!!!!!!!!!
!!GLUE OPTION!!!!
!!!!!!!!!!!!!!!!!!!!!!!!!
!!!!!!!!!!!!!!!!!!!!!!!!!
FLST,2,2,6,ORDE,2
FITEM,2,1
FITEM,2,2
VGLUE,P51X
!
!Association des materiau aux differents volumes
!!!!!!!!!!!!!!!!!!!!!!!!!!!!!!!
!!!!!!!MATERIAL 2!!!!!!!
!!!!!!!!!!!!!!!!!!!!!!!!!!!!!!!
!
CM,_Y,VOLU
VSEL, , , ,      1
CM,_Y1,VOLU
CMSEL,S,_Y
!*
CMSEL,S,_Y1
VATT,      2, ,   1,      0
CMSEL,S,_Y
CMDELE,_Y
CMDELE,_Y1
!*
!!!!!!!!!!!!!!!!!!!!!!!!!!!!!
!!!!!MATERIAL 3!!!!!!
!!!!!!!!!!!!!!!!!!!!!!!!!!!!!
!
CM,_Y,VOLU
VSEL, , , ,      3
CM,_Y1,VOLU
CMSEL,S,_Y
```

```
!*
CMSEL,S,_Y1
VATT,      3, ,   1,      0
CMSEL,S,_Y
CMDELE,_Y
CMDELE,_Y1
!*
!!!!
!Definition du maillage
MSHAPE,1,3D
MSHKEY,0
!*
FLST,5,2,6,ORDE,2
FITEM,5,1
FITEM,5,3
CM,_Y,VOLU
VSEL, , , ,P51X
CM,_Y1,VOLU
CHKMSH,'VOLU'
CMSEL,S,_Y
!*
VMESH,_Y1
!*
CMDELE,_Y
CMDELE,_Y1
CMDELE,_Y2
!*
!
!!!!!!!!!!!!!!!!!!!!!!
!!!Displacement!!!
!!!!!!!!!!!!!!!!!!!!!!
CM,_Y,NODE
NSEL, , , ,P51X
CM,_Y1,NODE
CMSEL,S,_Y
CMDELE,_Y
!*
```

```
!*
FLST,2,2,5,ORDE,2
FITEM,2,5
FITEM,2,-6
!*
/GO
DA,P51X,ALL,0
!
!!!!!!!!!!!!!!!!!!!!
!!!!VOLTAGE!!!!
!!!!!!!!!!!!!!!!!!!!
/USER,  1
FLST,2,1,5,ORDE,1
FITEM,2,13
/GO
!*
DA,P51X,VOLT,100
!*
/USER,  1
FLST,2,1,5,ORDE,1
FITEM,2,1
/GO
!*
DA,P51X,VOLT,100
!*
/USER,  1
/REPLO
FLST,2,2,5,ORDE,2
FITEM,2,2
FITEM,2,14
/GO
!*
DA,P51X,VOLT,0
!!!!!!!!!!!!!!!!!!
!!!SYMETR!!!
!!!!!!!!!!!!!!!!!!
!
```

```
FLST,2,2,5,ORDE,2
FITEM,2,5
FITEM,2,-6
DA,P51X,SYMM
!
!!!!!!!!!!!!!!!!!!!!!!!!!!
!!!!!!!!!!!!!!!!!!!!!!!!!!
!!!!SIMULATION!!!!
!!!!!!!!!!!!!!!!!!!!!!!!!!
/SOL
!*
ANTYPE,0
NSUBST,1,1,0
EQSLV,ITER,5
```

2. COUNTER-MASS SIMULATION

```
! Definition des materiaux
! --------------------------------
/PREP7
! Type d'elements
ET,1,SOLID98,0                    ! 3-D COUPLED-FIELD SOLID

! Definition des materiaux
! ------------------------
! Acier des contre-masses
! ------------------------
MP,EX,1,131E9                          ! ACIER : MODULUS OF ELASTICITY
MP,NUXY,1,.285                    ! ACIER : POISSON RATIO
MP,DENS,1,8250                    ! ACIER : DENSITY

! Ceramique polarise dans sens negatif
! -----------------------------------
MP,DENS,2,7400                    ! PC5H : DENSITY
```

```
TB,PIEZ,2                       ! DEFINE PIEZO. TABLE
! PIEZO MATRIX CONSTANTS
TBDATA,3,-4.9                   ! e31
TBDATA,6,-4.9                   ! e31
TBDATA,9,-21.4                  ! e33 , Signe - pour sens de polarisation
TBDATA,14,17.1                  ! e15
TBDATA,16,17.1                  ! e15
! PERMITTIVITY
MP,PERX,2,1820                  ! Eps_s_11
MP,PERY,2,1820                  ! Eps_s_11
MP,PERZ,2,1461                  ! Eps_s_33
! DEFINE STRUCTURAL TABLE FOR PC5H
TB,ANEL,2
! INPUT [C] MATRIX FOR PC5H
TBDATA,1,12.09E10,7.63E10,7.31E10        ! Ce11,Ce12,Ce13
TBDATA,7,12.09E10,7.31E10       ! Ce11,Ce13
TBDATA,12,11.26E10              ! Ce33
TBDATA,16,2.23E10               ! Ce66, attention inversion
TBDATA,19,3.36E10               ! Ce44
TBDATA,21,3.36E10               ! Ce44

! Ceramique polarise dans sens positif
! ------------------------------------
MP,DENS,3,7400                  ! PC5H : DENSITY
TB,PIEZ,3                       ! DEFINE PIEZO. TABLE
! PIEZO MATRIX CONSTANTS
TBDATA,3,-4.9                   ! e31
TBDATA,6,-4.9                   ! e31
TBDATA,9,+21.4                  ! e33, Signe + pour sens de polarisation
TBDATA,14,17.1                  ! e15
TBDATA,16,17.1                  ! e15
! PERMITTIVITY
```

```
MP,PERX,3,1820                  ! Eps_s_11
MP,PERY,3,1820                  ! Eps_s_11
MP,PERZ,3,1461                  ! Eps_s_33
!
! DEFINE STRUCTURAL TABLE FOR PC5H
!
TB,ANEL,3
! INPUT [C] MATRIX FOR PC5H
TBDATA,1,12.09E10,7.63E10,7.31E10       ! Ce11,Ce12,Ce13
TBDATA,7,12.09E10,7.31E10       ! Ce11,Ce13
TBDATA,12,11.26E10              ! Ce66, attention inversion
TBDATA,19,3.36E10               ! Ce44
TBDATA,21,3.36E10               ! Ce44
!
! Creation des ceramics
CYLIND,6.25e-3,2e-3,0,0.5e-3,0,180,
CYLIND,6.25e-3,2e-3,0,0.5e-3,180,360,
CYLIND,6.25e-3,2e-3,0.5e-3,1e-3,0,180,
CYLIND,6.25e-3,2e-3,0.5e-3,1e-3,180,360,
CYLIND,6.25e-3,2e-3,1e-3,1.5e-3,90,270,
CYLIND,6.25e-3,2e-3,1e-3,1.5e-3,-90,90,
CYLIND,6.25e-3,2e-3,1.5e-3,2e-3,90,270,
CYLIND,6.25e-3,2e-3,1.5e-3,2e-3,-90,90,
!!!!!!!!!!!!!!!!!!!!!!!!!!!!!!!!!!!!
! Creation des contremasse!!!
!!!!!!!!!!!!!!!!!!!!!!!!!!!!!!!!!!!!
CYLIND,6.25e-3,2e-3,2e-3,22e-3,0,360,
CYLIND,6.25e-3,2e-3,0,-20e-3,0,360,
!
!!!!!!!!!!!!
!!!!glue!!!
!!!!!!!!!!!!
```

```
FLST,2,10,6,ORDE,2
FITEM,2,1
FITEM,2,-10
VGLUE,P51X
vlist, all
!!!!!!!!!!!!!!!!!!!!!!!!!!!!!!
!!!!!!MATERIALS!!!!!!!!
!!!!!!!!!!!!!!!!!!!!!!!!!!!!!!
!!!!!CONTREMASSE!!!!
!!!!!!!!!!!!!!!!!!!!!!!!!!!!!!
FLST,5,2,6,ORDE,2
FITEM,5,19
FITEM,5,20
CM,_Y,VOLU
VSEL, , , ,P51X
CM,_Y1,VOLU
CMSEL,S,_Y
!*
CM,_Y1,VOLU
CMSEL,S,_Y
!*
CMSEL,S,_Y1
VATT,      1, ,   1,      0
CMSEL,S,_Y
CMDELE,_Y
CMDELE,_Y1
!*
!!!!!!!!!!!!!!!!!!!!!!!!!
!!!CER NEGATIV!!
!!!!!!!!!!!!!!!!!!!!!!!!!
FLST,5,4,6,ORDE,4
FITEM,5,12
```

```
FITEM,5,14
FITEM,5,15
FITEM,5,17
CM,_Y,VOLU
VSEL, , , ,P51X
CM,_Y1,VOLU
CMSEL,S,_Y
!*
CMSEL,S,_Y1
VATT,      2, ,   1,      0
CMSEL,S,_Y
CMDELE,_Y
CMDELE,_Y1
!!!!!!!!!!!!!!!!!!!!!!!!!!!!
!!!CER POSITIV!!!!!!
!!!!!!!!!!!!!!!!!!!!!!!!!!!!
FLST,5,4,6,ORDE,4
FITEM,5,11
FITEM,5,13
FITEM,5,16
FITEM,5,18
CM,_Y,VOLU
VSEL, , , ,P51X
CM,_Y1,VOLU
CMSEL,S,_Y
!*
CMSEL,S,_Y1
VATT,      3, ,   1,      0
CMSEL,S,_Y
CMDELE,_Y
CMDELE,_Y1
!!!!!!!!!!!!!!!!!
```

```
!!!!MESH!!!!
!!!!!!!!!!!!!!!!
MSHAPE,1,3D
MSHKEY,0
!*
FLST,5,10,6,ORDE,2
FITEM,5,11
FITEM,5,-20
CM,_Y,VOLU
VSEL, , , ,P51X
CM,_Y1,VOLU
CHKMSH,'VOLU'
CMSEL,S,_Y
!*
VMESH,_Y1
!*
CMDELE,_Y
CMDELE,_Y1
CMDELE,_Y2
!*
!!!!!!!!!!!!!!!!!!!!!!!
!!!!!!VOLTAGE!!!!
!!!!!!!!!!!!!!!!!!!!!!!
!FLST,2,6,5,ORDE,6
!FITEM,2,55
!FITEM,2,58
!FITEM,2,11
!FITEM,2,25
!FITEM,2,7
!FITEM,2,14
!/GO
!DA,P51X,VOLT,0
```

```
!!!!
!!!!
FLST,2,4,5,ORDE,4
FITEM,2,64
FITEM,2,2
FITEM,2,73
FITEM,2,26
/GO
!*
DA,P51X,VOLT,1000
!!!!
!!!!!!!!!!!!!!!!!!!!
!!!!!ANALYS!!!!
!!!!!!!!!!!!!!!!!!!!
!!!!!
/SOL
!*
ANTYPE,2
!*
!*
MODOPT,LANB,10
EQSLV,SPAR
MXPAND,10, , ,0
LUMPM,0
PSTRES,0
!*
MODOPT,LANB,10,15000,90000, ,OFF
!!!!!!!!!!
```

APPENDIX 3

Technical drawings:

APPENDIX 4

Current measurements:

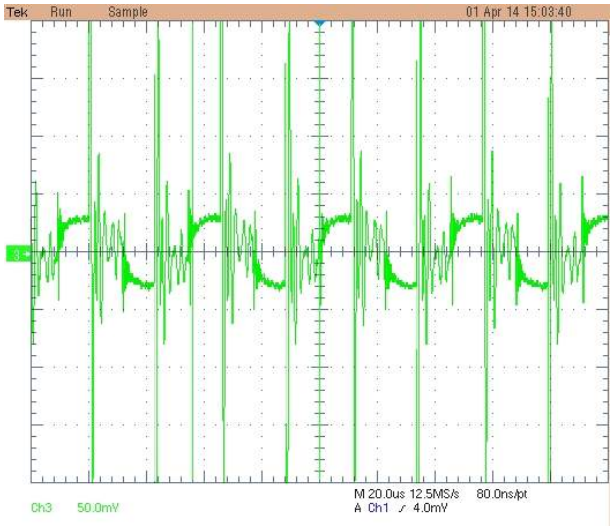

Fig. A.4.1 Current measurements for only one actuator connected

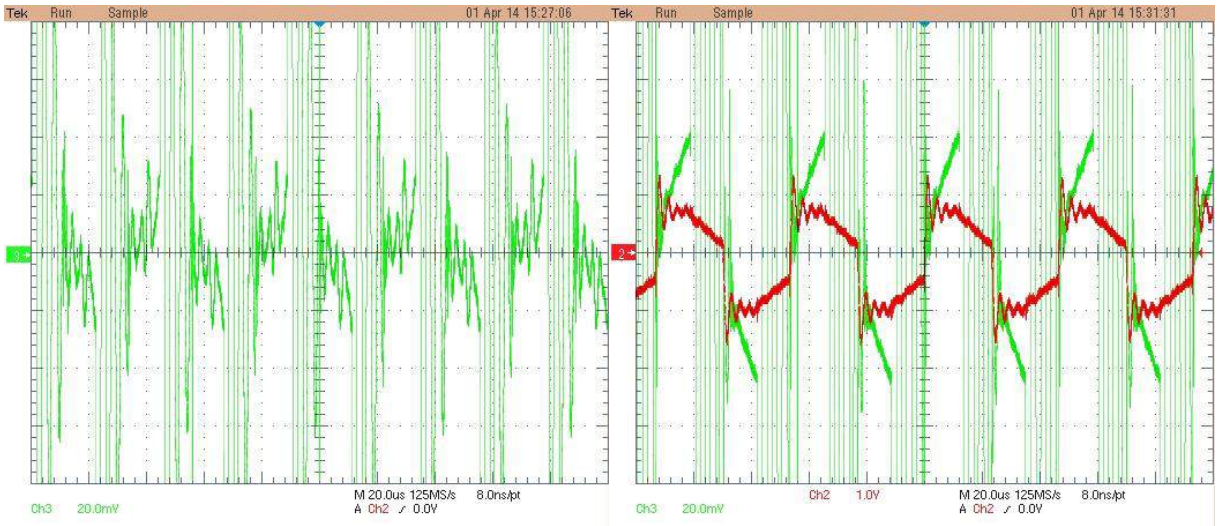

Fig. A.4.2 Current measurements with three actuators connected parallel. Measures for one phases – left, measures for two phases – right

APPENDIX 5

The dSpace control panel program blocks

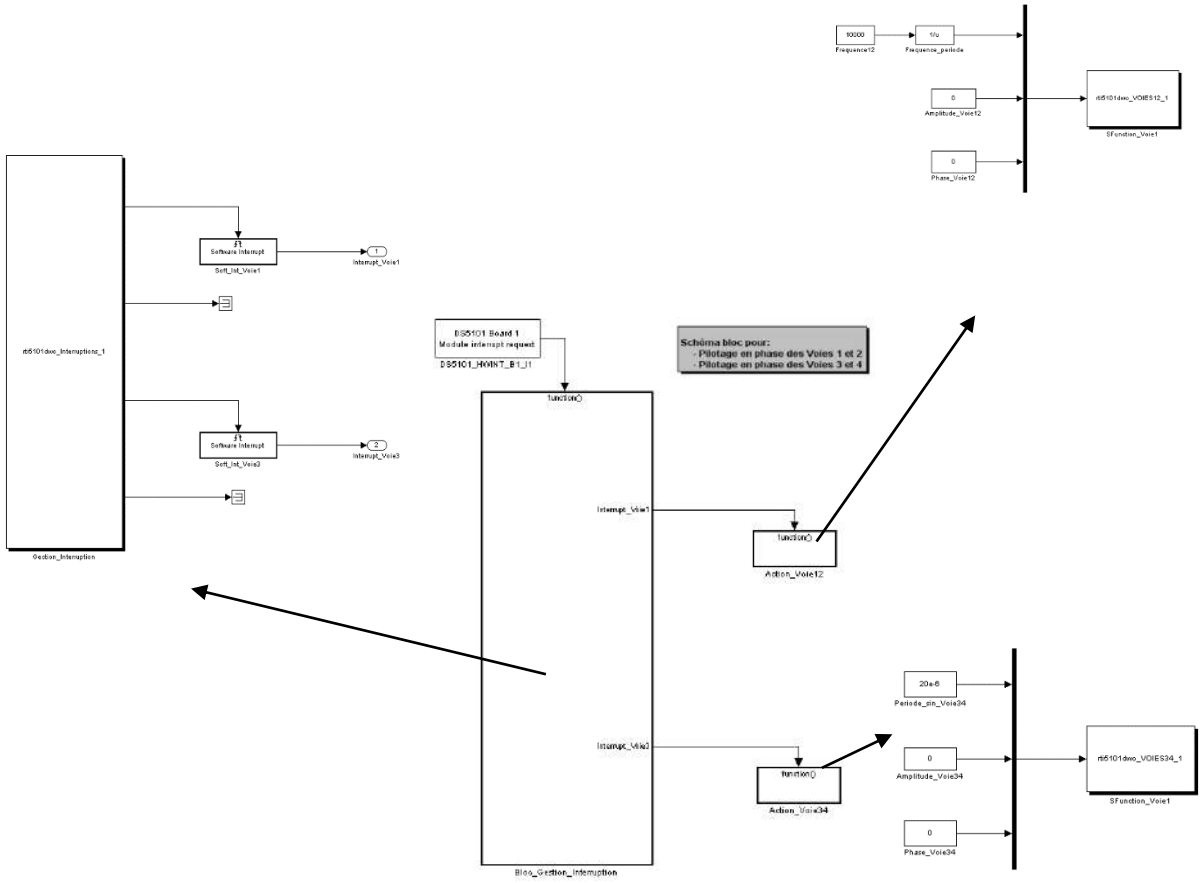

Fig. A.5.1 The main program blocks for power supply control